



University
of Glasgow

Beveridge, Nicola Louise (2012) Characterisation of silicon-silicon hydroxide catalysis bonds for future gravitational wave detectors. PhD thesis

<http://theses.gla.ac.uk/3526/>

Copyright and moral rights for this thesis are retained by the author

A copy can be downloaded for personal non-commercial research or study, without prior permission or charge

This thesis cannot be reproduced or quoted extensively from without first obtaining permission in writing from the Author

The content must not be changed in any way or sold commercially in any format or medium without the formal permission of the Author

When referring to this work, full bibliographic details including the author, title, awarding institution and date of the thesis must be given.

Characterisation of Silicon-Silicon
Hydroxide Catalysis Bonds for Future
Gravitational Wave Detectors



University
of Glasgow

Nicola Louise Beveridge MEng

School of Physics and Astronomy
Institute for Gravitational Research

University of Glasgow

Contents

Contents	i
List of Figures	v
List of Tables	viii
Acknowledgements	x
Preface	xi
Summary	xiii
1 Gravitational Wave Detection	1
1.1 Introduction	1
1.2 Sources of Gravitational Waves	3
1.3 Gravitational Waves Detectors	4
1.3.1 Introduction	4
1.3.2 Interferometric Detectors	6
1.3.3 Interferometric Techniques	7
1.3.3.1 Introduction	7
1.3.3.2 Fabry-Perot Arm Cavities	7
1.4 Limitations of Interferometric Detectors	8
1.4.1 Introduction	8
1.4.2 Gravitational Gradient Noise	9
1.4.3 Seismic Noise	9

1.4.4	Thermal Noise	10
1.4.5	Photoelectron Shot Noise	12
1.4.5.1	Power Recycling	13
1.4.5.2	Signal Recycling	13
1.4.6	Radiation Pressure Noise	14
1.4.7	The Standard Quantum Limit	15
1.5	Current Interferometric Detectors	15
1.5.1	First and Second Generation Detectors	15
1.5.1.1	LIGO	16
1.5.1.2	Virgo	17
1.5.1.3	GEO600	18
1.5.1.4	TAMA300, CLIO and LCGT	20
1.5.2	Future Detectors	21
1.5.2.1	Quantum Noise	22
1.5.2.2	Gravitational Gradient and Seismic Noise	23
1.5.2.3	Thermal Noise	23
1.6	Summary	25
2	Thermal Noise in Gravitational Wave Detectors	26
2.1	Introduction	26
2.1.1	Brownian Motion	27
2.1.2	The Fluctuation-Dissipation Theorem	27
2.2	Dissipation from Internal Friction in Materials	30
2.3	Thermal Noise associated with a Single Resonant Mode	32
2.4	The Quality Factor, Q	34
2.5	Thermal Noise in a Multi-Resonance System	35
2.5.1	The Arrhenius Equation	37
2.5.2	Debye Theory	37
2.6	Thermal Noise in a Gravitational Wave Detector	39
2.6.1	Coating Thermal Noise	39
2.6.2	Suspension Thermal Noise	39

2.6.3 Bond Loss	41
2.7 Conclusion	42
3 Hydroxide-Catalysis Bond Strength Testing	43
3.1 Introduction	43
3.2 Hydroxide-Catalysis Bonding	44
3.2.1 Hydroxide-Catalysis Bonds between Silicon	47
3.3 Thermal Oxidation of Silicon	48
3.3.1 Introduction	48
3.3.2 Oxidation Procedure	50
3.4 Bonding Procedure	54
3.4.1 Bonding Native Oxides	57
3.5 Four Point Bend Strength Tests	58
3.5.1 Experimental Set-up	58
3.5.2 Results	60
3.5.3 Analysis	61
3.6 Conclusion	70
4 Influence of the Oxide Layer on Bond Strength	72
4.1 Introduction	72
4.2 Experimental Set Up	74
4.2.1 Sample Preparation	74
4.2.2 Strength Testing Procedure	77
4.3 Results	78
4.3.1 Analysis and Comparison to Wet Thermal Oxide Results	81
4.4 Discussion and Summary	86
5 Mechanical Loss of Hydroxide-Catalysis Bonds	89
5.1 Introduction	89
5.2 Experimental Procedure	91
5.2.1 Experimental Set-Up	91
5.2.2 Measurement and Analysis Method	93

5.2.2.1	Introduction	93
5.2.2.2	Thermoelastic Damping	96
5.2.2.3	The Elastic Strain Energy stored in the Oxide Layers and Bond Layer	98
5.2.3	Sample Preparation	101
5.3	Results and Interpretation	109
5.3.1	Introduction	109
5.3.2	The Mechanical Loss in the Oxide Layers	110
5.3.3	Mechanical Loss of the Bond Layer	110
5.4	Conclusions	112
6 Conclusions		114
A Weibull Analysis Code		118
Bibliography		137

List of Figures

1.1	The effect of a gravitational wave on a ring of test particles	3
1.2	Schematic of Michelson interferometers with a delay lines and Fabry-Perot cavities	8
1.3	LIGO noise budget	9
1.4	A Michelson interferometer with power recycling	13
1.5	A Michelson interferometer with signal recycling	14
1.6	Photographs of the LIGO detectors	16
1.7	LIGO strain sensitivity improvements	17
1.8	The Virgo detector site	18
1.9	The GEO600 silica suspension	19
1.10	Diagram showing the LCGT	21
1.11	Artistic view and draft scheme of the proposed ET observatory . . .	22
1.12	ET Suspensions	23
2.1	Mechanical oscillator schematic	31
2.2	Mechanical oscillator schematic	38
2.3	Simplified diagram of the pendulum and violin modes	40
2.4	GEO suspension	41
3.1	Schematic of fused silica and hydrated fused silica	45
3.2	Schematic of the formation of a silicate bond	46
3.3	Mixed ingot pairing	50
3.4	Schematic for a wet thermal oxidation	51

3.5	Silicon samples on fused silica boat	51
3.6	Silicon samples in the furnace	52
3.7	Rate of wet thermal oxide growth	53
3.8	Flatness of oxidised silicon samples	54
3.9	Examples of high surface flatness	55
3.10	Examples of low surface flatness	55
3.11	Examples of low surface roughness	56
3.12	Photograph of specks on a bonding surface	56
3.13	Photograph showing hydrophillic and hydrophobic bonding surfaces	57
3.14	Failed bond surface	58
3.15	CAD images of strength testing set up	58
3.16	Strength test set up	59
3.17	Ansys analysis of strength test	60
3.18	Plot of all wet thermal oxide results	61
3.19	Example of a Weibull distribution	63
3.20	Joint 68% confidence regions for Weibull parameters	65
3.21	Weibull modulus and characteristic strength graphs	67
3.22	Samples post strength testing	68
3.23	Two different types of sample failure breaking at similar strengths .	68
4.1	Flatnesses of the coated silicon blocks	76
4.2	Variations observed during bonding process	77
4.3	Strength test results	80
4.4	The relationship between flatness and strength	81
4.5	Results of Weibull analysis	82
4.6	Break patterns	84
4.7	Bond break surfaces	88
5.1	Example of raw data from mechanical loss experiment	92
5.2	Typical ringdown	93
5.3	Experimental set up for measuring mechanical loss	94

5.4	Schematic diagram of the cryostat, with an inset showing details of the clamp used to hold the cantilever samples.	95
5.5	Diagram of heat flow across a bending beam	97
5.6	A schematic for the bending bonded structure, not to scale.	98
5.7	CAD schematic of the cantilevers to be bonded	102
5.8	Cantilevers undergoing wet thermal oxidation	102
5.9	Roughness of the oxidised cantilever surfaces	103
5.10	Cleaning a cantilever in piranha solution	104
5.11	Experimenting with bonding solution drop size	104
5.12	The spread of a $1\mu l$ drop	105
5.13	Bonding cantilevers with one $1\mu l$ drop of bonding solution	106
5.14	Thermal images of bonded cantilevers using one $1\mu l$ drop of bonding solution	106
5.15	Cantilever with three drops of $0.33\mu l$ bonding solution, and the bonded cantilever	107
5.16	Thermal images showing the changes in the bond over a 24 day period	108
5.17	Loss measurements for the $66\mu m$ plain silicon cantilever	110
5.18	Calculated Oxide Loss	111
5.19	Measured loss bonded structure	111
5.20	Mechanical Loss of Bond Layer	112

List of Tables

3.1	Data set sizes used in Figure 3.21	66
4.1	Data sets used in strength tests	78
4.2	Percentage of bond breaks	84

‘Don’t rest on past laurels’

J. Beveridge (1919 - 1998)

‘What’s going on *up there* then?’

D. Spray (1926 - 2011)

Acknowledgements

A Ph.D is not a solitary endeavour: this thesis would not have come into existence without the help and support of many people, all of whom deserve my utmost gratitude.

To my supervisors Professors Sheila Rowan and Jim Hough: thank you for offering me my place inside the IGR and for all the opportunities that came my way.

To the post-docs, in particular Mariëlle, Iain, Stuart and Liam: thank you for your guidance, patience and expertise. My Ph.D would not have been half what it is now without you.

To all the technicians: thank you for helping all my experiments run so smoothly, and for fixing them when they didn't.

To my peers: thank you for sharing the ups and downs of experimental work with me, it wouldn't have been the same without you.

To my friends and family: simply, thank you.

And finally, Joe: what can I say? *Teamwork.*

Preface

This thesis will be an account of work carried out by the author with support from staff in the Institute for Gravitational Research at the University of Glasgow between October 2008 and October 2011, involving studies of materials for use in future gravitational wave detectors.

The aim of this thesis is to investigate the suitability of hydroxide catalysis bonding for jointing silicon suspension components in future cryogenic interferometric gravitational wave detectors.

In Chapter 1 the context of the research is introduced: a contribution to the search for the direct evidence of gravitational waves, as predicted by Einstein.

In Chapter 2 the context of research reported in this thesis will be deepened by focussing on one important noise source in gravitational wave detectors, thermal noise, its relationship to mechanical dissipation and the influence it has on the achievable sensitivity of interferometric gravitation wave detectors.

In Chapter 3 hydroxide catalysis bonding, and its role in the construction of interferometric gravitational wave detectors and its potential for application in the suspensions of future detectors is investigated. The strength testing reported in this chapter of the bonds between silicon at both room and cryogenic temperature was carried out jointly by the author and Dr. van Veggel. The aim of this research was to determine if a minimum oxide layer thickness exists for a reliable bond to form between silicon surfaces.

The testing was completed with assistance from J. Davidson and R. Bezensek, and the analysis of the results was done with assistance from Prof. Hendry, who wrote the Fortran code used in the analysis. The work was supervised by Prof. Rowan and Prof. Hough.

The research into the strength of hydroxide catalysis bonds formed between silicon samples continues in Chapter 4, where the aim was to investigate the influence of the type of oxide layer on the bond strength. The work for this chapter was supported in a very similar way to the work in Chapter 3.

In Chapter 5, the mechanical loss of a pair of hydroxide catalysis bonded silicon cantilevers was measured from room temperature down to cryogenic temperatures. Analysis was then carried out to determine the mechanical loss components of the oxide layers and bond material. This work was carried out in Glasgow using an automated cryostat set up by Dr. Reid, Dr. Nawrodt and Dr. Martin. Dr. Martin, Dr. Reid and Dr. van Veggel all provided advice for the duration of the experiment. R. Jones designed the bonding jig for bonding the cantilevers. The MATLAB code used to analyse the data generated was written by M. Abernathy. The analysis of the data was done by the author with help from Dr. Martin and Dr. Reid.

This thesis concludes by summarising the findings and developing recommendations for future research.

Summary

The quadrupolar nature of gravitational waves, predicted by General Relativity, produces fluctuating strains in space-time that can be searched for using interferometric techniques.

Ground-based long-baseline gravitational wave detectors are being used to search for gravitational waves produced by astronomical events, such as supernovae explosions or binary systems. Masses, with highly reflective mirror coatings, are freely suspended at the ends of perpendicular arms up to 4 km in length. Laser interferometry is used to try to sense fluctuations in the relative separation of the masses caused by the passage of a gravitational wave.

Currently there several long-baseline gravitational wave detector projects around the globe, including the US LIGO project, where 4 km detectors have been operated, the 3 km Virgo detector in Italy and a 600 m UK/German detector based in Germany, GEO600. The strain expected from gravitational waves is expected to be less than $\sim 10^{-22}$, making detection of the resultant displacement of the masses highly challenging.

In the operational frequency band of between a few Hertz and a few kiloHertz, the thermal motion of the test masses and suspensions forms an important limit to the sensitivity of such detectors. The level of thermal noise is related to the mechanical loss of the test mass and suspension materials and the mirror coatings.

The first generation detectors are currently undergoing significant upgrades to further increase their sensitivity by a factor of ten. These upgrades include the installation of quasi-monolithic silica suspensions in an attempt to reduce the thermal noise of the test masses and their suspensions. Fused silica fibres are welded to fused silica interface pieces, called ‘ears’, which provide suitable welding points onto the sides of the mirror when bonded to the mirror using the high strength chemical jointing technique of hydroxide-catalysis bonding.

Plans are also developing for the design of potential ‘third generation’ detectors. These detectors may operate at cryogenic temperatures to further reduce thermal noise. Silicon is a prime candidate material for use in the test masses and their suspensions because of its desirable thermo-mechanical properties in the cryogenic regime. With some adaptation, hydroxide catalysis bonding may also be a viable technique for use in third generation detectors; however, to evaluate its suitability it is essential to quantify both the strength of silicon-silicon bonds at cryogenic temperatures and the thickness of such bonds, as the bond thickness has a direct effect on the contributions of the bond to the overall thermal noise of a bonded suspension.

This research focuses on development and evaluation of the properties of the technique of hydroxide catalysis bonding relevant to its application in future cryogenic gravitational wave detectors. Chapter 1 introduces gravitational waves and their possible sources and the techniques used for their detection. In chapter 2 thermal noise, the dominant noise source in the mid-frequency range, and how the materials in the suspension and test masses contribute to the level of thermal noise in the system, is discussed. The remaining chapters cover the experimental research: measuring the strength and mechanical loss of hydroxide catalysis bonds at cryogenic temperatures.

In chapters 3 and 4 investigations of the strength of hydroxide catalysis bonds between silicon blocks at room and cryogenic temperatures are described. To

make bonding of silicon components possible, the bonding surfaces must ideally have a thin coating of SiO_2 , with which the hydroxide can react to form the bond. Chapter 3 investigates the minimum required thickness of SiO_2 necessary for a successful bond. The bond strength, tested using a 4-point bend strength test, is found to reduce significantly with oxide layer thicknesses below 50 nm at cryogenic temperature. A Weibull analysis of the results showed a characteristic strength of approximately 41 MPa at 77 K and 35 MPa at room temperature for samples with a minimum oxide layer of 50 nm.

In chapter 4 the effect on the oxide layer deposition method and the purity of the silicon ingot on the strength of the bond are studied. Bend strength tests were performed on hydroxide-catalysis bonds formed between silicon samples of different crystallographic orientation and purity, that had been oxidised using a range of methods. The three methods used were; dry thermal oxidation, ion beam sputtering and e-beam deposition. It was found that the method used influenced the strength of the resulting bond, with the e-beam deposited layers producing the weakest samples. It is postulated that the reason for the lower strength of the e-beam samples is correlated with the lower density of this type of coating compared with other coating methods.

The mechanical loss of the bond between silicon cantilevers between 10 K and 250 K was measured in Chapter 5. The experimental set up is described, the results are presented and then analysed to establish an upper limit of 0.12 for the second bending mode below 100 K. The lowest loss measured was 0.06 at 12 K.

Chapter 1

Gravitational Wave Detection

1.1 Introduction

The direct detection of gravitational waves would enable our universe to be studied in a whole new way, opening up a new field in astronomy, and confirming directly a further prediction of Einstein's General Theory of Relativity (General Relativity).

The existence of gravitational waves was predicted in 1916 [1]. Many decades later, a key measurement of the effects of gravitational waves was made by Hulse and Taylor [2; 3] through the discovery and subsequent observation of the evolution of the orbit of the binary pulsar PSR 1916+16. Their observations agreed with the prediction of General Relativity to within 1% [2; 3], leading to the award of the 1993 Nobel Prize for Physics to them. However, the first direct detection of gravitational waves is still the subject of significant effort by scientists around the globe.

Gravitational waves are deformations of spacetime due to the action of asymmetrically accelerating mass. The gravitational force is very weak and pertur-

bations of a detectable level require very large masses and associated accelerations.

This limits potential sources of detectable gravitational waves to those of astrophysical origin, such as supernova explosions, binary neutron stars and black hole mergers. The gravitational waves from such sources produce fluctuating strains in space. These strains are predicted to be very small, of the order of 10^{-21} or lower [4; 5] and as a result are very difficult to directly detect.

However, the weak interaction of gravitational waves with matter means that they have reduced susceptibility to scattering and absorption compared to electromagnetic radiation, making them a potentially valuable tool for astronomers.

Gravitational waves are quadrupolar in nature. They are generated by asymmetric acceleration of mass such that a passing gravitational wave will exert a differential strain along perpendicular paths in space. There are two polarisations of gravitational wave: the “plus” polarisation and “cross” polarisation. The strain patterns cause contraction of space in one transverse direction while expanding it along the orthogonal direction in the transverse plane. The effect this has on a ring of test particles suspended freely in space is illustrated in Figure 1.1. Taking the change in length of the perpendicular axes to be $\pm\Delta L$, the total strain, h , is defined to be:

$$h = \frac{2\Delta L}{L} \quad (1.1)$$

A direct detection would not only further verify Einstein’s General Theory of Relativity, but it would also allow direct extraction of information about the behaviour of the masses involved in astrophysical events such as supernova explosions, coalescence of binary systems, rotation of pulsars and interactions between black holes [6].

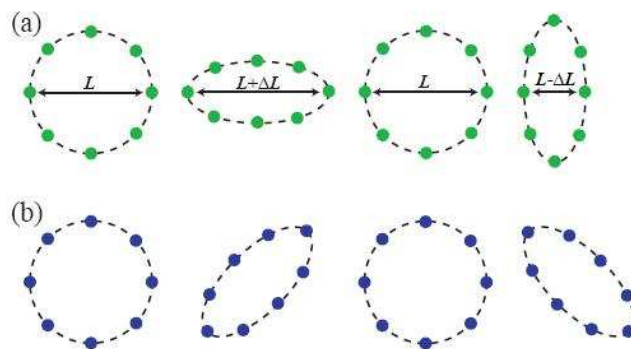


Figure 1.1: *The effect of a gravitational wave incident normal to the page on the position of a ring of particles in space where the wave has a (a) plus polarisation and (b) cross polarisation.*

1.2 Sources of Gravitational Waves

Astronomical sources of gravitational waves detectable by ground based detectors (producing gravitational waves the frequency range of a few Hz to a few kHz) have been predicted to cause strains in space time of the order of 10^{-21} to 10^{-39} on arrival on Earth [7]. A brief overview of some important sources follows.

Supernova explosions, some of the most violent astronomical events, formed a key source motivating the development of initial gravitational wave detectors [8]. Type II supernovae are believed to be triggered by the gravitational collapse of the core of an evolved star. Some models predict the emission of gravitational waves when the collapse is reversed in a ‘bounce’ once the core reaches nuclear densities [7].

One resultant end state from a Type II supernova explosion is thought to be a spinning neutron star, known as a pulsar [7]. A pulsar is considered to be a potential source of periodic gravitational waves [9], associated with non-axisymmetric rotation. Non-axisymmetric rotations may arise from a variety of phenomena, such as: irregularities in the star’s crust or irregularities that

have become frozen into the stars structure as it cooled; strains that have built up as the star has spun down; or a mode of pulsation that is excited in some way [8].

An extremely important potential class of gravitational wave source is that of neutron stars and black holes in binary systems orbiting their common centre of mass. Although black hole - black hole and black hole - neutron star binary systems have yet to be observed, they are expected to exist and to emit gravitational waves with a greater amplitude than neutron star - neutron star systems due to the greater density and mass of black holes [8].

In addition to the sources above, a background of gravitational radiation is expected to exist. This background will include the superposition of signals from the discussed astrophysical sources as well as from the very early universe. Such sources have been reviewed in detail by Allen [10] and Abbott et al. [11].

1.3 Gravitational Waves Detectors

1.3.1 Introduction

Initial experiments to detect gravitational waves were performed by Joseph Weber [12; 13]. They involved aluminium ‘bar’ detectors which were, by their design, sensitive in a range close to one resonant frequency of $\simeq 1600$ Hz, a frequency where the energy spectrum of the signals from collapsing stars was predicted to peak. Piezoelectric crystals bonded around the centre of such a bar were used to monitor oscillations of its fundamental resonant mode. If a gravitational wave of sufficient amplitude passed through the bar, the fundamental mode would be expected to be excited, with the piezoelectric crystals detecting changes to the amplitude of motion of the bar.

Weber claimed detection of gravitational waves in 1968 [13], when multiple coincident events were observed in bars 2 km apart. Further coincident readings were reported by Weber from larger bar detectors 1000 km apart [13; 14] but his results could not be reproduced. It was later estimated that the bar detectors at that time lacked the sensitivity to detect gravitational waves from any plausible sources, however it sparked the development of many more gravitational wave detectors in the scientific community.

Bar detectors were expected to be able to detect strains of the order of 10^{-16} [15], which was later improved to $\simeq 10^{-21}$ by cooling the bar detectors to cryogenic temperatures. Some of the low temperature detectors which have been operated over a period of years include Allegro [16], EXPLORER and NAUTILUS [17], NIOBE [18] and AURIGA [19; 20].

Of these, the AURIGA, EXPLORER and NAUTILUS bar detectors still function [21], however they were generally succeeded by detectors based on Michelson type interferometers. These kilometer scale interferometric gravitational wave detectors were able to reach sensitivities of at least 10^{-21} at $\simeq 200$ Hz by 2005, [21]. They are able to operate over a range of frequencies, an improvement over the bar detectors which are limited to a narrow frequency band around their resonant frequency. Interferometric detectors are discussed in more detail in Section 1.3.2.

The ‘first generation’ interferometric detectors LIGO, GEO600, and Virgo operated between a few Hz and a few kHz at room temperature. Presently, LIGO and Virgo are undergoing major upgrades to ‘second generation’ detectors. These detectors will be discussed in Sections 1.5.1.1, 1.5.1.3, and 1.5.1.2.

Plans for ground-based ‘third generation’ detectors and space based experiments are also underway. The Einstein Telescope (ET) [22] and LISA mission [23] are examples of such endeavours.

ET is proposed to operate over a wider frequency range than the first and second generation detectors. It is likely to be sited underground and operated at cryogenic temperatures to further reduce environmental noise and increase sensitivity beyond that planned for the second generation detectors. This is discussed further in Section 1.5.2. Space-based experiments are expected to operate below 1 Hz [24] where sources such as the coalescence of massive black holes and resolved and unresolved galactic binaries form interesting targets for study.

This thesis will focus on investigations of some of the technology to be applied in second generation ground based interferometric gravitational wave detectors and the evolution of designs required for the implementation of third generation cryogenic detectors.

1.3.2 Interferometric Detectors

Laser interferometry can be used to sense fluctuations in the relative separation of freely suspended masses at the ends of perpendicular arms: laser light is divided by a beam splitter and directed down the two arms. Test mass mirrors placed at the end of each arm reflect the light back towards the beam splitter where it is recombined and the resulting interference pattern is sensed using a photodiode. When a gravitational wave passes, one arm will lengthen while the other shortens. This causes a relative phase shift between the two reflected beams and a change in intensity of the interference pattern at the photodiode.

1.3.3 Interferometric Techniques

1.3.3.1 Introduction

Long-baseline gravitational wave detectors such as the LIGO [25; 26], Virgo [27], TAMA [28] and GEO 600 [29] instruments have been designed to search for the effects of gravitational waves by using laser interferometry to measure fluctuations in the relative separation of suspended masses as described above. LIGO, Virgo and TAMA have designs based on a Michelson interferometer with Fabry-Perot cavities in the arms of the interferometer. An alternative topology is seen in the GEO optical layout, which is an example of a Michelson interferometer incorporating delay lines [30]. Examples of each kind of set-up can be seen in Figure 1.2. In a Fabry-Perot cavity, the light is bounced many times between mirrors forming a cavity in each arm with the light beams following the same spatial path. In a delay line interferometer the multiple beams are spatially separate, therefore for the same increase in arm length, using a delay line interferometer requires a larger mirror diameter than the Fabry-Perot cavity.

The configuration of a Michelson interferometer can be adapted to increase its sensitivity in several ways, some examples of which are described in more detail in the following sections. They include Fabry-Perot cavities, power recycling [31] and signal recycling [32–34].

1.3.3.2 Fabry-Perot Arm Cavities

In order to enhance the phase change of the laser light due to a disturbance (such as one caused by a gravitational wave), Fabry-Perot optical cavities can be inserted into the arms of the interferometer. This results in the laser beam being reflected back and forth inside the cavity, increasing the light storage

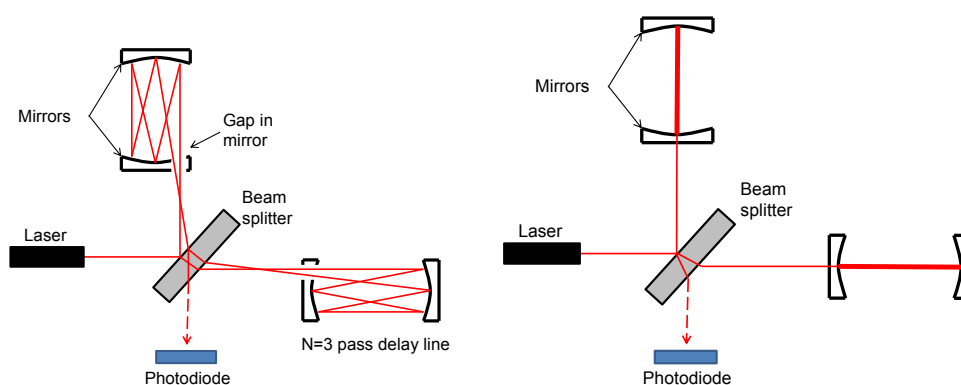


Figure 1.2: *Michelson interferometers with delay lines (left) and Fabry-Perot cavities (right).*

time in the arms and building up a light field in the cavity. This configuration is shown in Figure 1.2.

The input mirror of each cavity is partially transmissive, in order to allow some light to enter and leave the arm. The phase change that could be expected due to the presence of a gravitational wave would be enhanced with each bounce the light makes along the cavity.

1.4 Limitations of Interferometric Detectors

1.4.1 Introduction

Figure 1.3 shows the noise budget for the interferometers of the LIGO project, as an example of the types of noise sources which can limit the sensitivities of ground based interferometric gravitational wave detectors. In order to further improve the sensitivity of ground based detectors it is necessary to reduce the limiting noise sources.

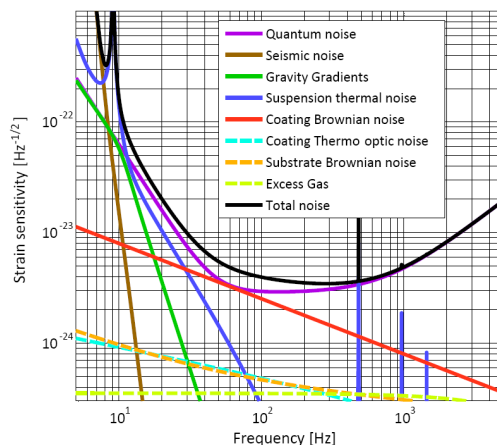


Figure 1.3: *Advanced LIGO noise budget [35].*

1.4.2 Gravitational Gradient Noise

At frequencies below approximately 10 Hz, the interferometer test masses are vulnerable to gravitational gradient, or Newtonian, noise. Variations in the local gravitational field can directly induce motion in the test masses, which cannot be completely shielded from such disturbances [36; 37]. The fluctuations can be produced by sources such as surface waves in the Earth's crust and also by human activity in the vicinity of the detector, including road traffic and aircraft flying overhead [7].

For ground based detectors on the surface of the Earth, gravity gradient noise forms a significant limit to sensitivities below ~ 10 Hz [36]. Placing the detector approximately 150 m underground reduces the influence of surface waves in the 1-10 Hz frequency band [38]. However, to achieve desired sensitivities below ~ 1 Hz, space based gravitational wave missions must be considered [6].

1.4.3 Seismic Noise

Ground-based interferometric detectors are sensitive to the environment in which they are placed. Anthropogenic activity close to the detector sites can

cause seismic vibrations which limit the detector sensitivity at the lower end of the frequency band, between 1 and 10 Hz. Thus, locations for ground based gravitational wave detectors should be carefully considered and selected for their distance from busy urban areas and geographical disturbances. Below 1 Hz, micro-seismic noise is caused by the impacts of ocean waves on continental coastlines [7].

The limitations in sensitivity due to seismic noise can be minimised by careful design of the test mass suspensions. Isolation from seismic noise in the horizontal direction can be obtained by suspending the test masses as simple pendulums: when the vibrational disturbances occur at frequencies above the resonant frequency of the pendulum, the transfer function for displacement between horizontal motions of the suspension point and the pendulum mass is proportional to $1/f^2$. Suspending the mass on a vertical spring can provide vertical isolation, and thus practical mirror suspensions typically incorporate both types of mechanical isolation [39].

In addition to the passive isolation systems described above, a feed-forward system can be applied. Measured environmental motion from seismometers on the building foundations is transmitted to piezoelectric actuators in the legs of the pendulum suspension structure to reduce the motion of the suspension structure [40; 41]. ‘Active’ isolation can also be implemented alongside feed-forward, where feedback servo loops attempt to null motion measured on the payload [41].

1.4.4 Thermal Noise

Thermal noise is one of the primary limitations to the sensitivity of gravitational wave detectors over the range of frequencies at which they are most sensitive (a few Hz up to several hundred Hz) [42–44]. It is caused by the

thermally driven motion of molecules in the test mass mirrors, their coatings and suspensions.

Thermal noise in the mirror coatings can be considered to be present in two broad forms. Firstly, thermal noise arising from the ‘mechanical loss’ of a coated mirror, arising from defects in the structure of the material or associated with the intrinsic structure of the material. Secondly thermal noise resulting from the effects of local statistical fluctuations in temperature which can result in local material deformations and thermo-optic noise[45].

The various resonant modes of a suspended test mass mirror can be driven by thermal excitation, with each mode having on average $\frac{1}{2}k_B T$ of thermal energy associated with it. The internal modes of the mirrors themselves are typically at frequencies above the gravitational wave detection band, thus the thermal noise contribution in the operating range of a gravitational wave detector comes effectively from the tails of the resonant modes.

By concentrating the majority of the thermal noise near to the resonances of the suspended test mass, the thermal motion off-resonance in the operational frequency range of the detectors can therefore be reduced. This is achieved through the use of low loss materials for the test mass and suspensions; ultra pure fused silica is one such material suitable for use at room temperature [46] and can be used as the substrate material for the test mass and for the suspension fibres.

Hydroxide-catalysis bonding, which will be discussed in Chapter 3, is a jointing technique suitable for use in a detector that uses silica fibres and test masses. It enables the construction of quasi-monolithic suspensions, which reduces the thermal noise associated with the suspension of the mirrors beyond that of a wire suspension [47].

In principle, thermal noise can be reduced by cooling the test mass mirrors and

using materials that have a low level of mechanical loss at low temperature. This rules out the use of amorphous fused silica in future cryogenic detectors due to its broad mechanical loss peak at ~ 40 K resulting from its internal material structure [46]. As alternative test mass and suspension materials, crystalline materials such as sapphire and silicon are of interest [48; 49].

Thermal noise will be discussed in greater detail in Chapter 2, and the application of hydroxide-catalysis bonding for a silicon suspension at cryogenic temperature, and its mechanical loss contribution, will be investigated in Chapters 3, 4 and 5.

1.4.5 Photoelectron Shot Noise

Changes in the lengths of the interferometer arms can be monitored through the variations in the intensity of the interference patterns of the recombined laser light detected at the output photodiode. The limit to the sensitivity of the optical readout system is set by the fluctuations in the detected output signal. Assuming the photoelectrons follow Poisson statistics, a signal containing N photons detected by a photodiode would have an error of \sqrt{N} associated with it.

In a simple Michelson interferometer, with laser of power P and wavelength λ , it can be shown that the differential displacement Δx , of the mirrors determined using equation 1.2 [31]:

$$\Delta x = \left(\frac{\hbar c \lambda \Delta f}{4\pi P \cos^2(\phi/2)} \right)^{1/2}, \quad (1.2)$$

where the phase difference between the light in the two arms of the interferometer at the point they combine is ϕ , and $\hbar = h/(2\pi)$ is the reduced Planck constant.

These factors limit the accuracy with which the differential displacement of the test mass mirrors can be determined. Note from equation 1.2, that increasing the laser power can reduce the displacement of the test mass mirrors due to photo-electron shot noise.

1.4.5.1 Power Recycling

Operating an interferometer close to a dark fringe (where the recombined laser light at the beam splitter interferes constructively toward the laser) is beneficial as it improves the shot noise limited sensitivity of the system [31].

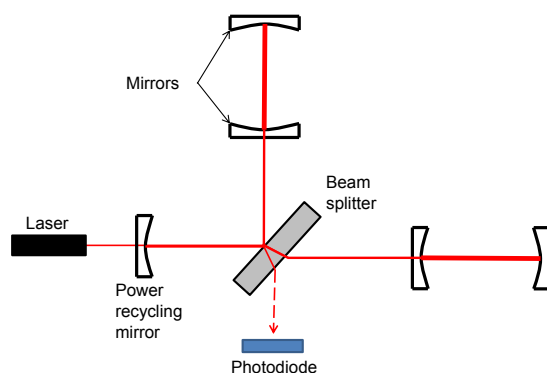


Figure 1.4: A Michelson interferometer with power recycling.

Placing a mirror between the laser and beam splitter (shown in Figure 1.4) reflects the laser beam back into the interferometer, enabling light to build up in the cavity formed between this ‘power recycling’ mirror and the interferometer. The result is an increase in the light incident on the beam splitter of the interferometer, and thus an increased sensitivity.

1.4.5.2 Signal Recycling

The recycling of ‘signal’ light at the output port can also offer improved sensitivity, this time at particular frequencies [32–34]. When an interferometer is

operating close to a dark fringe a disturbance, such as a gravitational wave, that changes the phase of the returned light causes light to leak out of the output port.

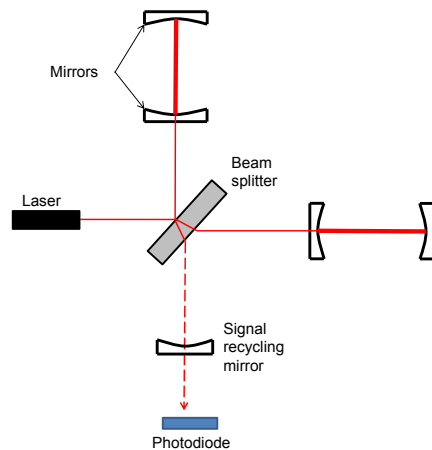


Figure 1.5: A Michelson interferometer with signal recycling.

The presence of a ‘signal recycling’ mirror (shown in Figure 1.5) enables the tuning of the response curve of an interferometer through the repositioning of the mirror. Signals at specific frequencies can be resonantly enhanced at the expense of others, allowing a detector to have enhanced sensitivity over frequency ranges of interest.

1.4.6 Radiation Pressure Noise

A fluctuating radiation pressure force arises from zero-point fluctuations of the amplitude of the vacuum electromagnetic field [50; 51]. If this light has the correct phase it will increase the light intensity in one of the interferometer arms while decreasing the intensity in the other arm, producing anti-correlated fluctuations of the light intensity in each arm. These intensity fluctuations are the differential driving force which results in radiation pressure noise.

For a simple Michelson interferometer, the differential displacement between each test mass, m , resulting from fluctuation in the radiation pressure at an

angular frequency ω , is given by [31]:

$$\Delta x = \left(\frac{16\pi\hbar P \Delta f}{\lambda m^2 \omega^4 c} \right)^{1/2} \quad (1.3)$$

It can be seen that both increasing the laser power and decreasing the mass of the mirrors can increase the displacement of the test mass mirrors caused by radiation pressure noise.

1.4.7 The Standard Quantum Limit

Sections 1.4.5 and 1.4.6 describe statistically independent sources of optical noise which decrease and increase, respectively, as a higher laser power is used. At any frequency of observation, an optimum laser power can be set, where the total quantum noise is at a minimum [31].

This sensitivity limit is known as the Standard Quantum Limit (SQL) and it corresponds to the limit set by the application of the Heisenberg Uncertainty Principle, in its position and momentum formulation [31; 50–52]. However, in principle, it can be overcome by using techniques that introduce a correlation between shot noise and radiation pressure [53; 54].

1.5 Current Interferometric Detectors

1.5.1 First and Second Generation Detectors

Over the past decade, kilometre-scale interferometric gravitational wave detectors have been operating around the world. The first generation of such detectors includes those of the LIGO project, based in the United States,

Virgo and GEO600, based in Italy and Germany, respectively, and TAMA300 based in Japan.



Figure 1.6: *Photographs of the two LIGO sites: Hanford (left) and Livingston (right).*

1.5.1.1 LIGO

The initial LIGO instruments comprised a 4 km and a 2 km detector located in Hanford, Washington and a 4 km detector in Livingston, Louisiana (Figure 1.6). The initial detector systems used Fabry-Perot cavities, power recycling and steel wire loop single stage suspensions. Six science runs have been completed. The first run, S1, starting in August 2002, and the latest run, S6, finished in October 2010. The two 4 km detectors were partially upgraded as part of the ‘enhanced’ LIGO project between 2007 and 2009, which increased their sensitivity between S5 and S6, as shown in Figure 1.7, and tested techniques for future, more substantial upgrades that would become part of the second generation ‘Advanced LIGO’ project. The science runs were often coincident with those of other detectors such as GEO600, Virgo and TAMA.

After the end of the S6 run, the two 4 km detectors were taken out of operation (the 2 km detector was taken offline in summer 2009) for the start of construction of Advanced LIGO.

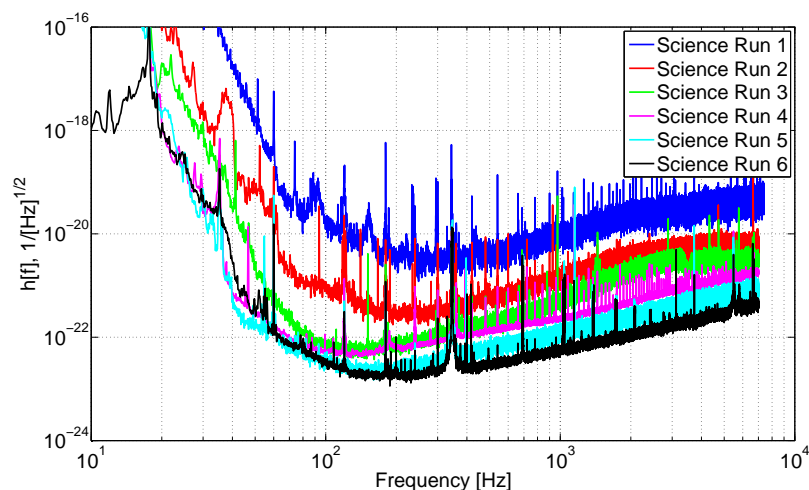


Figure 1.7: *The improvement in the sensitivity for the 4km LIGO interferometers can be seen in the increased sensitivity for each science run. Science run 6 is the sensitivity curve for Enhanced LIGO. (<http://www.ligo.caltech.edu/>)*

Advanced LIGO will enable major improvements in sensitivity over that of initial LIGO, with a factor of ten to fifteen increase in sensitivity being anticipated. The 2km interferometer at Hanford will be extended to become a third 4km detector, with the first data from the upgraded systems expected to be taken in 2014 [55]. The upgrades include, amongst other developments, the introduction of signal recycling (discussed in section 1.4.5.2) to optimise the detector sensitivity, a higher laser power to improve shot noise limited sensitivity (section 1.4.5), silica suspensions replacing initial LIGO’s wire suspensions to reduce the thermal noise in the system (section 1.4.4), and heavier test masses to counter the increased radiation pressure noise from the higher laser power (section 1.4.6) [55–57].

1.5.1.2 Virgo

The Virgo detector, built under a French-Italian collaboration, is sited near Casina in Italy. It has 3km long arms (Figure 1.8), and is based on a Fabry-

Perot Michelson-type interferometer with power recycling.



Figure 1.8: *The Virgo detector site in Italy.*

A multiple-stage horizontal pendulum arrangement, known as a ‘superattenuator’, with the lower stages suspended from an inverted pendulum with cantilever springs [58] providing seismic isolation and damping the pendulum modes [59].

Virgo became ‘Virgo+’ in 2008 when a set of medium scale improvements were made to the detector [60], and then in 2011 a major upgrade commenced to form a second generation ‘Advanced Virgo’ system. The upgrades will be similar in timescale to those proposed for Advanced LIGO and with a similar sensitivity goal. More information regarding Advanced Virgo and Virgo+ can be found in references [60] and [61].

1.5.1.3 GEO600

GEO600, a detector built under a German - UK collaboration has a shorter arm length of 600 m, is also based on a Michelson type interferometer design but without Fabry-Perot cavities. Instead, it uses a four-pass delay-line optical layout, and was the only first generation detector to use signal recycling [62]

and silica suspensions. The silica suspensions, shown in Figure 1.9, consist of fused silica fibres welded onto fused silica interface pieces ('ears') bonded onto the side of the test masses using hydroxide-catalysis bonding. This provided the detector with a much lower level of thermal noise contributed from the suspensions, by way of forming a quasi-monolithic structure [63].

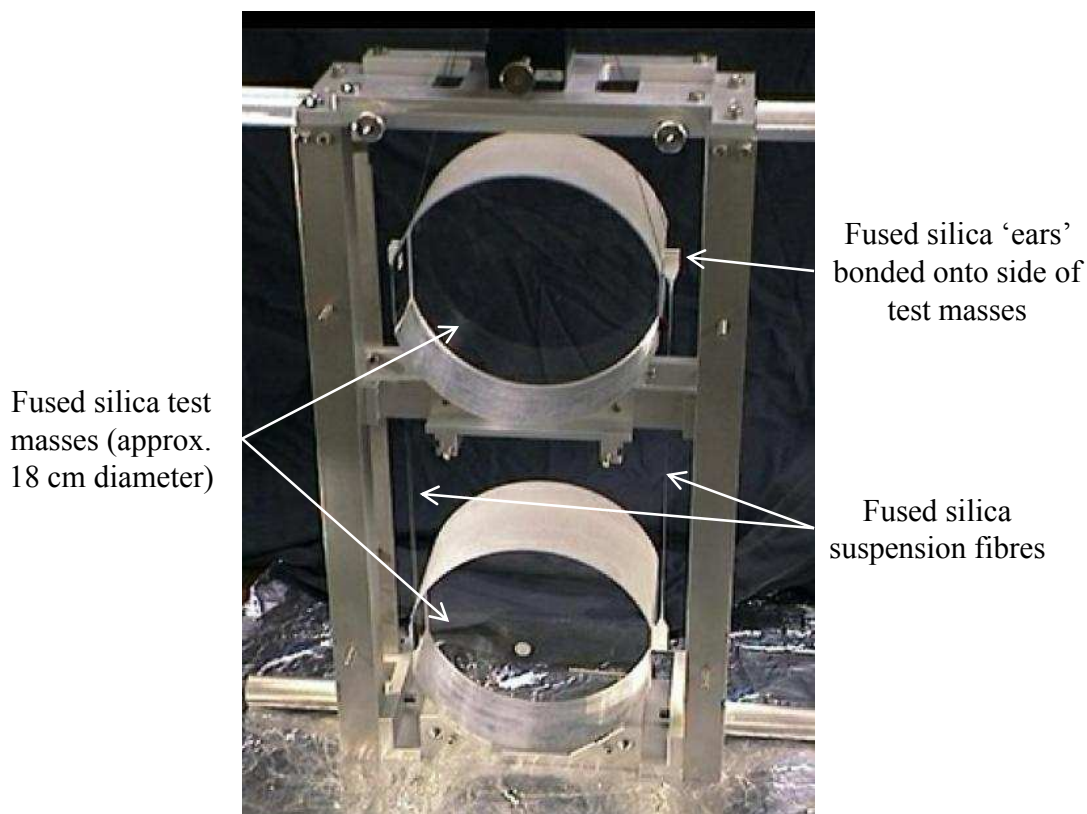


Figure 1.9: *The GEO600 silica suspension.*

The use of these novel technologies enabled GEO600 to take part in the first full-scale data taking runs alongside LIGO and Virgo despite its shorter arm lengths.

The technique of hydroxide-catalysis bonding and its contribution to the thermal noise of a system, will be discussed in greater detail in Chapters 3 and 5, as the focus of this thesis will be the potential application of hydroxide-catalysis bonding in future gravitational wave detectors.

GEO-*HF*, an upgrade program for GEO600 that will enable it to be used as a test-bed for novel interferometric techniques, began in summer 2009. GEO-*HF* participated alongside LIGO during the S6 science run in an overnight and weekend mode [6].

1.5.1.4 TAMA300, CLIO and LCGT

TAMA300 was the first interferometric detector to start taking data with sufficient sensitivity to potentially detect gravitational waves at the galactic centre [64]. Optimally polarised gravitational waves emitted from coalescing binary stars of at least $1.4 M_{\odot}$ at a distance of 10 kpc, and gravitational waves with a strain amplitude of $\sim 10^{-18}$ from supernova explosions could be detected by TAMA [64].

Between August 1999 and January 2004 TAMA had nine data taking periods over which time its typical strain noise sensitivity, in its most sensitive frequency band improved from $\sim 3 \times 10^{-19} \text{ Hz}^{-1/2}$ to $\sim 1.5 \times 10^{-21} \text{ Hz}^{-1/2}$ [65].

The design was a Fabry-Perot Michelson interferometer similar to the designs of LIGO and Virgo. Built mainly underground at the Tokyo Astronomical Observatory, TAMA300 acts as a test bed for future larger scale detectors in Japan.

The Large-scale Cryogenic Gravitational-wave Telescope (LCGT) is a planned second generation detector to be based underground in the Kamioka mine, Japan [66; 67]. With arms 3 km in length, and sapphire test mass mirrors and suspensions, it will initially run at room temperature, before being cooled for cryogenic operation. It is expected to have similar sensitivities to Advanced LIGO and Virgo. The LCGT is currently under construction, and is anticipated to begin data taking in 2017 [68].

Technology for the LCGT is being demonstrated by the Cryogenic Laser In-



Figure 1.10: Diagram showing the plans for the Japanese LCGT detector, based on the technology from the CLIO detector. (<http://gw.icrr.u-tokyo.ac.jp/lcgt/>)

terferometer Observatory (CLIO) [69], a 100 m baseline interferometer also situated in the Kamioka mine. CLIO will be able to demonstrate the low levels of seismic noise in the mine, and the installation of sapphire test mass mirrors suspended on aluminium wires cryogenically cooled to ~ 14 K [69].

1.5.2 Future Detectors

With the anticipation that the first gravitational waves will be detected by the second generation detectors, plans are developing for the design of potential ‘third generation’ detectors (such as the Einstein Telescope¹) [22; 70] that are expected to have a factor of ten improvement over the advanced, second generation, detectors. In order to accomplish this, the limitations of the technologies used in the advanced detectors need to be overcome, and new technologies for reducing noise sources must be applied. Some of these are summarised below.

¹<http://www.et-gw.eu>

1.5.2.1 Quantum Noise



Figure 1.11: *An artistic view (left) and draft scheme of three nested detectors (right) of the proposed ET observatory. (<http://www.et-gw.eu>)*

Figure 1.11 shows the conceptual design of the Einstein Telescope [22], an underground interferometer with 10 km length arms using a nested triangle formation, rather than the ‘L-shaped’ configuration of the first and second generation detectors.

Two interferometers are present in each of the three detectors (known as a xylophone configuration); one optimised for low frequency gravitational waves (ET-LF) using a lower power laser, and another for high frequency waves (ET-HF) using a higher laser power [71]. The use of a lower power laser at low frequency reduces the radiation pressure noise over the frequency range where it is most significant. Conversely, at higher frequencies, where the shot noise is dominant, the use of a higher power laser reduces the shot noise limit to sensitivity. The relationship between laser power and radiation pressure and shot noise was discussed in Sections 1.4.6 and 1.4.5.

1.5.2.2 Gravitational Gradient and Seismic Noise

Placing a detector underground can reduce the gravitational interactions between the optics and the surrounding ground (see Section 1.4.2). The longer arm lengths reduce the effects of displacement noise and the triangle formation allows the detector to be sensitive to both polarisations of gravitational wave simultaneously (shown in Figure 1.1) [72].

A suspension design similar to the Virgo superattenuator is proposed for use in the Einstein Telescope to minimise seismic noise. It is based on a multi-stage pendulum, and would suppress the transmission of ground seismic vibrations using an inverted pendulum top stage and mechanical seismic filters connected by metallic suspension wires [73]. An artist's impression of the ET suspension system in place is shown in Figure 1.12.

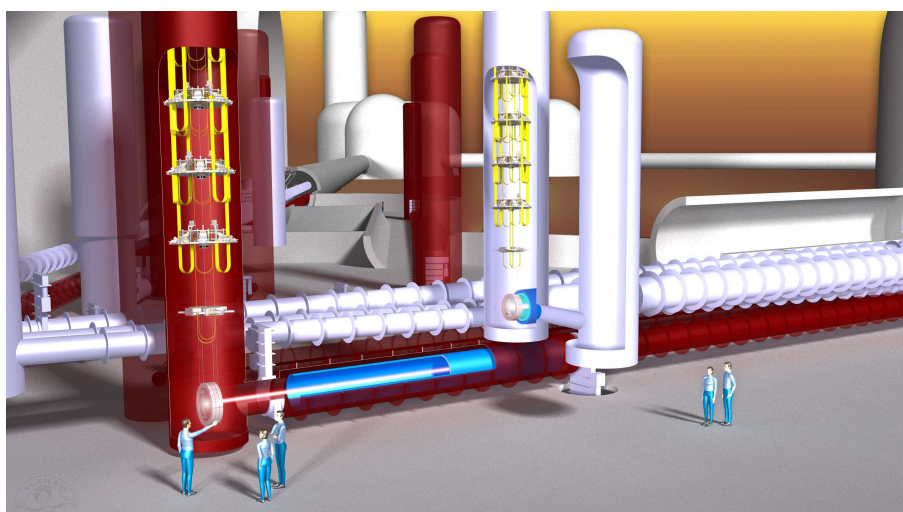


Figure 1.12: *Artist's impression of the ET suspension system, showing the superattenuator. (<http://www.et-gw.eu/>)*

1.5.2.3 Thermal Noise

Fused silica is the material of choice for room temperature advanced detectors due to its low optical and mechanical loss at room temperature [74] and avail-

ability in large sizes with high purity. This forms the substrate material chosen for GEO600 [75], Advanced LIGO [56] and Advanced Virgo [22] detectors. The designs for ET-HF, which will operate at room temperature, propose to use fused silica for all optical components.

Since the sensitivity is expected to be limited by thermal noise below ~ 400 Hz, ET-LF will operate at cryogenic temperature. The cooled optic and suspensions will require a crystalline material for the test mass and suspensions, due to an increase in mechanical loss which occurs with reduction in temperature for fused silica [46; 76], peaking around ~ 40 K.

Two candidate materials with low intrinsic mechanical loss at low temperature are under consideration for use in ET-LF: silicon [77] and sapphire [78]. Sapphire is already in use as a test mass material in CLIO, in preparation for use in the LCGT. However, silicon is the more promising of the two due to the ease of availability of large bulk samples [79].

In order to realise a silicon suspension system, research and development is underway for the manufacture and characterisation of silicon suspension fibres [79; 80], and the bonding of silicon in order to create a quasi-monolithic suspension [81–83]. The jointing technique must provide a bond with sufficient strength to suspend the test mass, high thermal conductivity in order for the heat from the laser to be transported away from the cryogenically cooled mirror, and low mechanical loss, to minimise the thermal noise contribution.

The technique of hydroxide-catalysis bonding has been successfully used in this context in the GEO600 detector, as described in section 1.5.1.3, and is being used to construct low loss silica suspensions for Advanced LIGO and Virgo.

In this thesis the suitability of hydroxide-catalysis bonding for application in jointing silicon - silicon components for ET-LF will be investigated.

1.6 Summary

Astrophysical events such as supernova explosions, and binary systems of black holes and neutron stars are potential sources of gravitational waves. A direct detection of such waves would both verify Einstein's General Theory of Relativity and enable astronomers to obtain direct and novel information about the behaviour of massive astrophysical systems.

Interferometric gravitational wave detectors are currently undergoing major upgrades to improve their sensitivities by a factor of ten from the initial detectors, commissioned a decade ago.

This second generation of detectors is expected to be successful in the search for the first detection of gravitational waves, as predicted in 1916 by Einstein.

Already, plans are underway for the third generation of ground based interferometric detectors, with the Einstein Telescope European Collaboration having published a conceptual design study in 2011. The Einstein Telescope aims to further improve sensitivity beyond that planned for the second generation detectors by a factor of ten. For this to be achieved, the noise sources that limit the first and second generation detectors must be overcome.

This research focuses on the characterisation of the strength and mechanical loss of the hydroxide-catalysis bonding technique when applied to silicon components and subjected to cryogenic temperatures to investigate its suitability for quasi monolithic suspensions in future generation gravitational wave detectors.

Chapter 2

Thermal Noise in Gravitational Wave Detectors

2.1 Introduction

One of the fundamental limitations to the sensitivity of a gravitational wave detector is set by the thermal noise, a generalisation of Brownian motion, of the test masses and their suspensions. This limits the performance of the detector between a few Hertz and several hundred Hertz.

The thermal displacement noise sensed at the surface of optical substrates arises from dissipation arising from a combination of sources, which are commonly classified into three types. Brownian noise describes the fluctuations resulting from localised sources of mechanical dissipation associated with, for example, defects distributed inside the mirror substrate. Thermoelastic noise is caused by the statistical temperature fluctuations which cause heat flow (and therefore energy loss) in the substrate. Thirdly, the motion of the substrate surface due to the temperature fluctuations causing thermal expansion and contraction, as described by Braginsky [48].

Key sources of thermal noise in interferometric detectors include dissipation associated with the test mass substrate material noise, the mirror coating and the suspensions used to support the test mass mirrors.

In the substrates and coatings thermal noise arises from the intrinsic mechanical dissipation of the materials, and from thermoelastic and thermo-optic effects arising from temperature fluctuations. Thermal noise also occurs from dissipation associated with the suspension fibres, where this can result in motions of the front face of the suspended mass.

2.1.1 Brownian Motion

Brownian motion was discovered by Robert Brown, who observed the erratic motion of small grains of dust and pollen suspended in water [84]. The phenomenon remained unexplained for many years, until Einstein was able to show that the motion arose from fluctuations in the rate of impacts of individual water molecules on the grains [85].

Equation 2.1 shows the mean-square displacement of a particle, $\overline{x_{therm}^2}$, connecting the molecular impacts to the dissipation of a grain's thermal energy ($k_B T$) as it moves through the fluid. Here, τ is the duration of the observation, a is the radius of a spherical grain and η represents the viscosity of the fluid in which the grains are suspended.

$$\overline{x_{therm}^2} = k_B T \frac{1}{3\pi a \eta} \tau \quad (2.1)$$

2.1.2 The Fluctuation-Dissipation Theorem

Brownian motion embodies the link between fluctuations (e.g. in the position of a particle) and dissipation (energy loss due to the viscosity of the fluid). In

general, any parameters which characterise a linear system in thermal equilibrium are found to undergo spontaneous thermally driven fluctuations, whose magnitude and frequency spectrum are related to the dissipative (i.e. real) part of the impedance of the system.

For a linear system, the equation of motion in the frequency domain can be written in terms of an external force, $F_{ext}(\omega)$, necessary to cause the system to move with a sinusoidal velocity of amplitude $v(\omega)$:

$$F_{ext}(\omega) = Z(\omega)v, \quad (2.2)$$

where the function $Z(\omega)$ is the mechanical impedance of the system. The reciprocal of the impedance is the admittance; $Y(\omega) \equiv 1/Z(\omega)$.

The Fluctuation-Dissipation Theorem, derived by Callen et al. [86–88], states that the power spectrum $F_{therm}^2(\omega)$ of the fluctuating force is given by:

$$F_{therm}^2(\omega) = 4k_B T \Re(Z(\omega)), \quad (2.3)$$

where $\Re(Z)$ is the real (i.e. dissipative) part of the impedance and the power spectrum of the system's fluctuating motion can be given as:

$$x_{therm}^2(\omega) = \frac{4k_B}{\omega^2} T \Re[Y(\omega)]. \quad (2.4)$$

Taking a gas damped pendulum as an example [7], the equation of motion of the system, neglecting the fluctuating force, can be written as:

$$F = m\ddot{x} + b\dot{x} + kx, \quad (2.5)$$

where k represents the spring constant ($m\omega_0^2$) of the pendulum, and b is the damping coefficient.

The external force, F_{ext} , necessary to establish a given velocity \dot{x} , can be determined by expressing all of the forces in the frequency domain, and writing each term in terms of velocity, \dot{x} , i.e:

$$x = \frac{\dot{x}}{i\omega} \quad \text{and} \quad \ddot{x} = i\omega\dot{x} \quad (2.6)$$

The impedance, $Z \equiv F_{ext}/v$, can now be calculated to be:

$$Z \equiv b + i\omega m + \frac{ik}{\omega} \quad (2.7)$$

Using equation 2.7, the admittance of the system, $Y(\omega) \equiv Z^{-1}(\omega)$, becomes:

$$Y(\omega) = \frac{1}{b + i\omega m + \frac{ik}{\omega}}. \quad (2.8)$$

Next, the denominator is rationalised:

$$Y(\omega) = \frac{b - i\omega m + \frac{ik}{\omega}}{b^2 + (\omega m - \frac{k}{\omega})^2}. \quad (2.9)$$

Thus, the real part of the admittance can be determined and by noting that $k = \omega_0^2 m$, equation 2.4 becomes:

$$x_{therm}^2(\omega) = \frac{4k_B T b}{\omega^2 (b^2 + (\omega m - \frac{k}{\omega})^2)}, \quad (2.10)$$

providing an expression for the thermal noise power spectral density of an oscillator of resonant frequency ω_0 , in terms of its mass and damping coefficient.

2.2 Dissipation from Internal Friction in Materials

The example above illustrates that the thermal noise is related to the damping present in the system. In the case of a suspended mirror in a gravitational wave detector, where sources of external damping are suitably minimised, the relevant damping is the internal friction of the material.

Internal friction can be understood by considering the stress and strain in a mechanical system. Hooke's law (equation 2.11) defines the relationship between force and displacement, where δx is the amount by which a spring extends from a rest length of x upon the application of the force to the spring, F_{spr} .

$$F_{spr} = -k\delta x \quad (2.11)$$

The definition, a generalisation of Hooke's law, of the relationship between stress, σ , and strain, ε , is $\sigma = \varepsilon Y$, where Y is Young's modulus. However, this implies that a strain in the material is created instantaneously when stress is applied, whereas a real material would demonstrate anelasticity; i.e. the strain would lag behind the stress and the material would continue to stretch after the applied stress is removed. In this process energy is dissipated.

If a periodic stress, σ , given by:

$$\sigma = \sigma_0 e^{i\omega t}, \quad (2.12)$$

where σ_0 is the stress amplitude and ω is the angular frequency of the oscillation

is applied to an anelastic material, a strain response results, ε , such that:

$$\varepsilon = \varepsilon_0 e^{i(\omega t - \phi)}, \quad (2.13)$$

where ϕ is the *loss angle*, the angle by which the strain lags behind the stress. The loss angle is related to the internal friction of the material and is a measure of the fractional energy dissipated per cycle of oscillation [89].

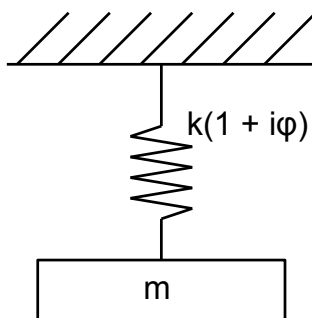


Figure 2.1: A diagram showing a mechanical oscillator with a complex spring constant $k(1 + i\phi)$.

The time delay between the applied stress and the strain response can be represented by a modified version of Hooke's law using a complex spring constant (shown in Figure 2.1). Thus, equation 2.11 becomes:

$$F_{spr} = -k(1 + i\phi(\omega))x, \quad (2.14)$$

where $\phi(\omega)$ represents the degree of anelasticity of the spring, and therefore the damping present due to the internal friction of the spring material.

If the resonant modes of the suspended mirror system in a gravitational wave detector are modeled as harmonic oscillators with internal damping, the equation of motion can be written as:

$$m\ddot{x} = -k(1 + i\phi(\omega))x + F. \quad (2.15)$$

Using equation 2.6, the force, F , on the oscillator becomes:

$$F = i\omega m\dot{x} + \frac{k}{i\omega}(1 + i\phi(\omega))\dot{x}, \quad (2.16)$$

and the impedance is:

$$Z = \frac{k - \omega^2 m + ik\phi(\omega)}{i\omega}. \quad (2.17)$$

By inverting equation 2.17, and rationalising the denominator, the admittance can therefore be found:

$$Y = \frac{\omega k\phi(\omega) + i(\omega k - m\omega^3)}{(k - m\omega^2)^2 + k^2\phi^2(\omega)}, \quad (2.18)$$

with the real part being:

$$\Re\{Y\} = \frac{\omega k\phi(\omega)}{(k - m\omega^2)^2 + k^2\phi^2(\omega)}. \quad (2.19)$$

Applying equation 2.4, and using $k = \omega_0^2 m$, the thermal noise power spectral density, $x^2(\omega)$, for a harmonic oscillator with internal friction $\phi(\omega)$ is therefore given by:

$$x_{therm}^2(\omega) = \frac{4k_B T \omega_0^2 \phi(\omega)}{m\omega[\phi^2(\omega)\omega_0^4 + (\omega_0^2 - \omega^2)^2]}. \quad (2.20)$$

2.3 Thermal Noise associated with a Single Resonant Mode

There are many resonant modes present in the mirror suspension system for a gravitational wave detector that can be thermally excited. These include the pendulum modes of the suspension, which occur at frequencies below the sensitive detection band of the interferometer, the violin modes of the suspension fibres, which lie within the detection band, and the internal modes of the

test mass mirror, which lie above the detection band. It is therefore the off-resonance thermal noise which limits the detector sensitivity for the pendulum and internal mirror modes.

It is possible to simplify equation 2.20 by looking at the thermal noise for each of the three cases: below the detection band, in the detection band and above the detection band.

Below the detection band, $\omega \ll \omega_0$:

$$x_{therm}(\omega) \approx \frac{4k_B T \phi(\omega)}{m\omega\omega_0^2(\phi^2(\omega) + 1)}. \quad (2.21)$$

Above the detection band, $\omega \gg \omega_0$:

$$x_{therm}(\omega) \approx \frac{4k_B T \omega_0^2 \phi(\omega)}{m\omega[\phi^2(\omega)\omega_0^4 + \omega^4]}. \quad (2.22)$$

In the detection band, $\omega \approx \omega_0$:

$$x_{therm}(\omega) \approx \frac{4k_B T \omega_0^2 \phi(\omega)}{m\phi^2(\omega)\omega^5}. \quad (2.23)$$

Using a low-loss material results in $\phi^2(\omega) \ll 1$, and the thermal noise in the detection band of the pendulum modes can be approximated as:

$$x_{therm}(\omega) \approx \frac{4k_B T \phi(\omega)}{m\omega\omega_0^2}. \quad (2.24)$$

Similarly, the thermal noise in the detection band due to the internal mirror modes can be approximated as:

$$x_{therm}(\omega) \approx \frac{4k_B T \omega_0^2 \phi(\omega)}{m\omega^5}, \quad (2.25)$$

and the contribution from the violin modes:

$$x_{therm}(\omega) \approx \frac{4k_B T}{m\omega_0^3 \phi(\omega_0)}. \quad (2.26)$$

Equations 2.24 and 2.25 show that the thermal noise power spectral density due to a resonance far from the detection band is directly proportional to the mechanical loss $\phi(\omega)$. Thus, the off-resonance thermal noise can be reduced for these modes, by using materials with low mechanical loss.

However, equation 2.26 shows that when the resonant mode is in the detector band, the power spectral density of thermal noise close to the resonance is inversely proportional to the mechanical loss.

By reducing the mechanical loss of the system through using a low loss suspension material, the thermal noise from the violin modes is effectively confined into a narrow frequency band centred on the resonance. This produces a narrower and higher thermal noise peak at the resonant frequency and lower off-resonance thermal noise. These peaks can then be easily filtered from the interferometer signal, without significantly reducing the useful bandwidth of the detector.

2.4 The Quality Factor, Q

The quality factor, Q , is a dimensionless measure of the dissipation of an oscillator at a resonant frequency, f_0 . It can be defined as:

$$Q(f_0) \equiv \frac{f_0}{\Delta f} \equiv \frac{2\pi E_{stored}}{E_{diss}}, \quad (2.27)$$

where Δf is the full width of the resonance peak in the frequency domain, measured at the level of half of the maximum power, E_{stored} is the total energy

stored in the resonating system, and E_{diss} is the energy dissipated with each cycle of oscillation. It can therefore be seen that an oscillator with a low level of energy dissipation will have a narrow resonance.

The quality factor can be related to the loss angle, ϕ , of the system. The loss angle is the angle by which the strain lags stress in an anelastic material and represents the proportion of total energy dissipated per oscillatory cycle:

$$\phi(\omega) = \frac{E_{diss}}{2\pi E_{stored}}. \quad (2.28)$$

At a resonant frequency, $\omega = \omega_0$, the mechanical loss angle is defined by $(1/Q(\omega_0))$. Away from the resonant frequencies $x_{therm}(\omega)$ is proportional to $\phi(\omega)$. The integral over all frequencies of the displacement power spectrum is independent of the amount of dissipation. By reducing the amount of dissipation (mechanical loss) in the test masses and suspensions, the thermal noise displacement spectral density away from the resonances can also be reduced, at the expense of an increase in the thermal noise spectral density at the resonant frequency.

2.5 Thermal Noise in a Multi-Resonance System

Previous discussion, and the thermal noise model described by equation 2.20, has focused on the thermal noise for a single resonance of a mechanical system. However, in an interferometric gravitational wave detector, the total thermal displacement from multiple resonant modes will be sensed by the laser beam reflecting from the front face of the mirror.

The mechanical dissipation of a real mirror, due to the presence of areas of

high loss such as the mirror coatings, or suspension fibre attachment points, is spatially inhomogeneous and thus the total thermal noise cannot be calculated by simply summing the individual modes [42].

Using the technique described by Levin [42], where a notional pressure of the same spatial profile as the intensity of the sensing beam to the front face of the substrate, the power spectral density of the thermal noise, S_x , can be written as:

$$S_x(f) = \frac{2k_B T W_{diss}}{\pi^2 f^2 F_0^2}, \quad (2.29)$$

where W_{diss} is the power dissipated when a notional oscillatory force of peak magnitude F_0 acts on the face of a test mass mirror.

If the loss is considered to be homogenous, and the laser beam radius is considerably smaller than the radius of the test mass, the test mass can be modeled as being half-infinite and the power spectral density of the Brownian thermal noise of the test mass can be shown to be [90]:

$$x_{therm}(\omega) = \frac{2k_B T (1 - \sigma^2)}{\pi^{3/2} f Y r_0} \phi_{substrate}(f) \quad (2.30)$$

where the test mass properties are: $\phi_{substrate}(f)$ is the mechanical loss, Y is the Young's modulus, and σ is the Poisson's ratio. r_0 is the radius of the laser beam where the electric field has fallen to $1/e$ of the maximum intensity.

Liu and Thorne [91] calculated a correction factor, C_{FTM} , for equation 2.30 for a finite test mass case, such that $x_{therm}^{FTM}(f) = C_{FTM}^2 x_{therm}^{ITM}(f)$, where x_{therm}^{FTM} is the thermal noise power spectral density of a finite test mass, as derived by Bondu [90] and corrected by Liu and Thorne [91]:

$$x_{therm}^{FTM}(f) = \frac{4k_B T}{\pi f} \phi_{substrate}(f) (U_o + \Delta U), \quad (2.31)$$

where $(U_o + \Delta U)$ represents the elastic deformation energy, defined explicitly

by Liu and Thorne [91].

2.5.1 The Arrhenius Equation

Internal friction is influenced by the arrangement of molecules inside the material. The time taken for an equilibrium strain to develop in response to an applied stress to the material is dependent on internal properties which are functions of the stress. Such properties include the density of point defects, dislocations, grain boundaries and impurities. In order for a new state of stress to be adjusted to, energy barriers of height ΔE must be overcome. This results in an exponential relaxation to the new equilibrium value, with a characteristic time τ which often obeys the Arrhenius equation [92]:

$$\tau = \tau_0 e^{\Delta E/k_B T}, \quad (2.32)$$

where τ_0 represents the characteristic time between attempts at crossing the energy barrier.

2.5.2 Debye Theory

Figure 2.2 shows a more accurate model of an anelastic material than the model shown in Figure 2.1. If a spring has only one significant internal relaxation process with a clearly defined energy barrier of ΔE , its dynamics can be represented using an undamped spring with constant k_1 in parallel with a Maxwell unit, a series combination of an undamped spring with constant k_2 , and a pure velocity damping dashpot, α .

Zener [93] showed that for such a model, the loss angle ϕ with a characteristic

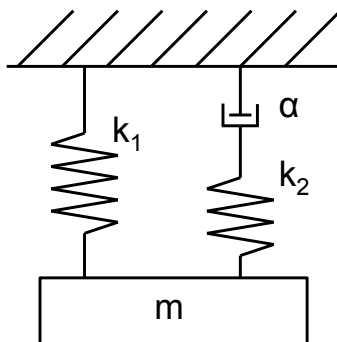


Figure 2.2: A diagram representing a typical anelastic solid, with an ideal spring connected in parallel with a spring-dashpot combination.

frequency dependence is given by:

$$\phi \approx \Delta \frac{\omega\tau}{1 + \omega^2\tau^2}, \quad (2.33)$$

where $\Delta \equiv k_2/k_1$ is the relaxation strength, and $\tau = \alpha/k_2$ is the relaxation time. The Debye peak is the dissipation peak at frequency $\omega_{peak} = \tau^{-1}$.

It has been reported that the internal friction is generally independent of frequency [7; 94–96], which may appear to contradict the Debye peak occurring at a characteristic frequency. It is possible, however, that a material may have several Debye peaks at frequencies separated by several orders of magnitude. At frequencies away from these peaks, the combined effect of the tails of the peaks is effectively constant with frequency.

2.6 Thermal Noise in a Gravitational Wave Detector

2.6.1 Coating Thermal Noise

When a laser is incident on the surface of a test mass, equation 2.29 shows that the level of thermal noise is directly related to the power dissipated in the test mass when a notional oscillating pressure is applied to the surface. At any point in the mass, the power dissipated is proportional to both the elastic energy associated with the deformations caused by the pressure and the mechanical loss at that point [42; 91].

The majority of the deformation will occur in the vicinity of the laser footprint on the test mass, therefore a dissipation source in this area will contribute more to the thermal noise read out by the laser beam than an identical source located further away.

Multi-layer dielectric coatings on the surfaces on the front surfaces of silica test masses in an interferometric gravitational wave detector have dissipation in the order of $2 - 4 \times 10^{-4}$ [43; 44; 97; 98] in comparison to the silica substrate, which has dissipation of $\sim 1 \times 10^{-9}$ [99]. Therefore, the thermal noise associated with the coatings will be dominant over the contribution from the substrate.

2.6.2 Suspension Thermal Noise

As discussed in section 2.3, the violin modes and pendulum modes both contribute to the thermal noise of the detector. Both of these sources arise from the pendulum suspension of the mirror used in interferometric detectors, as shown in Figure 2.3.

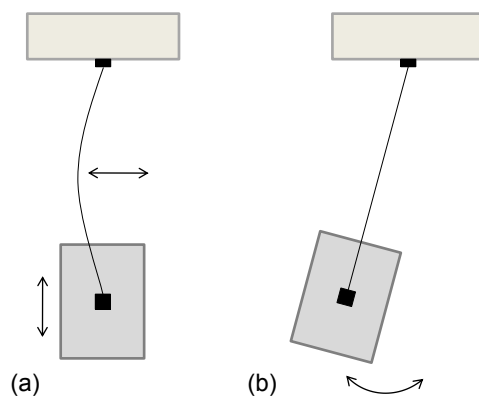


Figure 2.3: *Simplified diagram of (a) the fundamental violin mode, and (b) the pendulum mode of a suspended test mass.*

The loss factor of a pendulum is lower than that of the material used in the suspension fibres. This is because the majority of the energy in a pendulum is stored as potential energy via the Earth’s gravitational field, which is lossless, and only the fraction of the total energy stored in the flexing of the suspension fibres can be dissipated. This effect is known as ‘dilution’. Equation 2.34 shows the mechanical loss of a pendulum:

$$\phi_{\text{pendulum}} \approx \phi_{\text{fibre}} \frac{E_{\text{flex}}}{E_{\text{grav}}}. \quad (2.34)$$

Similarly, the loss of a violin mode is reduced from the intrinsic loss of the material by a dilution factor. If the loss in the suspension fibre is assumed to be spatially homogeneous and the rocking mode of the pendulum is constrained, the loss of the first violin mode will be twice that of the pendulum mode [100] [101]. The violin mode thermal displacement couples to the displacement of the test mass with a suppression factor of the ratio of the mass of the pendulum and fibre: $\frac{m}{m_{\text{fibre}}}$.

Section 2.3 described the thermal noise contributions from the pendulum and violin modes in equations 2.24 and 2.26, respectively. Another contributor to

thermal noise is the attachment points, known as the interface ‘ears’ that are bonded onto the side of the test masses in order for the suspension fibres to be welded into place. These can be seen for the GEO600 detector in the photograph in Figure 2.4.

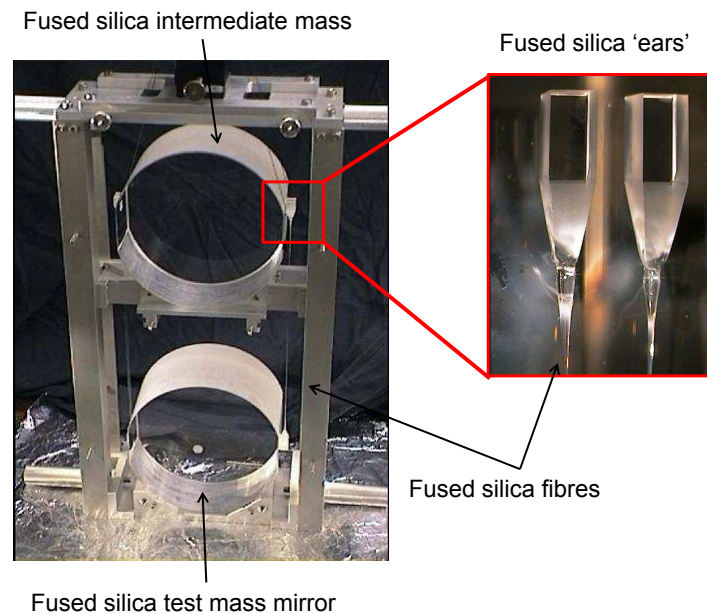


Figure 2.4: *Photograph of the GEO600 silica suspension, including the fused silica ears bonded onto the side of test masses. Credit: Albert Einstein Institute Hannover.*

2.6.3 Bond Loss

Experiments have shown that the method for attaching the suspension fibres to the test masses must be low loss to avoid degrading the pendulum mode loss factors [102]. Welding, which has been proved on small test masses, can produce substantial thermal stresses, increasing the chance of the substrate cracking [102].

An alternative technique, hydroxide-catalysis bonding, has been shown to be a low loss and high strength jointing technique for silica suspensions [103]. Investigations have been made into the mechanical loss of a hydroxide-catalysis

bond between both silica and sapphire [104], and it has been applied in the GEO600 suspension, and included in the upgrades for LIGO and Virgo: fused silica ‘ears’ are bonded onto the side of silica test masses to provide an interface for the suspension fibre to be welded to.

Hydroxide-catalysis bonding, due to its desirable properties including high strength and insensitivity to temperature [103], is under consideration for future developments of gravitational wave detectors.

2.7 Conclusion

The sensitive operating band of an interferometric gravitational wave detector is limited in its most sensitive frequency range by thermal noise. The mechanical loss of the materials used in the construction of the test masses and suspension systems is directly related to the level of thermal noise in the detector.

The use of low loss materials can therefore reduce the level of thermal noise, as can a lower operating temperature, and the careful positioning of higher loss sources away from the front face of the test mass mirror.

The construction of the pendulum suspension can also be a significant source of thermal noise. The method of bonding the interface ‘ears’ onto the sides of the test mass mirrors in order to create a quasi-monolithic suspension, will be the focus of this thesis, with measurements of the mechanical loss of a hydroxide-catalysis bond (as used in GEO600 and planned for use in Advanced LIGO and Virgo) measured in Chapter 5, and the application of the process for future generation gravitational wave detectors.

Chapter 3

Hydroxide-Catalysis Bond Strength Testing

3.1 Introduction

The technique of hydroxide-catalysis (silicate) bonding was invented and patented at Stanford University by Gwo [105; 106] for jointing fused silica pieces in the Gravity Probe B space experiment [107]. The technique was adapted for use in the construction of the final stages of the GEO600 suspension systems [103] due to the high bond strength [106] and suitably low mechanical loss, and for the high stability optical benches for the proposed ‘LISA’ mission, a space-based gravitational wave detector [108], due to the ability of the bonds to withstand the forces and thermal cycling associated with space launches and conditions [107; 108].

In the GEO600 detector, the hydroxide-catalysis bonding technique was used to joint the relevant silica attachments to the test masses as it was shown to add very little additional noise to the suspension system, because of a combination of its level of mechanical loss [103; 104], small bond thickness and high

mechanical strength [105]. Additionally it is vacuum compatible and allows for precision alignment of pieces [108].

As discussed in Chapter 1, the technique is being used in a similar way in upgrades to the suspensions of the LIGO [55] and Virgo [27] detectors to form ‘Advanced’ detector systems which should be operational around 2014. These advanced instruments should have a factor of 10 to 15 times better sensitivity than first generation detectors [27; 55]. The technique of hydroxide-catalysis bonding has also been proposed for use in the construction of silicon suspensions in future generations of cryogenic gravitational wave detectors [79].

3.2 Hydroxide-Catalysis Bonding

The hydroxide-catalysis bonding technique achieves the formation of a bond between surfaces through hydroxide-catalyzed hydration and dehydration. To form a bond, hydroxide ions (ideally in an aqueous solution) are deposited onto at least one of the surfaces. The two surfaces are then placed in contact with each other such that a chemical bond can form between the surfaces to be jointed. NaOH, KOH, and NH_4OH , are all hydroxides suitable for this use in an aqueous solution [106].

Ideally the surfaces to be jointed are required to be a material such as silica, fused silica, silicon with a surface oxide layer, natural or fused quartz, that can form a silicate-like network, or one which can be chemically linked to a silicate-like network, through hydroxide-catalyzed hydration and dehydration. These surfaces can be bonded together, or to another material such as alumina, which has oxygen present at the bonding surface that is able to form bonds with the silicate molecules. Alternatively, it is possible to bond two alumina surfaces together through the addition of silicate to the bonding solution.

The hydration and dehydration process can be catalyzed by H^+ , OH^- , and alkali metal ions. The use of a catalyst lowers the activation energy, E_a , of the dehydration process to less than a few $k_B T$ (where k_B is Boltzmann's constant and T is the temperature in Kelvin). This enables the hydration and dehydration process to easily occur at room temperature.

Hydration of fused silica is shown in Figure 3.2. The bulk of fused silica comprises a network of siloxane bridges ($Si-O-Si$), some of which are highlighted in red. When exposed to water and hydroxide ions (OH^-), the silicon and oxygen atoms can be hydrated to form $Si-O-H$ groups, shown on the right in Figure 3.2.

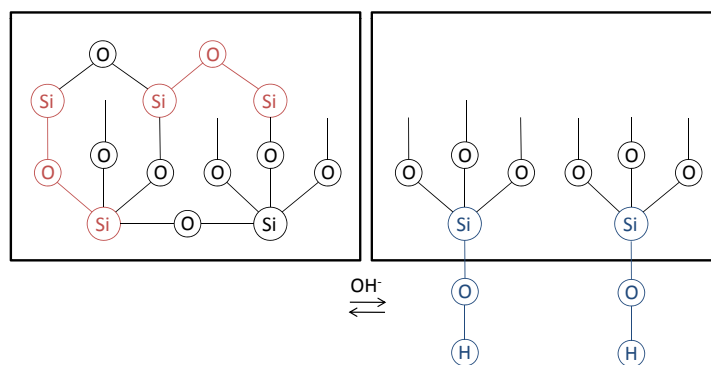


Figure 3.1: *Fused silica (left) with siloxane bridges highlighted in red. When fused silica is exposed to water and hydroxide ions, it becomes hydrated and $Si-O-H$ structural groups are formed (right, highlighted in blue).*

The dehydration process is shown in Figure 3.2. Two hydrated fused silica surfaces are placed close together, and an oxygen atom from one surface combines with one hydrogen atom from each of the two surfaces and is removed as a water molecule, resulting in the formation of a siloxane bridge. This process of chemical bonding results in the surfaces being bonded together with great strength.

The steps described in the text and figures above for fused silica can also be represented using equations 3.1, 3.2 and 3.3.

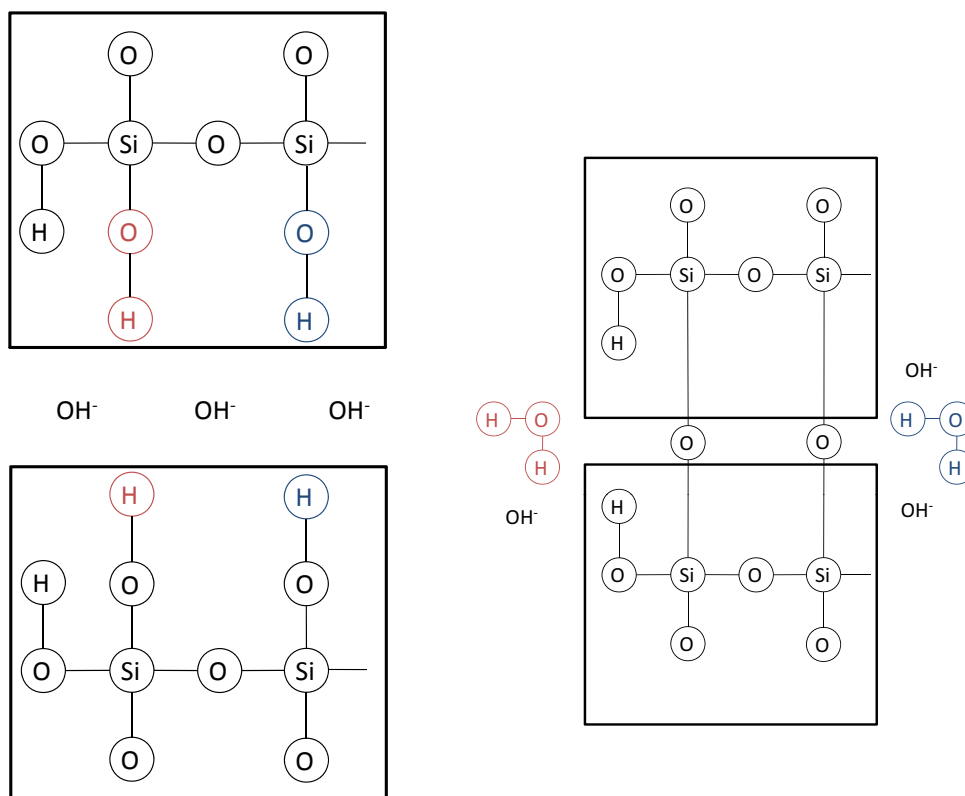
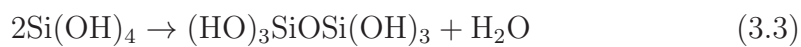
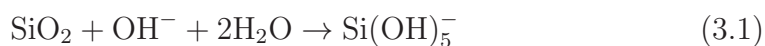


Figure 3.2: *The formation of the silicate bond. On the left, hydrated fused silica is in the presence of hydroxide ions. The red and blue atoms highlighted are removed during the dehydration process to form water molecules, and a siloxane bridge forms between the two surfaces.*



The bond will form if the two surfaces are close enough to each other; if both surfaces are perfectly flat this requirement is met by simply placing the two surfaces against each other. However, a perfectly flat surface is unlikely; in reality such a surface does not exist. For surfaces whose figures are slightly mismatched, the silicate-like networks that are formed (Figure 3.2) are able to

fill small gaps.

Although alternative techniques exist for use in jointing pairs of surfaces that have large amounts of surface mismatch (such as using a powder or slurry of materials than can be hydrated to have surface hydroxyl groups). For the application of hydroxide-catalysis bonding in the construction of suspensions in gravitational wave detectors, the bonding surfaces ideally have global surface figures that match to within 60 nm peak-to-valley. This enables bonds to be created using an aqueous bonding solution in order to create very thin bonds with high precision.

The time taken for a bond to form can be controlled by altering temperature and/or pH of the bonding solution used [106; 109]. The bond thickness between fused silica surfaces of nominal flatness 60 nm has been found to be approximately 60 nm - 100 nm when the bonding surfaces had a global flatness of $\leq \lambda/10$, where $\lambda = 633$ nm [108; 110].

3.2.1 Hydroxide-Catalysis Bonds between Silicon

Untreated silicon cannot be reliably bonded using this technique. To make bonding of silicon components possible, the bonding surfaces must ideally have a surface coating of SiO_2 , with which the hydroxide can react to form the bond [106].

A suitable layer can be deposited in a variety of ways. Previous studies of bonding silicon and silicon carbide [111] seemed to suggest that the nature of the silicon oxide layer played a role in determining the success of the bonding process. In [112] it was postulated that if hydrogen formed during the bonding process due to direct contact between silicon and aqueous hydroxide solution, this might have a detrimental effect on the resulting bond strength.

It was therefore proposed that oxide layer thickness might have an effect on strength, i.e. that a minimum thickness of surface oxide layer is required to create reliably strong bonds. In this chapter this hypothesis is investigated by creating a number of samples whose surfaces have wet thermal oxide layers of varying thickness applied to them, bonding pairs of such samples together, and strength testing the resultant bonds.

Van Veggel et al. [111] showed bending strengths could be achieved averaging 23 MPa in hydroxide-catalysis bonds between silicon carbide bonds and shear strengths averaging 3.9 MPa were achieved between silicon at room temperature [112]. However, the silicon samples were loaded in such a way that shear forces dominated the experiments, the results of which were thought to be limited by the way the samples were clamped. The bending stress in silicon-silicon bonds were measured by Dari et al. [82] to be approximately 8.7 ± 3.7 MPa at room temperature.

3.3 Thermal Oxidation of Silicon

3.3.1 Introduction

The Deal and Grove model [113] describes the thermal oxidation of silicon, which typically occurs between 800 and 1200°C. Silicon with a surface oxide layer of thickness D , will grow an oxide layer through the inward movement of the species of oxidant rather than by the outward movement of silicon. The transported species will go through three stages; initially it is transported from the bulk of the oxidising gas to the outer surface where it reacts or is adsorbed. Then, it is transported across the oxide film towards the silicon. Finally, it will react at the silicon surface to form a new layer of SiO_2 [113].

Silicon is easily oxidised in air: a native oxide of nanometre thickness grows on

the silicon surface in a couple of hours or days, depending on surface conditions. This native oxide, however, is limited in its thickness and is not stoichiometric SiO_2 . High quality thermal oxides can be grown at temperatures above 800°C [114].

There are two basic schemes used for thermal oxidation of silicon; wet and dry, the processes of which are described in equations 3.4 and 3.5 respectively, where (s) and (g) denote a solid and a gas respectively. During dry thermal oxidation, oxygen will diffuse through the SiO_2 film and react at the SiO_2/Si interface. Si is consumed when silicon and oxygen react to form SiO_2 . For an SiO_2 layer of thickness D , a thickness of $0.45D$ of silicon is consumed.



The rate at which an oxide layer will form on the surface of silicon is dependent on several factors, including the orientation of the silicon ingot and the oxidation method used. Oxygen molecules will diffuse through SiO_2 faster than water molecules. However as water solubility in SiO_2 is four orders of magnitude larger than that of oxygen, the higher concentration of the oxidant in the oxide results in wet thermal oxidation producing an oxide layer at a faster rate than dry oxidation.

There are several other factors that can influence the oxidation rate, including the doping level (highly doped silicon will oxidise faster than a lightly doped material [114]), the pressure at which the oxidation takes place (a higher oxygen pressure results in a faster oxide growth [114]) and the crystal orientation. Silicon $\langle 111 \rangle$ will oxidise at a faster rate than silicon $\langle 100 \rangle$ because of a higher number of silicon bonds being available at the surface. This also influences the quality of an oxide layer, and a slowly grown oxide layer is more

dense and of a higher quality than an oxide layer grown quickly [115].

Here, all samples were oxidised at atmospheric pressure. The different crystallographic orientations were not considered when selecting oxidation times due to the small influence this was expected to have on the oxide layer growth rate given the uncalibrated oxidation set-up [115].

3.3.2 Oxidation Procedure

For the strength tests rectangular silicon blocks of dimensions $20\text{ mm} \times 10\text{ mm} \times 5\text{ mm}$ cut from two different silicon ingots were used. Both ingots were manufactured by Prolog; ingot one had a $\langle 111 \rangle$ crystal orientation, ingot two had a $\langle 100 \rangle$ crystal orientation, as shown in Figure 3.3. The bonding surfaces were formed from one of the $5\text{ mm} \times 10\text{ mm}$ surfaces on each sample, so that after bonding a composite sample was created with dimensions $40\text{ mm} \times 10\text{ mm} \times 5\text{ mm}$.

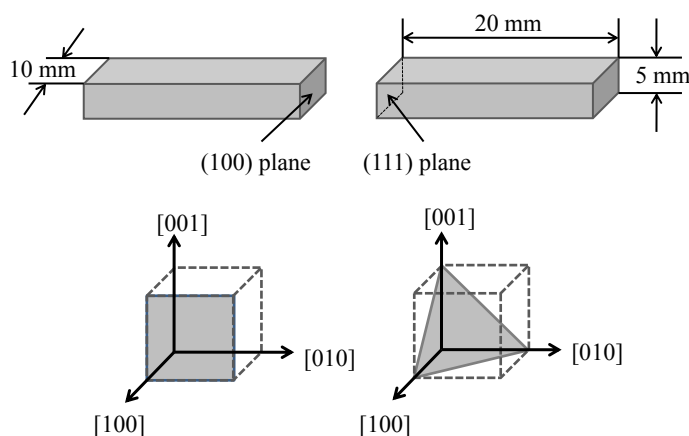


Figure 3.3: Diagram showing a ‘mixed’ ingot pairing. The bonding surface on each block is $5\text{ mm} \times 10\text{ mm}$, and for a mixed ingot pairing, a $\langle 111 \rangle$ block is bonded to a block of orientation $\langle 100 \rangle$.

In order to remove any organic residue on the bonding surfaces prior to oxidation an acid clean, using a 1:7 volumetric ratio of hydrogen peroxide and sulphuric acid, known as ‘piranha solution’, was performed on all samples.

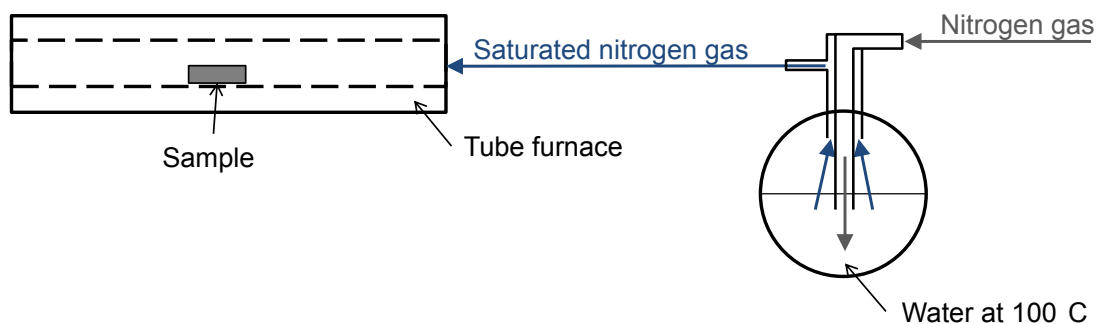


Figure 3.4: Schematic for a wet thermal oxidation.

Figure 3.4 shows a schematic diagram for the wet thermal oxidation set up: nitrogen gas is passed through boiling water and subsequently passed over the samples which are contained in a furnace, over the samples. This introduces water into the hot environment and as described in Section 3.3.1, accelerates the growth of the oxide layer on the silicon surface.

The silicon blocks were placed on a fused silica 'boat' with the bonding surfaces exposed to the environment (shown in Figure 3.5) and placed into the centre of the tube once the temperature had reached 1000°C, and the gas flow had been started. The samples inside the furnace can be seen in Figure 3.6.

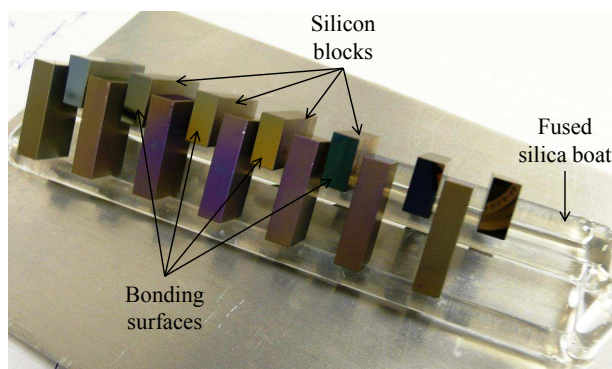


Figure 3.5: Silicon samples on a fused silica boat, after oxidation. The bonding surfaces were exposed to the saturated nitrogen gas flow. The variations in colour are due to different thicknesses of oxide layers present on the surface.

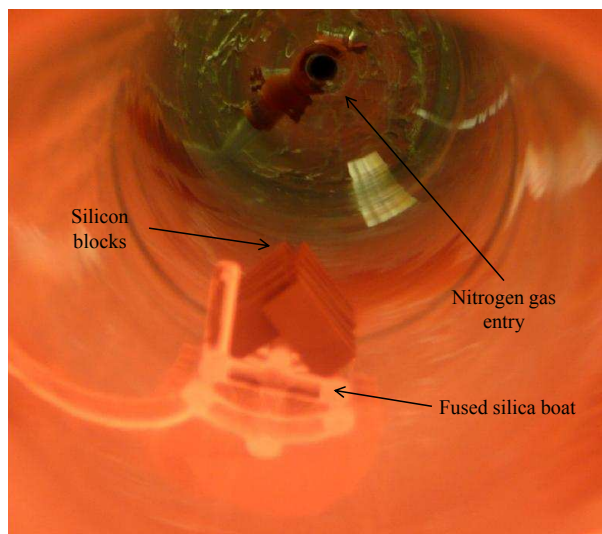


Figure 3.6: *Silicon samples in the furnace.*

Previous experiments found the growth rate for an oxide layer on silicon in a wet environment to be lower than that predicted by the model proposed by Deal and Grove [112; 113]: samples oxidised for 18 minutes grew oxide layers of approximately 84 nm [112]. Therefore, oxidation times were chosen to be between 5 and 55 minutes to grow oxide layers up to ~ 200 nm.

However, it was discovered that some of the oxide layers grown were not as thick as expected. Therefore, in order to get a good range of oxide layer thicknesses, it was necessary to re-oxidise some of the samples. The oxidised blocks were put back into the tube furnace (in the same environment as before) to ‘top-up’ the oxide layer. The resulting oxide layer was measured and assumed to be a single oxide layer and the oxidation time was considered to be the total time the sample spent inside the furnace.

Figure 3.7 shows a plot of the oxidation time and resultant oxide layer thickness for both the $\langle 111 \rangle$ and $\langle 100 \rangle$ ingots. It is apparent that the ingot with the $\langle 111 \rangle$ crystallographic orientation formed an oxide layer at a greater rate than the ingot with the $\langle 100 \rangle$ orientation. There are also anomalous results for the samples oxidised for 30 minutes that do not follow the general trend.

It is postulated that these are due to variations in the oxidation conditions. For example, it is possible that when the nitrogen gas passes through the boiling water, some water could get splashed into the pipe, preventing constant gas flow into the furnace and also get passed into the furnace, increasing the humidity inside the furnace.

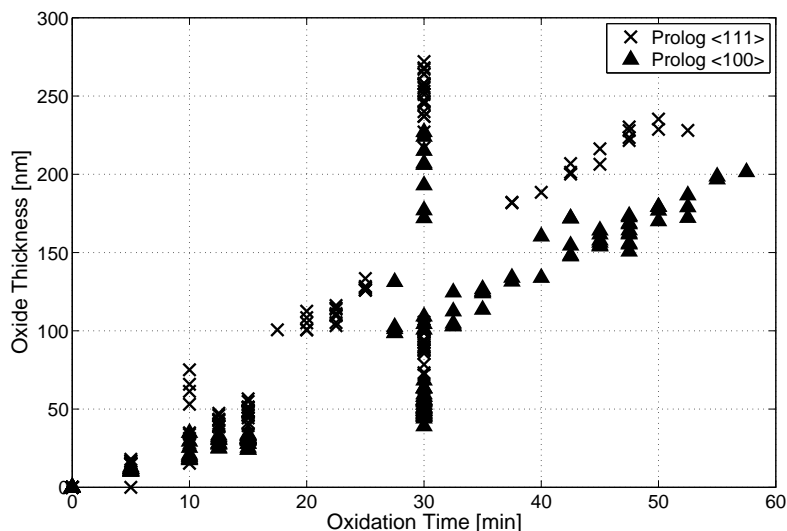


Figure 3.7: Plot showing the measured relationship between oxide layer thickness and oxidation time in a wet thermal environment.

The oxide thicknesses were measured using ellipsometry. An ellipsometer measures the change in the polarisation state of light when it is reflected from a sample. If linearly polarised light of a known orientation is reflected at an oblique incidence from a surface, the reflected light is elliptically polarised. The shape and orientation of the ellipse depends on the angle of incidence, the direction of the polarisation of the incident light, and the reflection properties of the surface. The presence of a thin film on the surface (such as an oxide layer) will change the reflection properties such that the thickness of the film can be determined. The thickness of the oxide layer grown on each sample was measured at a central point on the oxidised bonding surface.

3.4 Bonding Procedure

The bonding surfaces of all samples were polished to a nominal flatness of $\lambda/10$ where $\lambda=633\text{ nm}$. The flatness of the bonding surface was measured after oxidation using a Zygo GPI XP/D interferometer operating at 633 nm. All samples were marked with identification numbers, to allow the bonds to be characterized and tracked throughout the experimental process.

The Zygo interferometer was used to measure the flatness of each sample, shown in Figure 3.8. Examples of the resulting images for samples with low flatness peak-valley (PV) values are shown in Figure 3.9. High flatness values are often caused by edge effects on the samples, shown in Figure 3.10.

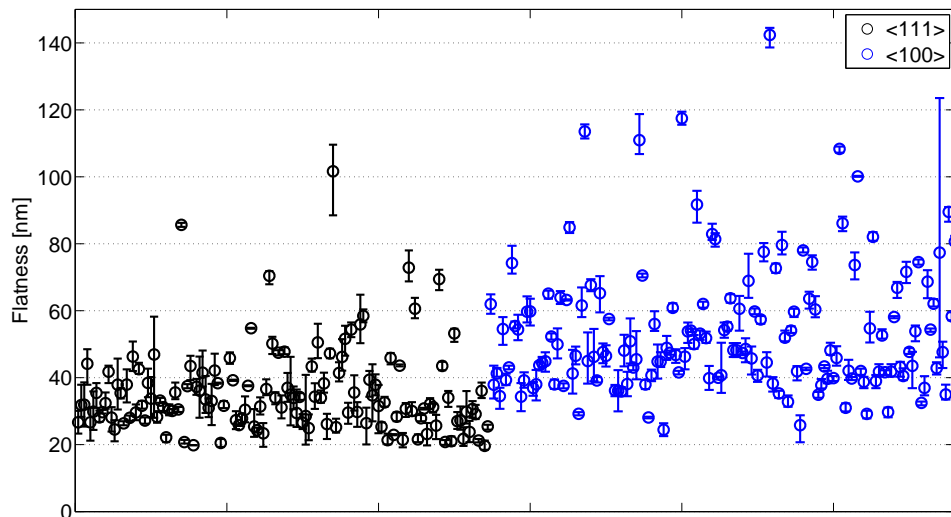
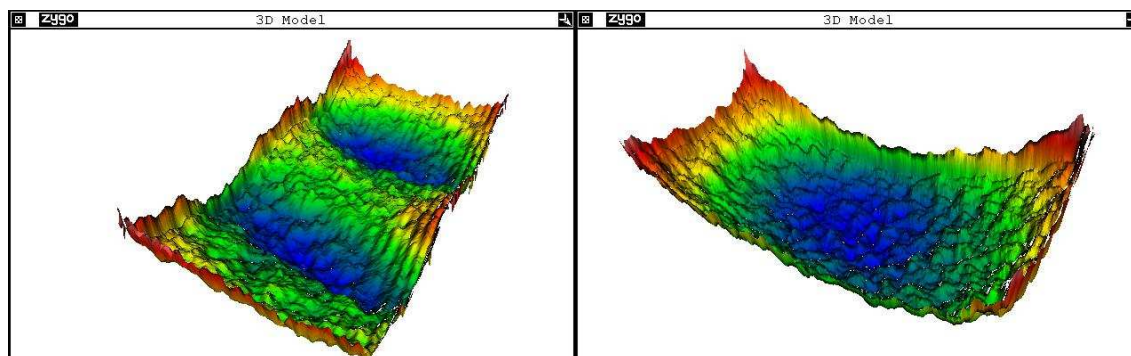


Figure 3.8: *The measured flatness of the bonding surface of each silicon block after oxidation.*

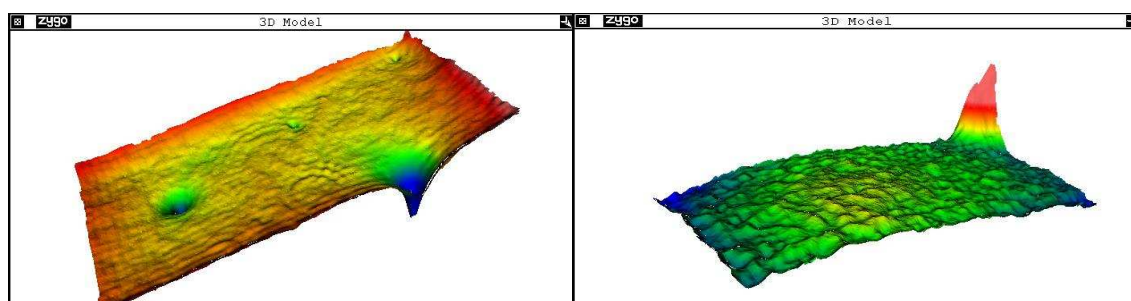
The roughness of selected samples was also measured using a Veeco Wyko NT1100 Optical surface profiler which uses a phase shift technique. The results from the measurements, shown in Figure 3.11, showed the oxide layers grown using the experimental set up shown in Figure 3.4 to be suitably smooth.



(a) 27.02 nm PV flatness

(b) 27.07 nm PV flatness

Figure 3.9: Two samples with Peak to Valley (PV) flatnesses of less than 30 nm.



(a) 116.78 nm

(b) 111.86 nm

Figure 3.10: Two samples with features that produce flatnesses of above 100 nm.

The bonding procedure took place on a class 100 flow bench, and the bonding surfaces were cleaned using a procedure consisting of polishing with cerium oxide in de-ionised water followed by cleaning with sodium bicarbonate, a methanol rinse and a methanol drag wipe immediately prior to bonding. By ensuring the surface is hydrophillic prior to bonding, any hydrophobicity which may be due to organic or silicone contamination, is minimised along with any surface particulate contamination.

The bonding solution was dispensed onto the surfaces using a pipette, where $0.4 \mu\text{l}$ of solution per cm^2 ($0.2 \mu\text{l}$ for the strength test samples) was used. The bonding solution was produced by diluting a commercially available sodium

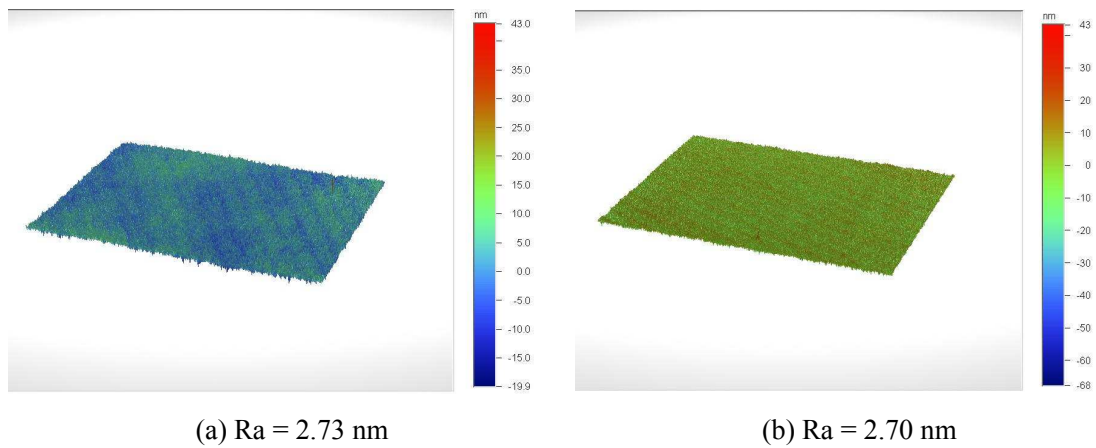


Figure 3.11: *Two samples with showing low levels of surface roughness, with Ra being the arithmetic average of the absolute values of the vertical deviations of the roughness profile from the mean line.*

silicate solution (14% NaOH and 27% SiO₂) with de-ionized water at a volumetric ratio of 1:6, a solution used previously [108].

Occasionally, localised point-like surface features in the oxidised surface were seen on the bonding surface. An example of defects on the surface is shown in Figure 3.12. These are postulated to be due to particulate contamination during the oxidation process. Any surface features visible on the bonding surface, such as the specks visible in Figure 3.12, were recorded.

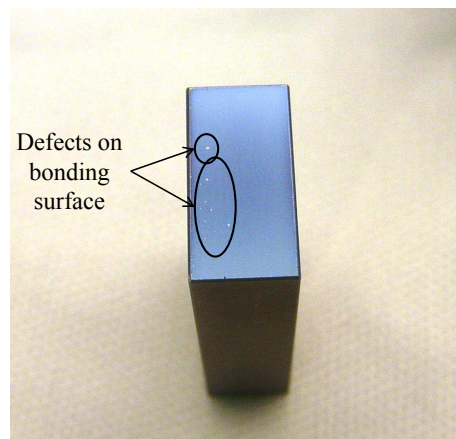


Figure 3.12: *Photograph of a block with specks visible on the oxidised bonding surface.*

All samples were left to cure at room temperature for a minimum period of 4 weeks in a clean room environment at room temperature.

3.4.1 Bonding Native Oxides

Some silicon blocks were bonded with no thermal oxide layer grown on the bonding surface to investigate the minimum amount of oxide layer required for a bond to form. It was noted that the cleaning procedure using cerium oxide failed to make the native oxide layer hydrophilic, unlike the thermal oxide layers, preventing the droplet of bonding solution from spreading across the bonding surface. This effect is shown in Figure 3.13.

Six of the bonds involving samples with native oxides failed to form correctly. Figure 3.14 shows the bonding surface of a failed bond between two native oxide layers.

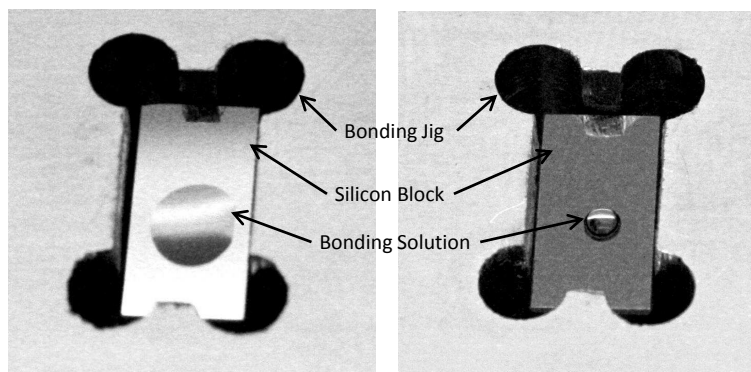


Figure 3.13: *Photograph showing the effect of hydrophilic surface conditions on the spread of bonding solution. The image on the right shows a hydrophobic bonding surface, due to cerium oxide cleaning procedure being ineffective on the native oxide layer. On the left, a hydrophilic thermal oxide layer is shown. The drop on the hydrophilic surface has spread much more than that on the hydrophobic surface.*



Figure 3.14: Image showing the surface of a sample of two native oxide blocks that failed to bond.

3.5 Four Point Bend Strength Tests

3.5.1 Experimental Set-up

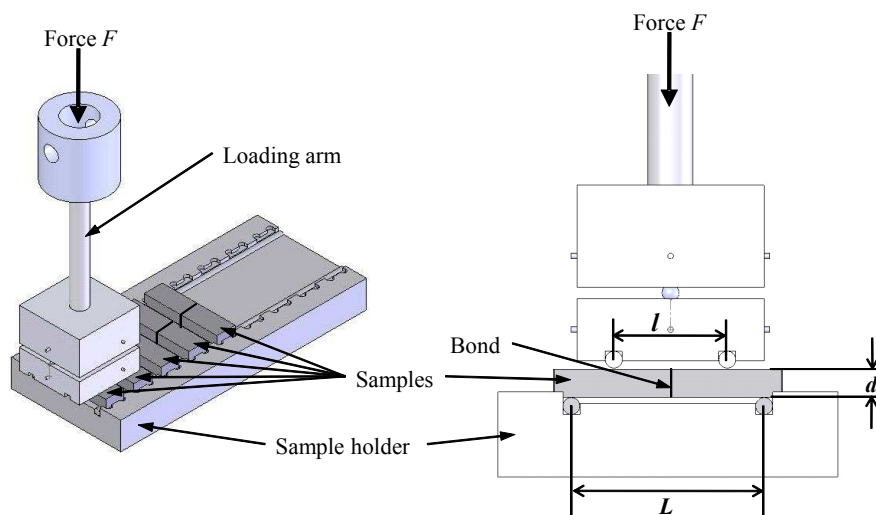


Figure 3.15: 3D and detail CAD images of the bending strength set-up. The sample holder was placed in a teflon bath, which was filled with liquid nitrogen for the cryogenic tests.

The bond strength was determined using a four point bend test whose geometry is shown in Figure 3.15, which is consistent with ASTM standard C 1161-2C [116] for breaking brittle materials (like ceramics and glass). The samples were placed on the holder of the setup and a downwards force, F , was applied

using Zwick-Roell static 2 kN and 200 kN machines through a loading arm and measured until the sample broke. The supports underneath the sample are placed at a distance $L=34$ mm, and the force is applied equally through two points on top of the sample at a distance $l=20$ mm apart, with both distances centered at the bond.

The strength was calculated using (3.6) below where F is the force, L is the distance between the bottom supports, b is the width of the sample and d is the thickness of the sample [116].

$$\sigma_{\max} = \frac{3(L - l)F}{2bd^2} \quad (3.6)$$

Measurements were performed at room temperature and at ~ 77 K. The latter cryogenic measurements were performed by submerging the samples in liquid nitrogen and waiting for thermal equilibrium by observing the settling of the nitrogen after boiling before conducting the strength test.

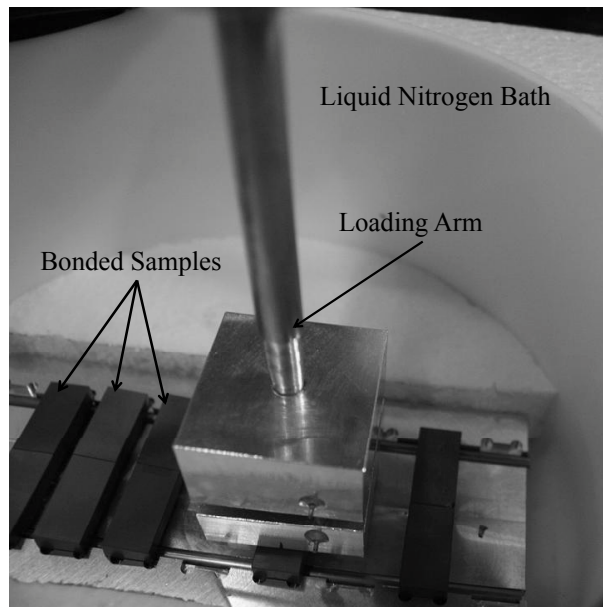


Figure 3.16: Image showing the test set up; to cool the samples down to ~ 77 K, the bath was filled with liquid nitrogen.

Ansys¹ analysis was performed in order to predict the effect of the oxide layer thickness on the bond strength, as shown in Figure 3.17. Ansys is a general purpose finite element modeling package used for numerically solving mechanical problems. However, the small size of the bond and oxide layers in comparison to the overall sample size did not allow any conclusions to be drawn.

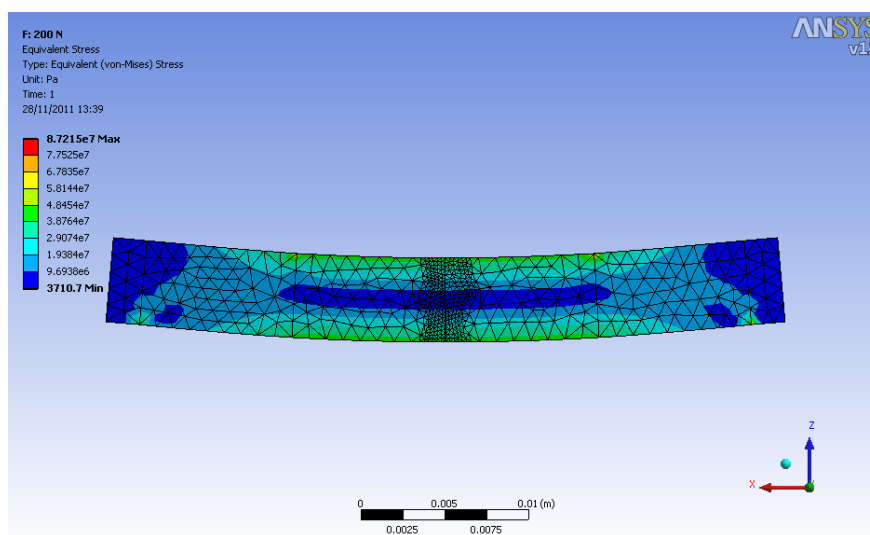


Figure 3.17: *Ansys analysis showing the equivalent stress on the bonded sample, applying a 200 N force.*

3.5.2 Results

In total, 135 bonded samples were strength tested; 86 at ~ 77 K, and 49 at room temperature. Five samples failed to bond. Figure 3.18 shows how the breaking strength of the samples varied with the minimum oxide layer thickness (t_{\min}) found on the surface of each sample. Three main features can be identified. Firstly, when looking only at the cryogenic temperature results, there is a clear trend of decreasing strength once the minimum oxide layer is less than 50 nm. Secondly, when comparing cryogenic to room temperature

¹www.ansys.com/en_uk

results at comparable oxide layer thicknesses there appears to be no significant difference in strengths indicating that the strength of the bonds is not negatively influenced by thermal loading due to expansion differences between the bond material (silicon dioxide and siloxane chains) and the bulk material (silicon). Lastly, there appears to be a grouping of samples that lie in the $75 \text{ nm} < t_{\text{min}} < 260 \text{ nm}$ that have somewhat lower strength (less than 30 MPa) than the remainder of the samples.

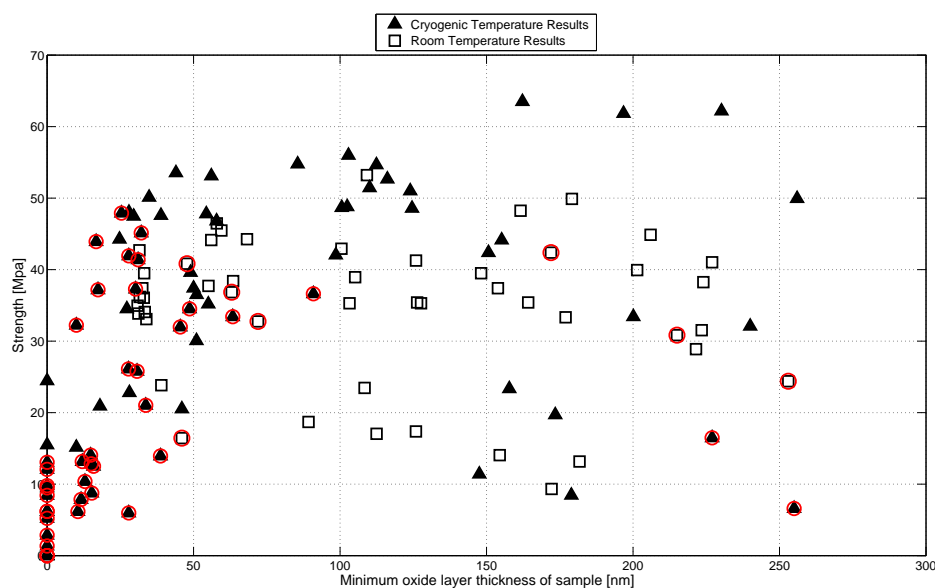


Figure 3.18: *Plot showing the strength of all samples tested. When the minimum oxide layer thickness exceeds 50 nm, the strengths appear to become, on average, more reliable.*

3.5.3 Analysis

Due to the brittleness of the samples, a statistical variation could be expected to be seen in their strengths. This occurs because a fracture may originate at flaws in the material itself and therefore the strength will depend upon the probability of there being a flaw that is large enough to cause a fracture normal to the direction of the maximum tensile stress.

The variations in strength of such materials are generally modeled by a Weibull distribution [117] rather than, for example, a Gaussian distribution. The Weibull distribution is commonly used in modeling extreme or critical phenomena or in survival and reliability analysis where one wishes to estimate the ‘time to failure’ of an industrial or mechanical process. In particular the Weibull distribution can be strongly skewed and is thus appropriate for modeling statistical variations which are not symmetric with respect to some given characteristic behaviour — such as one may encounter when considering the distribution of breaking strengths.

The two-parameter Weibull distribution has a probability density function (pdf), denoted $P(F)$, given by equation 3.7:

$$P(F) = \frac{m}{F_0} \left(\frac{F}{F_0} \right)^{m-1} \exp \left[- \left(\frac{F}{F_0} \right)^m \right] \quad (3.7)$$

where the Weibull modulus, m , provides a measure of the variability of the material property measured — with increasing Weibull modulus indicating a smaller range of variability. The parameter F_0 represents a characteristic strength for the distribution. The combination of these two parameters permits comparison between data sets acquired from similar experiments, in order to explore and identify factors that might influence the strength of the data sets. An example of a Weibull distribution is shown in Figure 3.19.

In previous literature on breaking strength (see [117]) estimation of m and F_0 has generally been carried out in terms of the cumulative distribution that corresponds to the pdf of equation 3.7. The measured strengths and estimated cumulative probabilities for the data set are transformed into new variables related to m and F_0 via a simple straight line dependence [117]. Fits to these parameters are then obtained via, for example, linear regression. However this approach generally assumes that the scatter about the regression line is

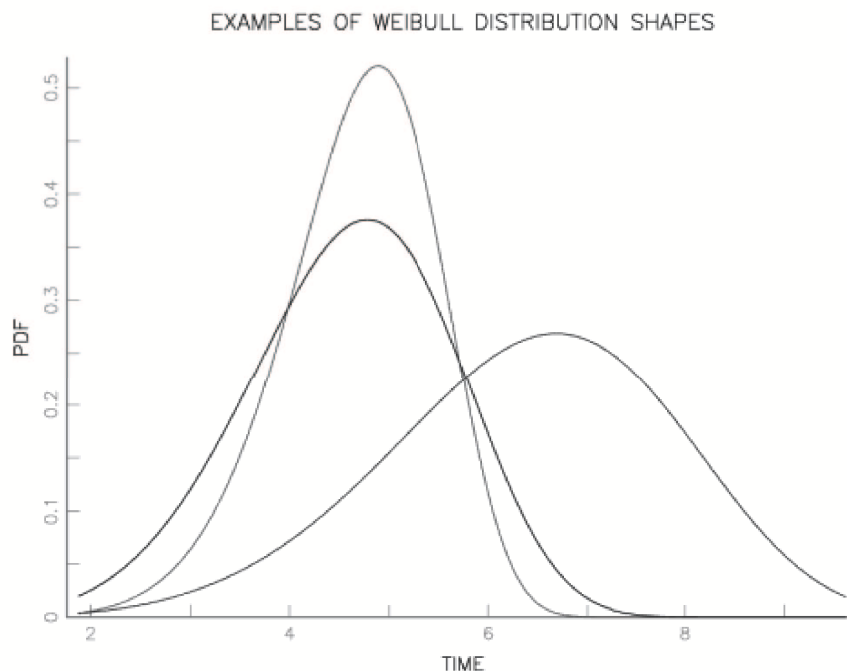


Figure 3.19: *An example of different Weibull distributions. Taken from [118].*

Gaussian — an assumption that may be questionable given the highly skewed nature of the original Weibull distribution.

In the analysis carried out here, an alternative approach using a Bayesian analysis was carried out that simultaneously estimates m and F_0 directly from the Weibull pdf and requires no such Gaussian assumption. Moreover we use a Markov Chain Monte Carlo method [119] to obtain confidence regions for our fitted Weibull parameters. Equation 3.8 shows the joint likelihood function, assuming that all the measured F_i values are independently and identically distributed from the Weibull probability function (pdf). For a continuous variable F , the pdf tells us the probability of any particular value of parameter F , and is peaked at the most likely value.

$$L(F_1, \dots, F_N) = \prod_{i=1}^N \left(\frac{m}{F_0} \right) \left(\frac{F_i}{F_0} \right)^{m-1} \exp \left[- \left(\frac{F_i}{F_0} \right)^m \right] \quad (3.8)$$

Using Bayes' theorem, inferences can be made about m and F_0 , using equation 3.9. This states the posterior probability $p(m, F_0|\text{data})$ of a particular hypothesis is based on the data, the prior probability $p(m, F_0)$, and the likelihood function $p(\text{data}|m, F_0)$.

$$p(m, F_0|\text{data}) = p(\text{data}|m, F_0)p(m, F_0) \quad (3.9)$$

The prior pdf is taken to be broad and flat, as little is known about the hypothesis prior to the analysis, resulting in the posterior being proportional to the likelihood function. Since the maximum of the log likelihood is equal to the maximum of the likelihood, we work with the log likelihood given by equation 3.10.

$$\ell(m, F_0) = N \ln(m) - mN \ln(F_0) + (m - 1) \sum_{i=1}^N \ln(F_i) - (F_0^{-m}) \sum_{i=1}^N F_i^m \quad (3.10)$$

Figure 3.21 shows estimates of the m parameter (top figure) and F_0 parameter (bottom figure) for all data sets, determined by marginalizing the joint posterior distribution of m and F_0 . Here the markers indicate the mode of the marginalized posterior and the error bars indicate the central 68% of the distribution (also visible in Figure 3.20). It can be seen that the values for the Weibull modulus and characteristic strength vary when different factors are taken into account. The low value of m for the full data sets indicates that there may be several factors affecting the strength of the samples. Some possible factors were identified during the experiment and filters were applied in order to identify which of these factors influence the characteristic strength and spread of results, as shown in Table 3.1. Initially, a minimum oxide layer thickness filter was applied. The value of 50 nm was selected after inspection of Figure 3.18 as discussed earlier, in which a clustering of low strength samples for oxide thicknesses below 50 nm can be seen.

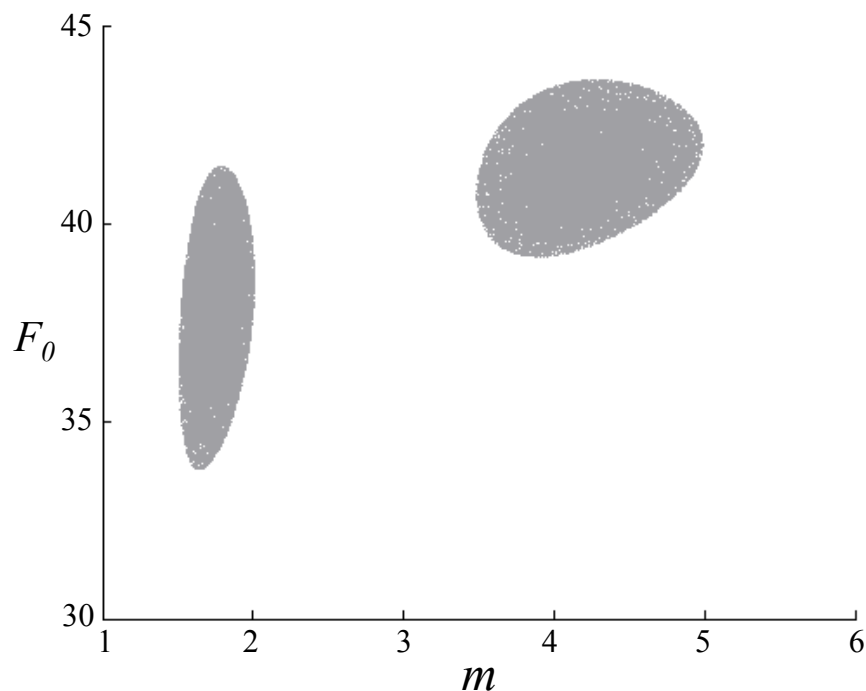


Figure 3.20: *Joint 68% confidence regions for the Weibull parameters m and F_0 , obtained from a Bayesian analysis of all cryogenic (left) and room temperature (right) strength results.*

There appears to be no correlation between the minimum oxide layer thickness on the pair of bonding surfaces for each sample and the strength of the sample when the minimum oxide layer thickness on the bonding surfaces is between 50 nm and 250 nm. This is of importance because the goal is to minimize the thickness of the overall oxide and bond layer as far as possible for application in third generation gravitational wave detectors, due to the direct relationship between the thickness of the oxide layer and bond and the thermal noise resulting from the bond [120].

A significant limitation with this analysis is the small number of data points after certain filters are applied. However, a clear effect is seen when considering the results obtained at cryogenic temperature in Figure 3.21 when removing

Temperature	Filter 01	Filter 02	Data Set Size
77 K			86
293 K			49
77 K	$t_{min} > 50$ nm		33
293 K	$t_{min} > 50$ nm		37
77 K	$t_{min} > 50$ nm	$t_{diff} > 20$ nm	7
293 K	$t_{min} > 50$ nm	$t_{diff} > 20$ nm	17
77 K	$t_{min} > 50$ nm	Diagonal Break	29
293 K	$t_{min} > 50$ nm	Diagonal Break	33
77 K	$t_{min} > 50$ nm	Bond Break	4
293 K	$t_{min} > 50$ nm	Bond Break	5
77 K	$t_{min} > 50$ nm	Re-oxidised	16
293 K	$t_{min} > 50$ nm	Re-oxidised	14
77 K	$t_{min} > 50$ nm	Not Re-oxidised	17
293 K	$t_{min} > 50$ nm	Not Re-oxidised	24
77 K	$t_{min} > 50$ nm	Same Ingot	25
293 K	$t_{min} > 50$ nm	Same Ingot	20
77 K	$t_{min} > 50$ nm	Mixed Ingot	8
293 K	$t_{min} > 50$ nm	Mixed Ingot	18

Table 3.1: *Data set sizes used in Figure 3.21*

samples with a minimum oxide layer thickness of less than 50 nm: both the characteristic strength and Weibull modulus increase. This is not seen for the strengths measured at room temperature, possibly because only a very small portion of the room temperature samples had oxide layers below 50 nm. The complete sample set size having oxide thicknesses lower than 50 nm was too small to allow statistically significant results to be obtained at both room and low temperature, therefore measurements were predominantly made at cryogenic temperature for this group of samples.

At both temperatures, the samples broke in two different ways; in a ‘bond’ break, where the fracture was along the bond of the sample, or in a ‘diagonal’ break, where the fracture went through the bulk material. Both of these types of break are visible in Figure 3.22. A detailed image of the failed surfaces in both bond and diagonal break is shown in Figure 3.23. Although it would

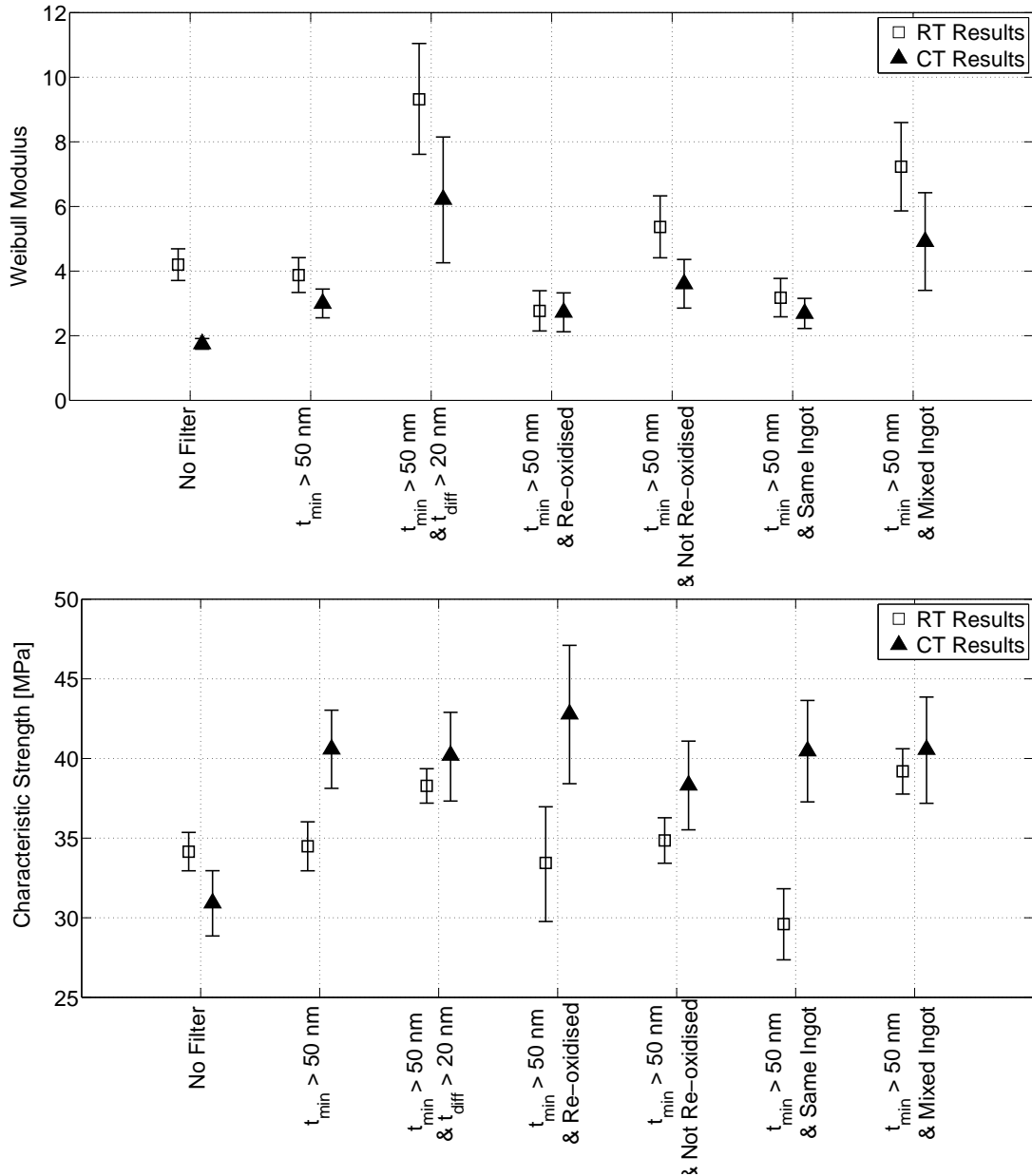


Figure 3.21: Graphs showing the values for the Weibull modulus (top) characteristic strength (bottom) for each data set, with error bars indicating the 68% confidence limits. The key describing the filters applied to each data set is shown in Table 3.1.

appear that different mechanisms caused the two samples to break, a similar strength was obtained. However, it was observed that the majority of the samples with a minimum oxide layer of less than 50 nm had a bond break in comparison to the samples with thicker oxide layers mostly having a diagonal

break pattern, suggesting that when the bonds were weak the sample would break along the bond. This supports the hypothesis that there is a minimum oxide layer needed for a bond to successfully form between the two surfaces.

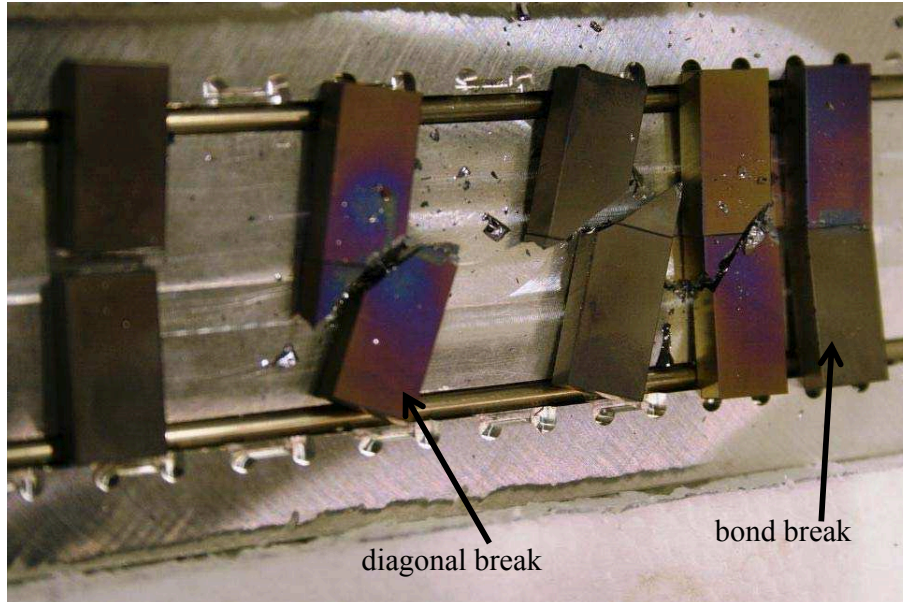


Figure 3.22: *Samples post- strength testing. The middle three samples broke through the bulk, whereas the samples at either end broke along the bond.*

Looking further at Figure 3.21 it was observed that when the difference between the oxide layers on the bonding surfaces of each sample was greater than 20 nm, although the characteristic strength (F_0) only increases at room temperature

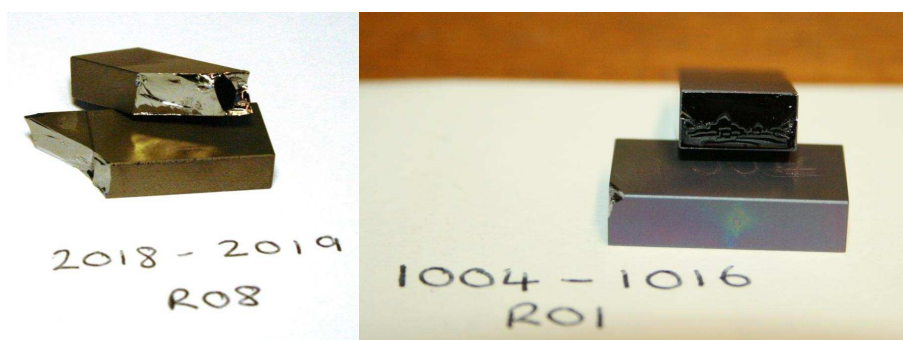


Figure 3.23: *Samples R08 (left) and R01 (right) were both tested at room temperature and although both failed in different ways, had strengths of 25.9 MPa and 26.5 MPa respectively, showing that the nature of the break is not solely indicative of a higher strength.*

(it remains the same at cryogenic temperature) the value of m increases by a significant amount at both temperatures, showing a reduction in the spread of strengths. The low grouping seen in Figure 3.18 is also eliminated. It is hypothesized that there may be a geometrical effect resulting from the large difference in oxide layer that is influencing these results.

The effect of re-oxidation does not consistently change the characteristic strength, however the value of m decreases when considering the samples that were re-oxidised, suggesting that the value of the characteristic strength is less reliable when the samples have been re-oxidised. This could be caused by, for example, an increased likelihood of contamination of samples before bonding or a weak interface between layers.

There is a marked difference between the room temperature results for characteristic strengths and Weibull modulus of samples from the same ingot in comparison to those from different ingots; both the strength and modulus increase when samples are from mixed ingots. At cryogenic temperature, the strength does not appear to change. However, the Weibull modulus does increase significantly for samples from mixed ingots. A possible explanation is a geometrical effect in samples from mixed ingots due to differences in the density of the oxide layer. A slowly grown thermal oxide layer will be denser than one grown rapidly [115]. Silicon of orientation $\langle 111 \rangle$ will grow a thermal oxide layer at a faster rate to silicon of orientation $\langle 100 \rangle$ and will therefore have a slightly less dense thermal oxide layer. However, the exact mechanism causing the improved value of m and the increase in characteristic strength at room temperature is not yet known.

3.6 Conclusion

Bend strength tests were performed on silicon samples jointed by hydroxide-catalysis bonding, where the silicon surfaces being jointed had thermal oxide layers of varying thicknesses. Strength test results show a characteristic strength of approximately 41 ± 2.4 MPa at 77 K and 35 ± 1.5 MPa at room temperature for samples with a minimum oxide layer of 50 nm. The bond strength reduced significantly with oxide layer thicknesses below 50 nm at cryogenic temperature.

Van Veggel et al. [111] showed bending strengths averaging 23 MPa in silicon carbide-silicon carbide bonds. Those experiments were performed with similar sample geometry and with a very similar 4-point bending set-up. The strengths for silicon-silicon bonds reported by van Veggel et al. [112] averaged 3.9 MPa at room temperature. Those strengths are a factor of 10 lower than those reported in this chapter. The experiments done by van Veggel et al. [112] were however performed under different loading conditions; i.e. they were shear experiments that were thought to be limited by the way the samples were clamped. Performing shear strength experiments that will be less dominated by the sample and loading geometry should shed light on the isotropy of the bond strength under different loading conditions. The results in this paper support the postulation by van Veggel et al. [112] that an oxide layer which is too thin can negatively influence the bond strength.

The bending stress in silicon-silicon bonds have previously been measured by Dari et al. [82] to be approximately 8.7 ± 3.7 MPa at room temperature. The results presented here use a different sample geometry and are significantly higher, also demonstrating the need for an oxide layer to be present for a successful bond to form.

In summary, it can be seen that the characteristic strength of all the samples

studied at both cryogenic and at room temperature lies above 20 MPa, and there exists an opportunity for this to increase along with the Weibull modulus once factors negatively affecting the bond can be identified and removed. It has been shown that repeated oxidation, differences in oxide thickness and ingot pairing can have effects on bond strength that would benefit from further investigation.

Chapter 4

Influence of the Oxide Layer on Bond Strength

4.1 Introduction

Previous investigations, described in Chapter 3, have shown hydroxide-catalysis bonds between silicon at both room and cryogenic temperatures have a characteristic strength of $\sim 36 \pm 3.9$ MPa [83]. The strengths obtained were higher than have been found for hydroxide-catalysis bonds between silica samples of the type currently used in the GEO600 gravitational wave detector and the upgrades to the LIGO detectors [56]. However, part of the sample preparation necessary to obtain reliable bonds between silicon samples involved thermal oxidation of the silicon surfaces. When considering the construction of the suspensions for the test masses for any future cryogenic gravitational wave detector, it may not be practical or desirable to thermally oxidise a complete silicon test mass for the purpose of bonding the suspension interface pieces onto the side of a mirror substrate. In current designs for the test masses for the ET-LF instrument, the mirror substrates are anticipated to be a minimum

of 211 kg with diameters of approximately 620×180 mm [79]. In order to apply a thermal oxide layer onto the bonding surface, the whole test mass would need to be placed inside a furnace, which would result in oxide layers being grown on all exposed surfaces, including the front mirror face, potentially damaging the mirror coatings or preventing their application.

In this chapter the results of investigations of the influence of different methods of applying a silicon dioxide layer to the bonding surfaces of silicon samples on the strength of bonds are presented. Also the influence of ingot purity and orientation are studied.

There are various possible ways in which a layer of silicon dioxide may be applied to the surfaces of silicon to be jointed. Here, three different techniques were selected; e-beam deposition, ion beam sputtering, and the growth of a dry thermal oxide. The strengths of bonds formed between samples whose surfaces were treated using these methods were then measured and the results compared to the bond strengths found in Chapter 3 in which wet thermal oxidation was used.

In this chapter, first the coating methods and resulting oxide layers are described; the bonding procedure and strength testing experiments are explained in detail in Chapter Three so only notable changes are discussed. The results are presented, and analysed using the same analysis method as in Chapter 3, and conclusions are drawn regarding the appropriateness of each type of oxide layer for use in future gravitational wave detectors.

4.2 Experimental Set Up

4.2.1 Sample Preparation

Three different methods were employed to deposit a silicon dioxide layer onto the bonding surfaces: thermal oxidation in a dry environment, ion-beam deposition and e-beam sputtering. The thermal oxidation was carried out at the University of Glasgow by the author; the ion-beam deposition and e-beam sputtering were carried out commercially by Gooch and Housego¹ and Advanced Thin Films² respectively. The thickness of the oxide layer requested from each vendor was 150 nm. The samples were ultra-sonically cleaned in acetone and methanol to remove any dust from the scribing of identification numbers to the sides of the samples prior to shipping to the respective companies.

For the strength tests described here, rectangular silicon blocks (of dimensions 20 mm × 10 mm × 5 mm) from two different silicon ingots were used. The first ingot was manufactured by Shin-Etsu³ and had a <100> crystallographic orientation. The second ingot had a <111> crystallographic orientation, and was manufactured by Prolog⁴. The Shin-Etsu ingot is float zone silicon doped with n-type Phosphorous with resistivities in the range 56.0 - 76.0 Ohm-cm. The ingot supplied by Prolog was grown using the Czochralski process, with an unknown resistance. The bonding surface in each case was a 5 mm × 10 mm surface, so that after bonding a sample was created with dimensions 40 mm × 10 mm × 5 mm, as shown in Figure 3.3.

25 samples of <111> orientation and 28 samples of <100> orientation had SiO₂ applied by ion beam sputtering. At the vendor the samples were cleaned in detergent and wiped with acetone prior to placing them into the coating

¹<http://goochandhousego.com>

²<http://www.atfilms.com>

³<http://shinetsu.co.jp>

⁴<http://www.semicor.ukrpack.net/>

chamber. They were then cleaned in O₂ plasma with an argon ion beam at 200-250 V beam energy. The ion beam sputtering was then performed using the argon ion beam and a GE124 fused quartz target. The temperature throughout the process remained below 90°C. However, the samples were heat treated at 450°C in air after coating to reduce any stresses in the coatings.

For the e-beam deposition, 27 <111> and 27<100 > samples were drag wiped with methanol and then inspected under a microscope before the coating procedure. The oxide layers were applied using electron beam evaporation using silica ground granules as the target. The temperature during the process was approximately 315°C, and the coating was not subsequently heat treated.

For the dry thermal oxidation, any organic residue was removed through an acid clean using a 1:7 volumetric ratio of hydrogen peroxide and sulphuric acid. 31 <111> samples and 33 <100> were placed in batches in air in a tube furnace at 1000°C for seven hours to grow an oxide layer of approximately 150 nm to match the ion beam and e-beam samples.

The thicknesses of the oxide layers formed from each of the processes were measured using ellipsometry. The e-beam samples were found to have oxide layer thicknesses of 134.61 ± 0.75 nm, the ion beam samples had oxide layer thicknesses of 154.06 ± 0.74 nm and the dry thermal oxide layers were 167.93 ± 13.19 nm thick.

The flatness of the bonding surface on each sample was also measured using the Zygo interferometer discussed in Section 3.4. The results are shown in Figure 4.1.

As in the experiments discussed in Chapter 3, the bonding surfaces were made hydrophilic prior to bonding through the same regime used in experiments described in Chapter 3 of polishing with cerium oxide in de-ionised water followed by cleaning with sodium bicarbonate and a methanol rinse. It was noticed that

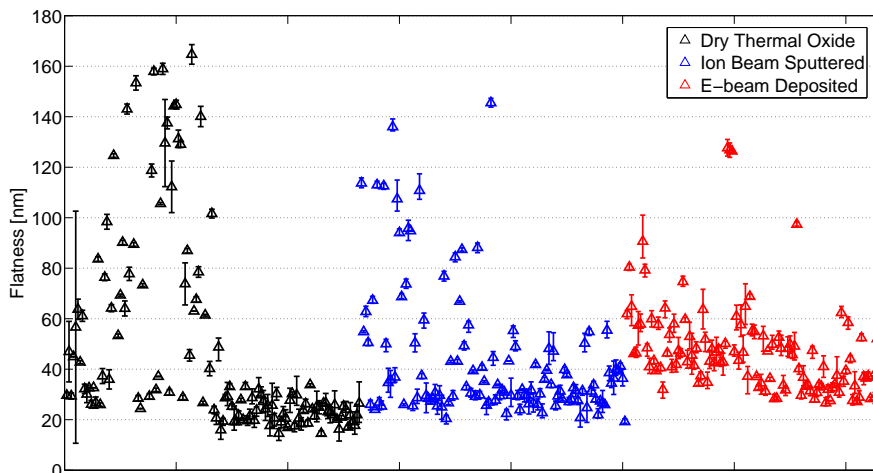


Figure 4.1: *The results of the flatness measurements for the silicon blocks after the oxide layers were applied.*

during this procedure, the ion-beam and e-beam coatings were vulnerable to such a coarse cleaning procedure and when a large force was applied during the cerium oxide step, the coating was partly worn away. This is shown in Figure 4.2 on the left hand side. Measurements with the ellipsometer discussed in Section 3.4 showed the oxide layer to have been reduced by approximately 20 nm in the centre of the bonding area and approximately 25 nm at the edges.

It was noticed that after the curing period of four weeks, a white residue was present of the corners of some of the samples. This is shown in Figure 4.2 on the right hand side. It is thought that this is due to excess bonding solution at the edge of the bond drying out. The samples that showed degradation of the oxide layer after the cleaning process, and that developed the white residue, were marked to determine if this influenced the bond strength.

The bonding solution was dispensed onto the surfaces to be jointed immediately after they had been treated with a final methanol wipe. $0.4 \mu\text{l}$ of solution per cm^2 was used ($0.2 \mu\text{l}$ for the strength test samples). The bonding solution was produced by diluting a commercially available sodium silicate solution (14% NaOH and 27% SiO_2) with de-ionized water at a volumetric ratio of

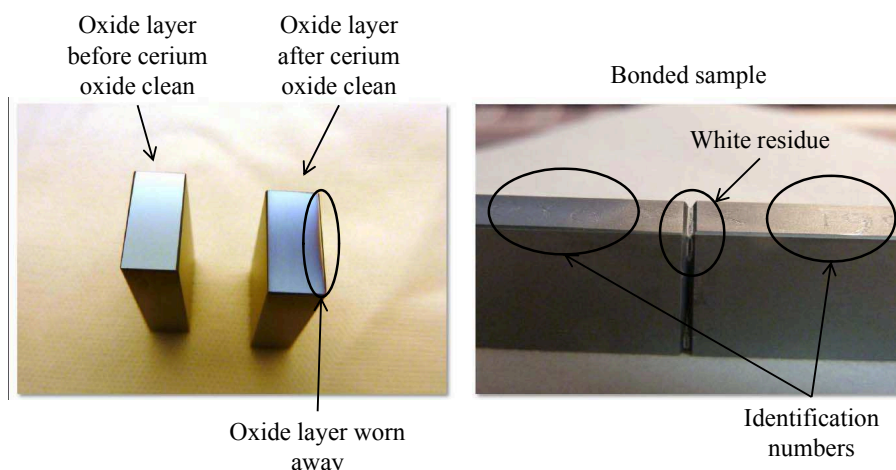


Figure 4.2: *Two observations were made during the bonding process; the ion-beam and e-beam coatings were occasionally worn away during the cerium oxide step (left) and a white residue was seen around the edges of some samples after the four week cure period (right).*

1:6, a solution used previously [108]. All samples were left to cure at room temperature for a minimum period of 4 weeks.

Samples were bonded like to like: i.e. a $\langle 111 \rangle$ sample with an e-beam coating was only bonded to another $\langle 111 \rangle$ e-beam sample.

4.2.2 Strength Testing Procedure

The bond strength was determined using the same set up as previously reported in Chapter 3, and shown in Figure 3.15 with the force, F , being applied through a loading arm and measured until the sample broke using a Zwick-Roell static 2kN machine. The supports below the sample were placed at a distance, L , apart and the force was applied equally through two line contacts on top of the sample at a distance l apart. Both distances were centered on the bond and the strength was obtained from the maximum force using equation 3.6.

Figure 3.16 shows the bath that was filled with liquid nitrogen in order to cool the set up and samples down to approximately 77 K. This enabled measure-

ments to be made at both room temperature and cryogenic temperatures using the same set-up.

166 samples were strength tested; 82 at room temperature and 84 at ~ 77 K. The samples were categorized by ingot orientation and oxidation technique. Table 4.1 shows the details for each data set used in the analysis of the results. These include the relevant results from Chapter 3, the allow for a comparison to the wet thermal oxides as well.

Temperature	Ingot	Oxide Layer Technique	Data Set Size
77 K	Prolog $\langle 111 \rangle$	Wet thermal oxide	09
293 K	Prolog $\langle 111 \rangle$	Wet thermal oxide	11
77 K	Prolog $\langle 111 \rangle$	Dry thermal oxide	16
293 K	Prolog $\langle 111 \rangle$	Dry thermal oxide	15
77 K	Prolog $\langle 111 \rangle$	Ion beam sputtered	13
293 K	Prolog $\langle 111 \rangle$	Ion beam sputtered	12
77 K	Prolog $\langle 111 \rangle$	E beam deposited	14
293 K	Prolog $\langle 111 \rangle$	E beam deposited	11
77 K	Prolog $\langle 100 \rangle$	Wet thermal oxide	14
293 K	Prolog $\langle 100 \rangle$	Wet thermal oxide	06
77 K	Shin-Etsu $\langle 100 \rangle$	Dry thermal oxide	17
293 K	Shin-Etsu $\langle 100 \rangle$	Dry thermal oxide	16
77 K	Shin-Etsu $\langle 100 \rangle$	Ion beam sputtered	14
293 K	Shin-Etsu $\langle 100 \rangle$	Ion beam sputtered	14
77 K	Shin-Etsu $\langle 100 \rangle$	E beam deposited	14
293 K	Shin-Etsu $\langle 100 \rangle$	E beam deposited	13

Table 4.1: *Data sets used in strength tests*

4.3 Results

Figure 4.3 shows the strength results that were obtained in total from samples treated by any of the three oxidation techniques. The results are presented in four graphs, displaying separately the two different ingots and two differ-

ent temperatures at which the strength was measured. The strengths of the bonds formed between samples for which (a) the ion-beam and e-beam coatings were worn away during the cleaning process and (b) the samples that had a white residue around the edges of the bond did not show deteriorating strength behaviour. Given this, they were included with the remainder of the results.

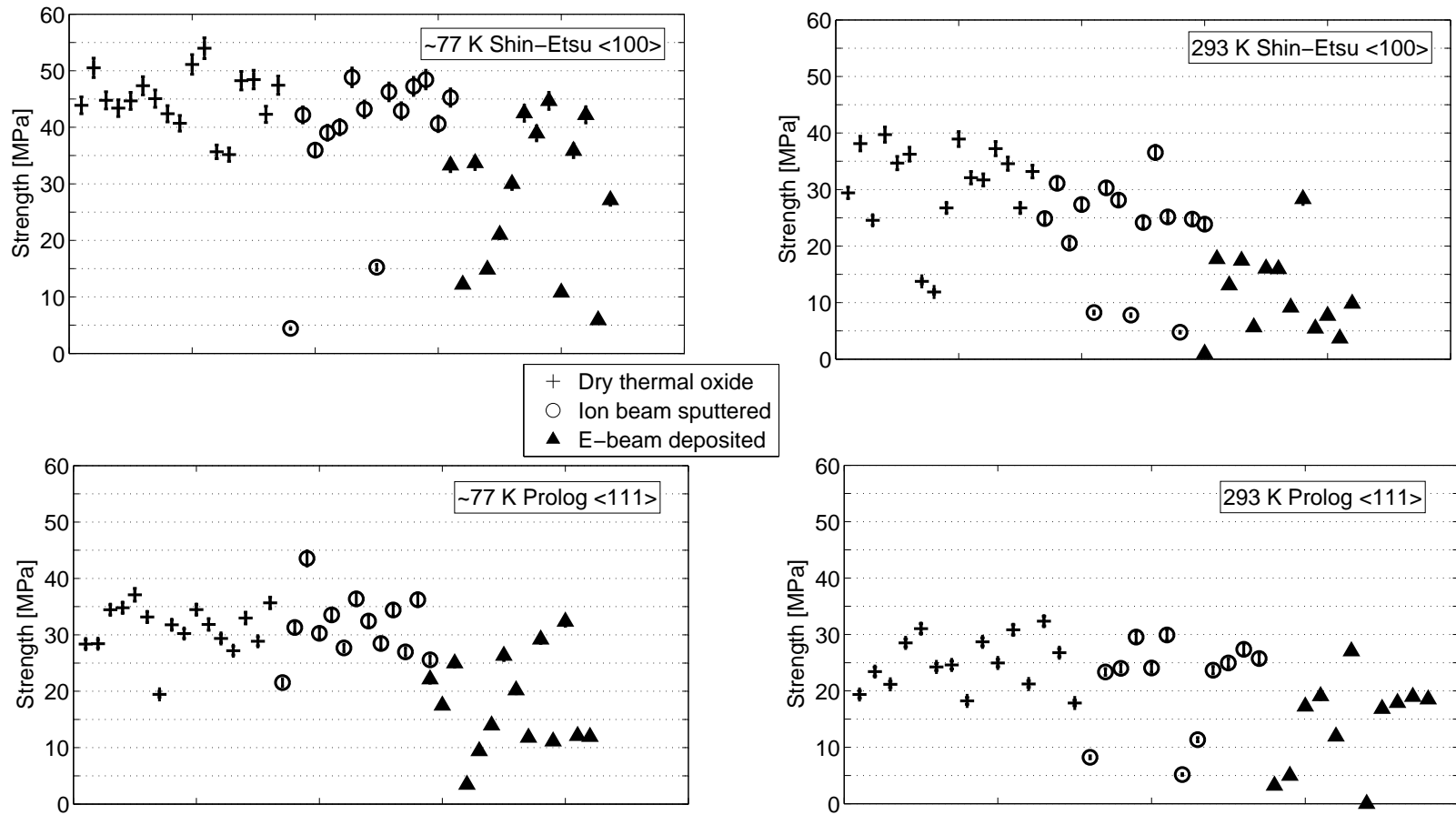


Figure 4.3: All strength test results, showing the results at both temperatures for the Shin-Etsu <100> samples (top) and Prolog <111> samples (bottom).

Figure 4.4 indicates that the average flatness of the bonding surfaces for each sample does not have a direct effect on the strength of the bond formed between them. Thus, it is postulated that the lower level of flatness seen in the dry thermal oxide samples in Figure 4.1 did not influence the strength of the bonded samples.

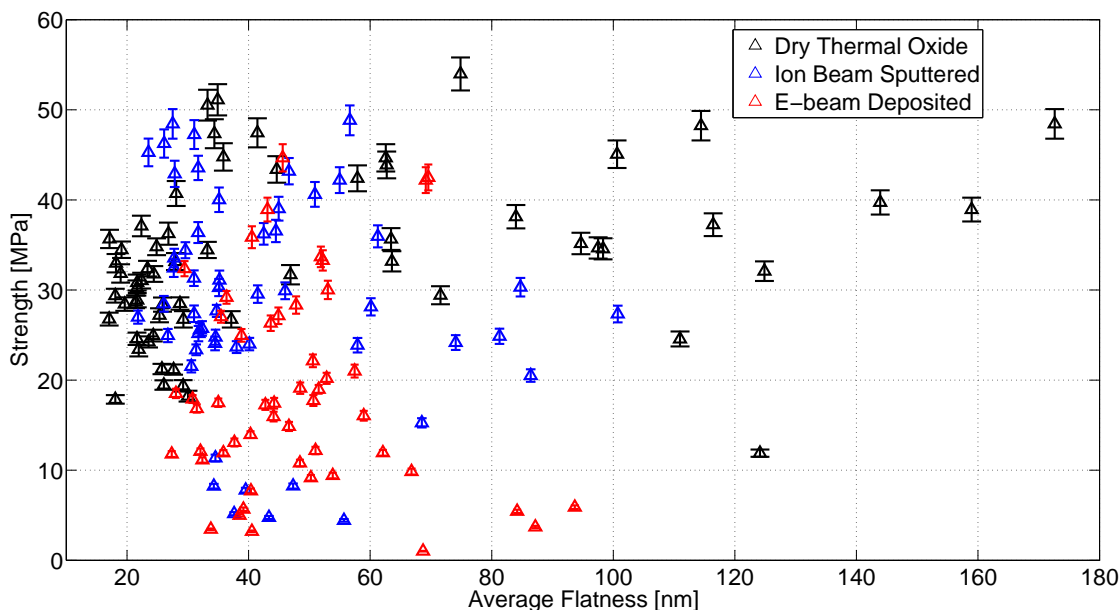


Figure 4.4: A plot showing the relationship between the average flatness of each pair bonding surfaces and strength of the bond formed between them.

4.3.1 Analysis and Comparison to Wet Thermal Oxide Results

A Weibull analysis of the results was performed. Due to the brittleness of the samples, fracture is likely to originate at flaws in the material itself. Therefore, the strength of the samples will depend upon the probability of there being a flaw that is large enough to cause a fracture normal to the direction of the maximum tensile stress. The statistical variation of such results can be expected to be modeled by a Weibull distribution [117].

The same Bayesian analysis used in Chapter 3 and published in [83] was carried out, estimating m and F_0 directly from the Weibull probability density function, and a Markov Chain Monte Carlo method [119] was used to obtain confidence regions for our fitted Weibull parameters.

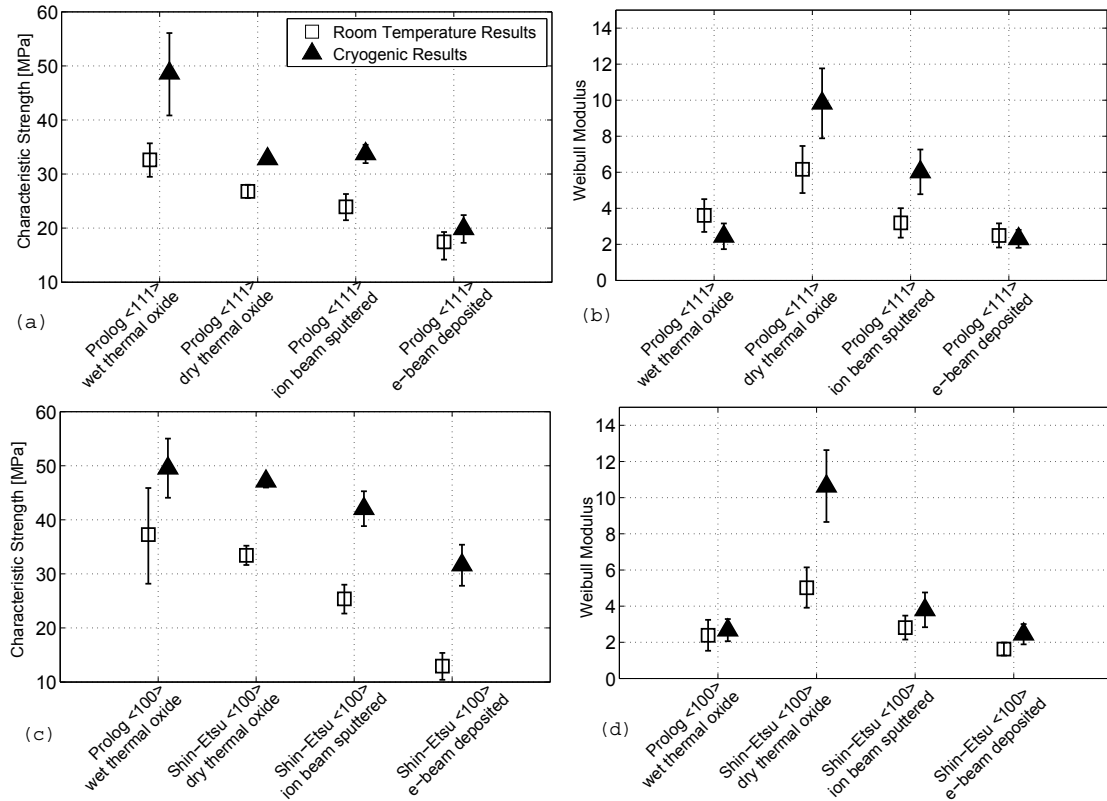


Figure 4.5: *Results of Weibull analysis. On the left characteristic strength is shown, and on the right the Weibull modulus is shown. The top row shows the $\langle 111 \rangle$ results, the bottom row the $\langle 100 \rangle$ results.*

Figure 4.5 shows the results of the Weibull analysis. It also includes the results from the wet thermal oxidised samples discussed in Chapter 3 for comparison. In order for the comparison to be valid, only samples that had a minimum oxide layer thickness greater than 50 nm and a difference in oxide layer thickness of less than 20 nm were included. These results do include samples that were re-oxidised, which was shown to negatively influence the Weibull modulus but did not affect the characteristic strength. These samples were not removed as this would have resulted in insufficient data for a comparison.

From inspection of Figure 4.3, bonds between the samples coated using the e-beam method consistently show the lowest strengths. This is confirmed by the lower characteristic strength and also low Weibull modulus shown in Figure 4.5. Focussing on the top two graphs in Figure 4.5, two features are identified. Firstly, although the ion beam sputtered and dry thermal oxide results exhibit similar strengths, the dry thermal oxide produced a more consistent range of strengths, as demonstrated by the higher value for m . Secondly, at cryogenic temperature, the wet thermal oxide appears to contribute to a stronger bond. The low value for m for the wet thermal oxide is likely due to the inclusion of the re-oxidised samples from the previous experiment. Thirdly, cryogenic strengths are consistently higher than room temperature strengths.

The bottom two graphs in Figure 4.5 show the results from the $\langle 100 \rangle$ crystallographic orientation. Here, it should be noted that the wet thermal oxide results are from a lower purity silicon ingot produced also with a different method (Prolog, CZ P-type boron doped) than all other samples (Shin Etsu, FZ N-type). We see a general downwards trend when moving from the thermal oxide results, to the ion beam sputtered results, to the e-beam deposited results and there is little difference in characteristic strength between the two thermal oxides.

Though room temperature results show on the whole a downward trend in strength when moving from wet thermal oxide to dry thermal oxide to ion beam sputtering to e-beam deposition, the values of characteristic strengths when comparing $\langle 111 \rangle$ to $\langle 100 \rangle$ results are mostly quite similar. The cryogenic characteristic strengths of the Shin-Etsu $\langle 100 \rangle$ are notably higher (> 10 MPa difference) than the cryogenic Prolog $\langle 111 \rangle$ results.

The samples broke in two different ways, ‘bond’ breaks, where a majority of the bonding surface is exposed after strength testing, and ‘diagonal’ breaks where the bulk silicon failed. Images of the two types of break can be seen in Figure

4.6. Table 4.2 shows the proportion of bond breaks for each ingot and oxide layer type. It has previously been suggested that samples that break along the bond generally have a lower strength [112] than those that failed in the bulk of the bonded silicon and this pattern is seen again here. The e-beam samples that consistently showed lower strengths have the highest proportion of bond breaks. In every case, the Prolog $\langle 111 \rangle$ samples had a higher proportion of bond breaks, and at room temperature, samples were more likely to break along the bond.



Figure 4.6: *Bond break (top) and diagonal break (bottom).*

		Percentage of bond breaks at 293 K	Percentage of bond breaks at 77 K
Dry Oxide	Shin-Etsu 100	24%	19%
	Prolog 111	88%	33%
Ion Beam	Shin-Etsu 100	36%	36%
	Prolog 111	77%	92%
E-Beam	Shin-Etsu 100	57%	54%
	Prolog 111	93%	72%

Table 4.2: *Percentage of bond breaks*

Interestingly, as shown in Figure 4.7, the bond break surfaces for the e-beam samples are distinctly different to those of the ion beam and dry thermal oxide samples. The surface was uniform in colour on both parts of the sample, and

measurements taken using ellipsometry show the majority of the original oxide layer to still be unchanged in thickness on both surfaces, suggesting that the bond failed, leaving the oxide layers in tact. The ion beam and dry thermal oxide samples produced mirrored patterns, where sections of the exposed surfaces could be measured, showing the original oxide layer remained. However, the majority of the surfaces showed evidence of multiple layers, indicating that when the bond failed, parts of the oxide layers also broke away from the original surfaces.

These results suggest that the reason for the lower strengths found in the e-beam sputtered samples was the formation of a less strong bond than in the ion beam and dry oxide samples and that it was not a problem in the adhesion of the coating to the silicon surface.

Communications with the vendor suggests that e-beam coatings have voids, thus it was decided to test if these voids could actually be identified, and if hydrogen gas was being formed, by submerging unbonded but coated samples in bonding solution for several hours. Using a Wyko NT1100 optical profiling system⁵ it was found that only e-beam sputtered <100> samples showed voids, typically 20 nm deep with a density of ~ 60 voids/mm². These could not be seen in any of the other samples. The submergence tests did not reveal any obvious hydrogen gas formation in any of the samples. We therefore believe hydrogen formation was not the cause of the lower strength bonds.

Another possible reason for the strength could be a difference in the density of coatings. Discussions with the vendors suggests e-beam deposition should give the lowest density coatings, followed by ion beam sputtering and thermal oxides should be the most dense.

Attempts were made to measure the density of the oxide layers by measuring the weight of a coated sample before and after the coating was etched away.

⁵<http://www.veeco.com>

Exact densities could not be obtained due to the weight change being too small to accurately measure. However, the relative values were consistent with the e-beam method producing the least dense oxide layer, and the thermal oxide the most dense. The density of the oxide layer may contribute to the overall strength of the bond as the lower the density, the lower the number of siloxane chains that may be formed; further research is required to confirm this.

4.4 Discussion and Summary

Bend strength tests were performed on hydroxide-catalysis bonds formed between silicon samples of different crystallographic orientation that had been oxidised using a range of methods. The three methods used were; dry thermal oxidation, ion beam sputtering and e-beam deposition. These results were compared with the previous results from samples with surfaces treated using wet thermal oxidation. It was found that the coating method used did influence the strength of the resulting bond. The e-beam deposited layers produced the weakest samples, with strengths of 17 ± 2 MPa and 20 ± 4 MPa for the Prolog $\langle 111 \rangle$ samples and 13 ± 3 MPa and 32 ± 4 MPa for the Shin-Etsu $\langle 100 \rangle$ samples at room temperature and cryogenic temperature, respectively. The dry thermal oxide produced the results with the smallest spread of values, with strengths of 27 ± 1 MPa and 33 ± 1 MPa for the Prolog $\langle 111 \rangle$ samples and 33 ± 2 MPa and 47 ± 1 MPa for the Shin-Etsu $\langle 100 \rangle$ samples at room temperature and cryogenic temperature, respectively. The ion beam sputtered layer produced strengths of 24 ± 3 MPa and 34 ± 2 MPa for the Prolog $\langle 111 \rangle$ samples and 25 ± 3 MPa and 42 ± 3 MPa for the Shin-Etsu $\langle 100 \rangle$ samples at room temperature and cryogenic temperature, respectively. These were compared to the wet thermal oxide results from Chapter 3 of 35 ± 2 MPa and 41 ± 2 MPa at room temperature and cryogenic temperature, respectively.

These results are consistent with previous experiments, where a minimum thickness of wet thermal oxide layer of 50 nm was established for reliable bonds at cryogenic temperature [83] and with van Veggel et al. [111] who showed bending strengths averaging 23 MPa in silicon carbide-silicon carbide bonds.

It was observed that Shin-Etsu <100> ingot produced stronger bonds at cryogenic temperature, and that the dry thermal oxide layer produced the most reliable results for both ingots. The reason for the large difference between the room temperature and cryogenic temperature results for the Shin-Etsu <100> is not yet understood.

It is postulated that the reason for the lower strength of the e-beam samples is that the density is lower. Based on the photographs of samples broken on the bond, the e-beam coating has adhered well to the silicon surface. This must mean that the hydroxide-catalysis bond has not been adhered as well to the oxides as was the case for the thermally oxidised and ion-beam sputtered sample. It could be that fewer siloxane chains can be formed due to the reduced density.

The results presented here show that the methods of ion beam sputtering, and thermal oxidation may be considered to apply a layer of SiO₂ onto the bonding surfaces of a silicon test mass and suspension components. The three methods produced strength of over 25 MPa, showing that hydroxide-catalysis bonding is a valid technique for the construction of silicon suspensions in cryogenic gravitational wave detectors.

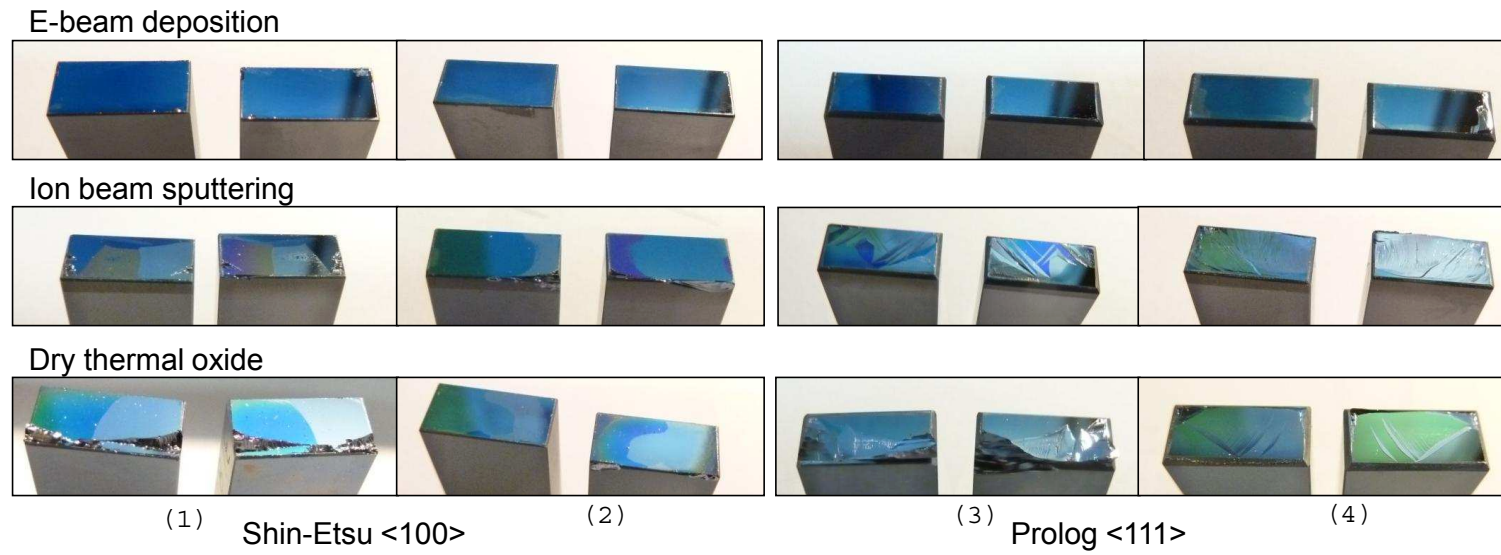


Figure 4.7: *Example bond break surfaces at room temperature: e-beam (top), ion beam (middle) and dry thermal oxide (bottom). Columns 1 and 2 show Shin-Etsu $\langle 100 \rangle$ samples, and columns 3 and 4 show Prolog $\langle 111 \rangle$ samples.*

Chapter 5

Mechanical Loss of Hydroxide-Catalysis Bonds

5.1 Introduction

As discussed in Chapter 2, part of the thermal noise in gravitational wave detectors results from the internal friction in the hydroxide-catalysis bonds of the suspension interface pieces to the test masses. It is therefore important to quantify the mechanical loss of hydroxide-catalysis bonds between relevant materials.

The mechanical loss of a hydroxide-catalysis bond has previously been investigated and found to be between 0.18 and 0.54 for a bond between bulk silica samples at room temperature [104]. In order for hydroxide-catalysis bonds to be considered for use in the suspensions of cryogenic gravitational wave detectors, the mechanical loss of the bond must be characterised at low temperature, where the detector is likely to operate, and for silicon-silicon bonds in order to estimate the level of thermal noise introduced by the bonds.

The mechanical loss of mirror coatings on cantilevers have been measured at

cryogenic temperature using a well established method [121]. In this method silicon cantilevers are clamped and excited to an amplitude A , and then the excitation signal is removed and the resonance allowed to de-excite. The experimental set-up is discussed in more detail in Section 5.2.1.

At a resonant mode of a system, the mechanical loss can be calculated using equation 5.1, where E_{stored} is the total energy stored in the oscillating system, and $E_{dissipated}$ is the energy dissipated with each cycle of oscillation.

$$\phi(\omega_0) = \frac{E_{dissipated}}{2\pi E_{stored}} \quad (5.1)$$

It is possible to measure mechanical loss through measuring the ring down time of a resonant mode of angular frequency ω_0 from an initial amplitude A_0 . The time dependence of the amplitude decay $A(t)$ is given by:

$$A(t) = A_0 e^{-\phi(\omega_0)\omega_0 t/2}. \quad (5.2)$$

For a cantilever of thickness a , length L , Young's modulus Y and density ρ , the first five resonant frequencies can be calculated using equation 5.3 [122] where $k_n L = 1.875$ (n=1), 4.694 (n=2), 7.853 (n=3), 10.996 (n=4) and 14.137 (n=5) [123].

$$\omega_n = (k_n L)^2 \frac{a}{2\sqrt{3}L^2} \left(\frac{Y}{\rho}\right)^{(1/2)} \quad (5.3)$$

The above method can be adapted to determine the mechanical loss of a hydroxide-catalysis bond in a pair of bonded silicon cantilevers. Preliminary results [124] have suggested that the loss of the bond between 20 and 200 K had an upper limit of 0.2. The bonded cantilevers in this case had a bond of irregular quality with voids visible throughout the bond. By measuring a

higher quality bond, it is hoped that a more precise upper limit to the loss can be established.

The benefit of using a silicon cantilever is the low dissipation of silicon at cryogenic temperatures [49; 77; 125; 126]. However, in order to successfully bond the cantilevers together, a layer of SiO_2 (silica) is required on the bonding surfaces [106]. Silica, although it has low dissipation at room temperature [125; 127; 128], is known to have a dissipation peak at $\sim 30 - 50$ K [49]. It is possible to take the loss of the oxide layers and substrate into account, and from the measured loss of the bonded cantilever structure, extract the mechanical loss of the bond layer.

5.2 Experimental Procedure

5.2.1 Experimental Set-Up

The experimental set-up for the measurement of mechanical loss of a cantilever is shown in Figure 5.3. A cantilever (of approximate dimensions $45 \times 5 \times 0.07$ mm) was clamped inside a cryostat, which was evacuated to a pressure of approximately 1×10^{-6} mbar to minimise any dissipative effects from gas damping [129] and cooled to an initial temperature of 10 K. The temperature of the clamp was monitored using DT-670 silicon diode sensors.

The bending modes of the cantilever are excited electrostatically by applying an oscillating high voltage signal at the frequency of each mode using the exciter plate, shown in Figure 5.3. The motion of the excited cantilever can be monitored by illuminating the clamped cantilever with a laser beam. The amplitude of the excited mode and subsequent ring down is recorded by measuring the shadow of the cantilever as it bends that is cast onto a split photodiode

sensor. An example of an excitation signal and the resultant ringdown is shown in Figures 5.1 and 5.2.

The measured dissipation is calculated using Matlab software¹ from an exponential fit to the amplitude ring down using equation 5.2.

The loss value obtained using this method is that of the total of all the energy dissipation mechanisms present in the sample. If the sample has an oxide layer, or contains a hydroxide-catalysis bond; further analysis must be done to extract the loss associated with these features, as will be described.

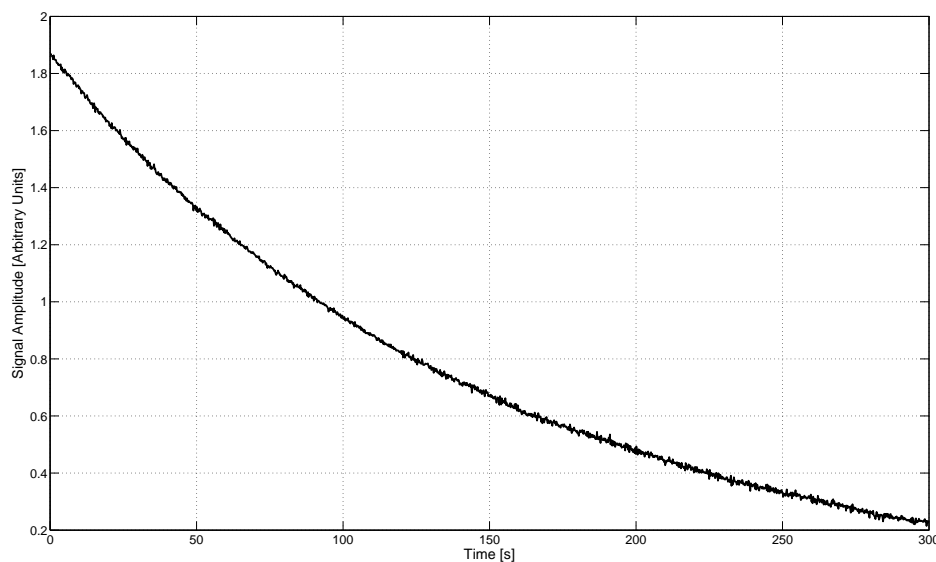


Figure 5.1: *An example of the raw data obtained from the experimental set up. A ringdown of the second resonant mode at 40 K is shown.*

Loss measurements were made at 2 K temperature steps from 10 to 50 K, every 5 K up to 100 K and every 20 K up to 240 K. At each temperature step, the clamp and sample were held at the specified temperature using a Lakeshore 340 temperature proportional integral derivative (PID) controller which used the difference between the measured temperature and the set temperature to adjust the heat supplied to the clamp from high wattage resistors, shown in

¹<http://www.mathworks.co.uk>

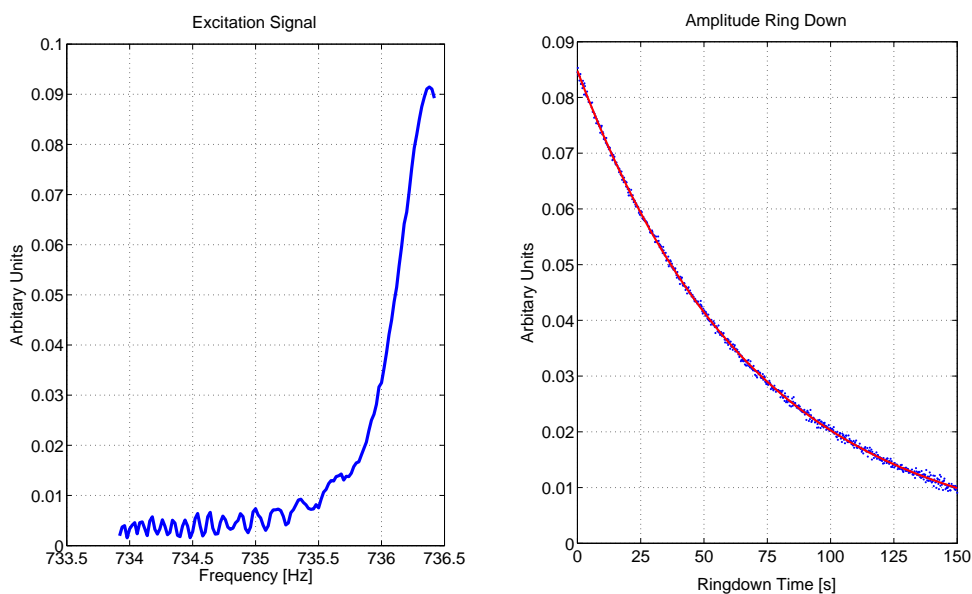


Figure 5.2: *Example of the excitation signal (left) for a silicon cantilever and the subsequent ringdown (right) of the amplitude of motion of the cantilever at a resonant frequency.*

Figure 5.4. Three ‘ringdowns’ at each measurable resonant frequency were made before the clamp was heated up to the next temperature step.

After completing ringdowns at each temperature step, the cantilever was re-clamped inside the cryostat and the process was repeated until three sets of data were obtained. This allows assessment of any contribution to the mechanical loss from friction due to movement of the clamped end of the sample in the clamping block so it can be minimised [130].

5.2.2 Measurement and Analysis Method

5.2.2.1 Introduction

The technique of calculating the mechanical loss of a coating applied on a substrate is well established [121], and can be adapted to extract the loss contribution of a silicate bond layer from the measured loss of a pair of bonded

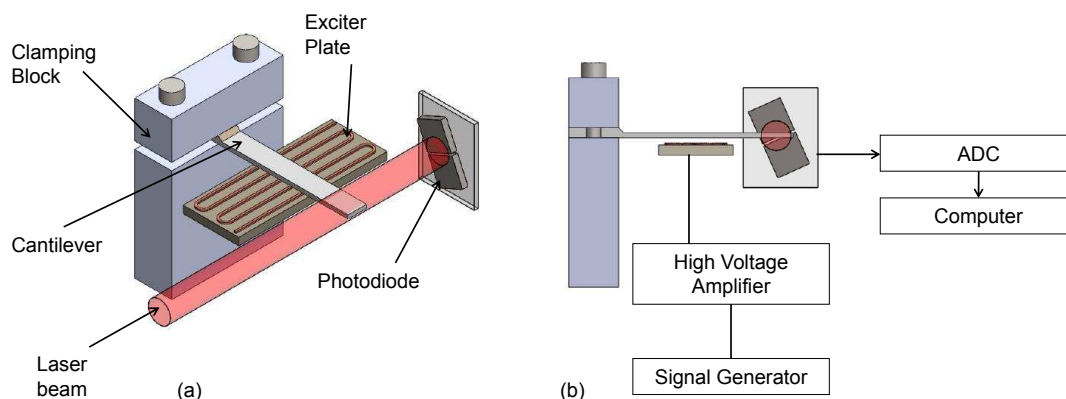


Figure 5.3: *The experimental set up for the measurement of the mechanical loss of a silicon cantilever.*

oxidised silicon cantilevers.

The loss of the unoxidised cantilevers is measured and then loss measurements are carried out again after oxidation such that the loss of the oxide layers may be extracted. Measurements are repeated typically three times, over a temperature range of 10 K to 250 K. The cantilevers are then bonded and after a four week curing period, are measured again so that the bond loss can be extracted. The process used to prepare the cantilevers for each step is described in Section 5.2.3, and the analysis used to determine the losses of the oxide layer and bond material is described below.

As the bonded sample vibrates, energy will be dissipated by internal friction in the bond, the oxide layers and in the silicon. However, only the energy stored in the bond can be dissipated in the bond thus it is necessary to calculate the fraction of the total elastic energy stored in each region of the sample.

The product of the total mechanical loss of the bonded structure and the total strain energy stored in the system is equal to the sum of the products of the mechanical losses and stored strain energies for each mechanical loss

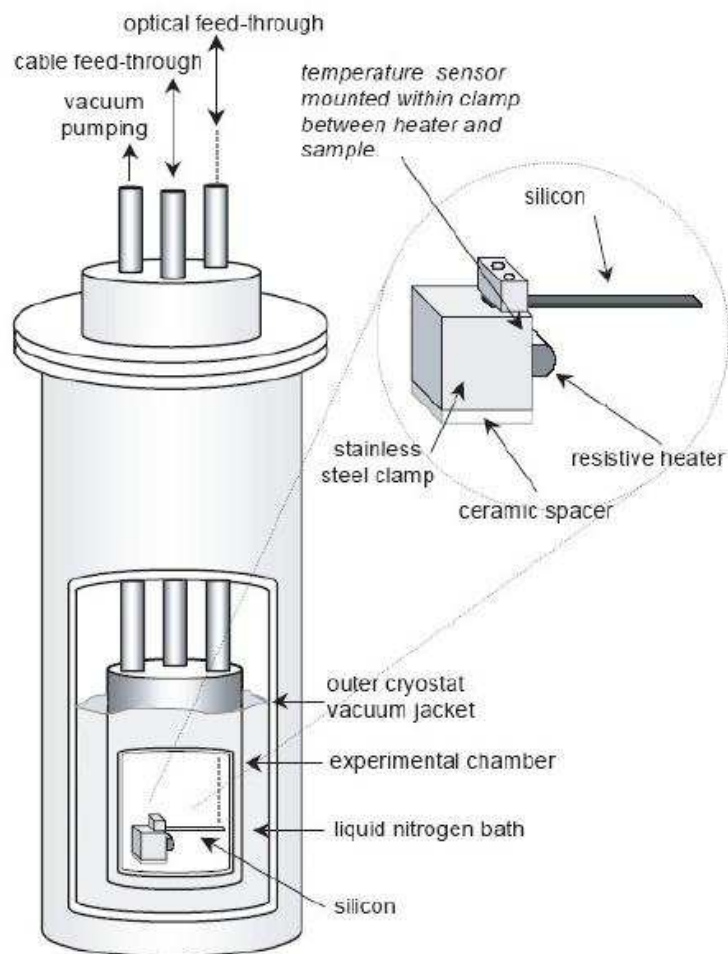


Figure 5.4: Schematic diagram of the cryostat, with an inset showing details of the clamp used to hold the cantilever samples.

component. This may be written as [131]:

$$E_t \phi_t = E_s(\phi_s + \phi_{sTE}) + E_b \phi_b + E_o \phi_o, \quad (5.4)$$

where E is the strain energy, ϕ is the loss and the subscripts s , b and o represent the substrate, bond layer and oxide layers respectively. ϕ_{sTE} is the thermoelastic loss contribution, as described in Section 5.2.2.2, and the subscript t denotes the total strain energy and loss of the structure.

The bond has a much smaller volume than the remainder structure, thus it can be assumed that the silicon substrates store the majority of the elastic strain energy of the structure, such that $E_s \approx E_t$. Equation 5.4 therefore becomes:

$$\phi_t = \phi_s + \phi_{sTE} + \frac{E_b}{E_t} \phi_b + \frac{E_o}{E_t} \phi_o, \quad (5.5)$$

where the energy ratios E_b/E_t and E_o/E_t are the scaling factor by which the intrinsic component losses are multiplied. Both ϕ_s and ϕ_{sTE} can be determined, ϕ_s through the measurement of unoxidised silicon cantilevers and ϕ_{sTE} can be calculated from the known dimensions and material properties of the cantilevers.

From measuring a silicon cantilever before and after oxidation, the loss of the oxide layer (ϕ_o) on the silicon substrate can be calculated using equation 5.6 [121]. Here, the subscript m denotes the measured loss of the oxidised cantilever. The thickness of the oxide layer (t) is taken to be the combined thickness of both the top and bottom oxide layers of the cantilever, a is the thickness of the silicon substrate, and Y represents the Young's modulus.

$$\phi_o(\omega_0) = \frac{Y_s a}{3Y_o t} (\phi_m(\omega_0) - \phi_s(\omega_0)) \quad (5.6)$$

5.2.2.2 Thermoelastic Damping

When a thin beam or fibre is deflected into an arc, the part of the beam under compression will heat up, while the opposite side of the beam will expand and cool down. This temperature difference causes a heat flow across the beam, and a vibrating beam will have an oscillating heat flow as each side of the beam is compressed and stretched in turn. This heat flow is the source of thermoelastic dissipation and will peak at a frequency related to the time taken for heat to flow across the beam. This is demonstrated in Figure 5.5.

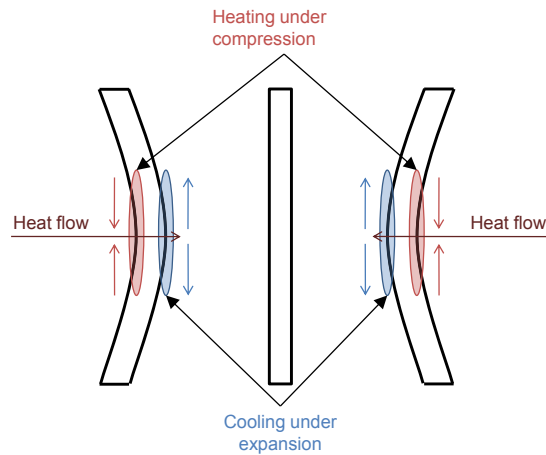


Figure 5.5: A schematic diagram of a bending beam. As the beam oscillates, the sections undergoing compression and tension will experience heating and cooling effects that alternate with each cycle of oscillation.

The level of thermoelastic dissipation, ϕ_{TE} , as calculated by Zener [132; 133] in a flexure is shown in equation 5.7 where Y represents the Young's modulus, ρ is the density, C is the specific heat capacity and τ is the relaxation time.

$$\phi_{TE}(\omega) = \frac{Y\alpha^2 T}{\rho C} \frac{\omega\tau}{1 + \omega^2\tau^2} \quad (5.7)$$

The relaxation time, which is the time taken for heat to flow across the beam, sets a characteristic frequency, $f_{char} = (2\pi\tau)^{-1}$, at which the maximum thermoelastic loss occurs. The relaxation time for a fibre with a rectangular cross section of thickness t is given by equation 5.8, and for a circular cross section with diameter d is given by equation 5.9 [134].

$$\tau = \frac{\rho C t^2}{\pi^2 \kappa} \quad (5.8)$$

$$\tau = \frac{\rho C d^2}{13.55 \kappa} \quad (5.9)$$

This theory can be directly applied in the estimation of the thermoelastic

thermal noise for the suspensions of gravitational wave detectors.

5.2.2.3 The Elastic Strain Energy stored in the Oxide Layers and Bond Layer

If the two component cantilevers to be bonded have thicknesses of a and b , the bond layer can be thought of as starting a distance a below the surface of a thin rectangular beam with a total thickness $(a + b)$, as shown in Figure 5.6.

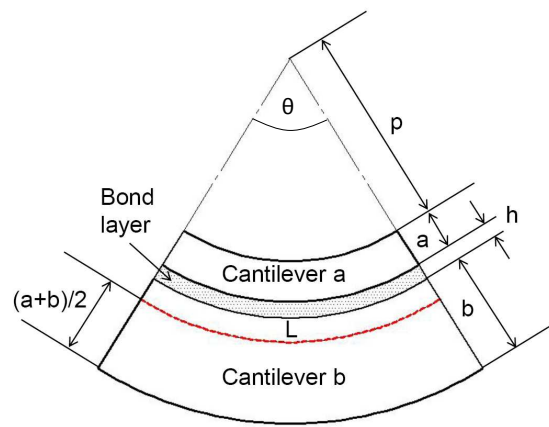


Figure 5.6: A schematic for the bending bonded structure, not to scale.

The energy ratio is calculated analytically using the geometry of the structure, and the expression for the stored energy in the bond layer can be based upon geometric corrections to the known expression for the elastic strain energy in a coating applied to one surface of a cantilever [135]:

$$E_o = \frac{Y t w}{2 L} \Delta L^2, \quad (5.10)$$

where Y is the Young's modulus of the cantilever with thickness t and width w , and ΔL is the change in length due to the applied strain.

$$\frac{E_c}{E_t} = \frac{3 Y_c t_c}{Y_s t_s} \quad (5.11)$$

The force exerted on the volume by the excitation can be calculated using equation 5.12, and the integral of the force, with respect to the resultant extension, (ΔL), is equal to the stored elastic energy in the volume [135]. Equation 5.12 can be applied to the bond layer in the pair of bonded cantilevers and using the small angle approximation, the length of the unstressed bond, L , is equal to θp .

$$F = \frac{Y w t}{L} \Delta L \quad (5.12)$$

In the case of the pair of bonded cantilevers, where both cantilevers are made of the same material, the neutral axis occurs halfway through the sample such that $L = \theta (p + \frac{1}{2}(a + b))$. Given that the thickness of the bond, $h \ll a, b$, ΔL does not change by a significant amount between the top and bottom surfaces and equation 5.10 for the total energy stored in the bond layer can be written:

$$E_b = \frac{Y_b h w}{2 L} \theta^2 \left(\frac{b - a}{2} \right)^2. \quad (5.13)$$

The two external oxide layers of the bonded structure, which can be considered to have thicknesses of t_1 and t_4 , can be treated as coatings on a substrate. The energy ratios can therefore be written as shown in equations 5.14 and 5.15.

$$\frac{E_{o1}}{E_t} = \frac{3 Y_o t_1}{Y_s t_s} \quad (5.14)$$

$$\frac{E_{o4}}{E_t} = \frac{3 Y_o t_4}{Y_s t_s} \quad (5.15)$$

The oxide layers on the bonding surfaces of the cantilevers (i.e. they are internal to the bonded structure) with thicknesses t_2 and t_3 should also be considered. Assuming the oxide layer is not completely consumed during the bonding process, they can both be treated in the same way as the bond layer, and the

strain energy for each can be calculated as shown in equations 5.16 and 5.17:

$$E_{o2} = \frac{Y_o t_2 w}{2L} \theta^2 \left(\frac{b-a}{2} \right)^2 \quad (5.16)$$

$$E_{o3} = \frac{Y_o t_3 w}{2L} \theta^2 \left(\frac{b-a}{2} \right)^2, \quad (5.17)$$

where $\theta^2 \left(\frac{b-a}{2} \right)$ represents the change in length experienced by the oxide layer. This can be considered to be the same for both oxide layers and the bond, due to the relative thicknesses of the oxide layers and bond layer to the cantilever thickness as the difference in the change in length between each layer varies by an insignificant amount.

Assuming the presence of the oxide and bond layers does not alter the overall elastic behaviour, the bonded structure can be considered as a single cantilever of thickness $T = (a+b)$. Heptonstall [135] shows the energy stored in a bending cantilever is given by:

$$\frac{E_t}{2} = \frac{1}{48} \frac{Y_s w \theta^2 T^3}{L}, \quad (5.18)$$

and therefore:

$$E_t = \frac{1}{24} \frac{Y_s w \theta^2 (a+b)^3}{L}, \quad (5.19)$$

and the energy ratio E_b/E_t :

$$\frac{E_b}{E_t} = \frac{3Y_b h(a-b)^2}{Y_t (a+b)^3}. \quad (5.20)$$

Assuming the majority of the measured loss (ϕ_m) in the bonded structure arises from the thermoelastic loss in the substrate, the loss of the bond layer and the loss of the oxide layers, an upper limit to the bond loss can be calculated. Equation 5.21 shows the sum of the products of the mechanical loss and energy for such a case, where each of the four oxide layers are denominated by the

subscript 1 - 4:

$$E_t \phi_m = E_s \phi_s + E_b \phi_b + E_{s_{TE}} \phi_{s_{TE}} + E_{o1} \phi_{o1} + E_{o2} \phi_{o2} + E_{o3} \phi_{o3} + E_{o4} \phi_{o4}. \quad (5.21)$$

Since each oxide layer will have the same loss value, ϕ_{1-4} can be replaced by ϕ_o . It can also be noted that $E_{o1}/E_t = E_{o4}/E_t$. Dividing through by E_t and re-arranging equation 5.21 provides us with an equation for determining the loss contributed by the bond layer:

$$\phi_b = \frac{E_t}{E_b} \left[\phi_m - \phi_s - \phi_{s_{TE}} - 2 \frac{E_{o1}}{E_t} \phi_o - \frac{E_{o2}}{E_t} \phi_o - \frac{E_{o3}}{E_t} \phi_o \right]. \quad (5.22)$$

5.2.3 Sample Preparation

In order to fabricate a sample that could be used to measure the mechanical loss of a hydroxide-catalysis bond, two silicon cantilevers were manufactured by Kelvin Nanotechnology with thicknesses measured to be 66 μm and 26 μm respectively (see Figure 5.7). The surface of both cantilevers lies on the (100) plane. The thicknesses of the cantilevers were calculated using equation 5.3, after measuring the fundamental frequencies once the cantilevers were clamped inside the cryostat. The Young's Modulus of silicon was taken to be 164 GPa [136], and the density was taken to be 2330 kg/m³ [137].

By bonding cantilevers of unequal thicknesses, the hydroxide-catalysis bond can be offset from the neutral axis, allowing the mechanical loss of the bond to be measured.

The cantilevers were oxidised and bonded (see Figure 5.7) - these steps are described in the following sections - and the loss then measured using the setup shown in Figure 5.3.

The cantilevers were oxidised in the same way as that described in Chapter

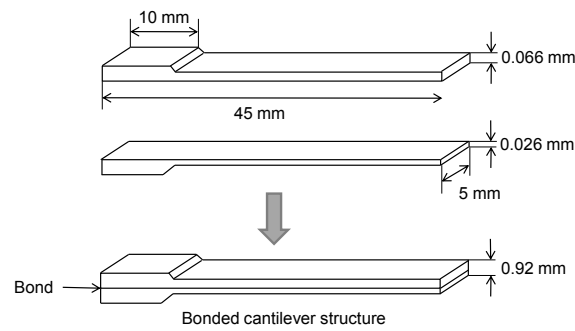


Figure 5.7: *CAD schematic of (a) the individual cantilevers to be bonded and (b) the bonded cantilever structure.*

3; after cleaning the cantilevers in a piranha solution, a wet thermal oxidation technique was used, and the cantilevers were held at $\sim 1000^\circ\text{C}$ for 45 minutes with nitrogen gas saturated with water vapour passing through the furnace. The cantilevers, after being cleaned in a piranha solution, were placed with the bonding surface exposed to the air flow inside the furnace. Ellipsometry showed oxide layers on both sides of the cantilever measured to be 231 ± 3 nm in thickness.

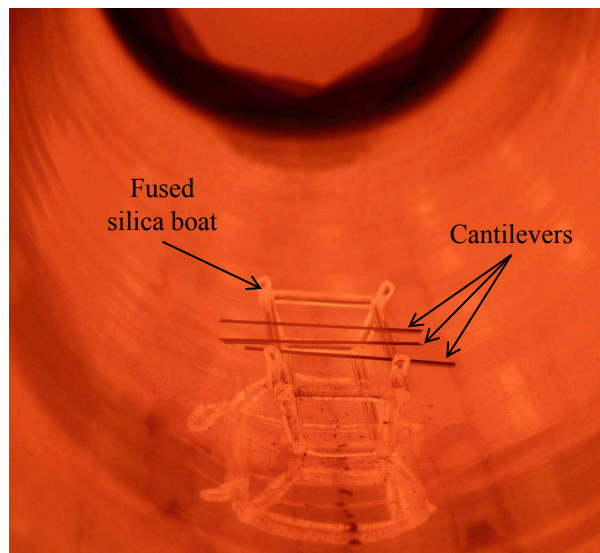


Figure 5.8: *Three cantilevers face down on a fused silica boat inside the furnace. The base of each cantilever, which is the bonding surface, is completely exposed to the saturated gas flow inside the furnace.*

The roughnesses of the oxidised top and bottom surfaces was measured for the $66\mu\text{m}$ cantilever (shown in Figure 5.9), using the Veeco Wyko NT1100 Optical surface profiler. The results were taken as indicative of the $26\mu\text{m}$ cantilever, which was not measured due its fragility.

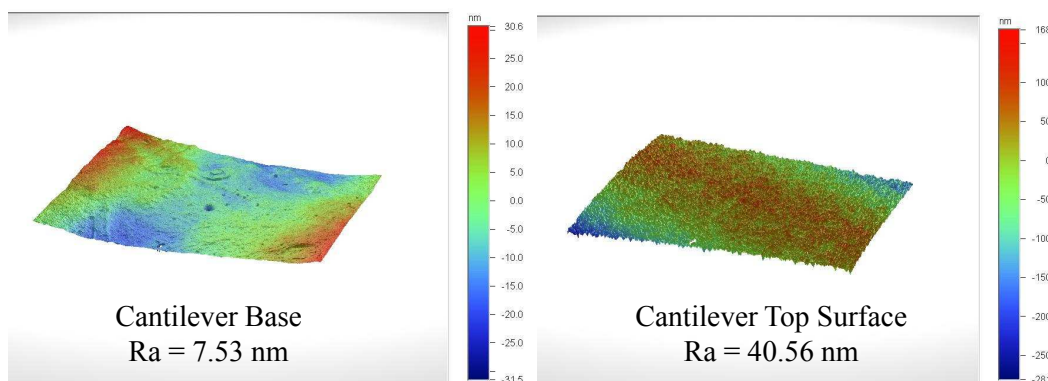


Figure 5.9: *Roughness measurements of the two oxidised surfaces of a cantilever, where R_a is the arithmetic average of the roughness profile. The base of the cantilever is the bonding surface, which shows the roughness to be low.*

Due to the delicate nature of the cantilevers, the cerium oxide cleaning regime detailed in Chapter 3 and typically used prior to bonding, could not be used. It was therefore necessary to clean the cantilevers prior to bonding using the same method that was used to clean the cantilevers before oxidation.

A piranha solution was prepared using a 7:1 ratio of sulphuric acid and hydrogen peroxide, and each cantilever was held in the solution for approximately one minute. This is shown in Figure 5.10. The cantilevers were then held in de-ionised water, to remove any traces of the piranha solution, and finally rinsed with methanol.

In order to ensure that the piranha solution clean would enable the bonding solution to be deposited on the surfaces, a series of tests were carried out on an oxidised silicon wafer that had been cleaned in this manner.

It was unknown how quickly the drop of bonding solution would spread over

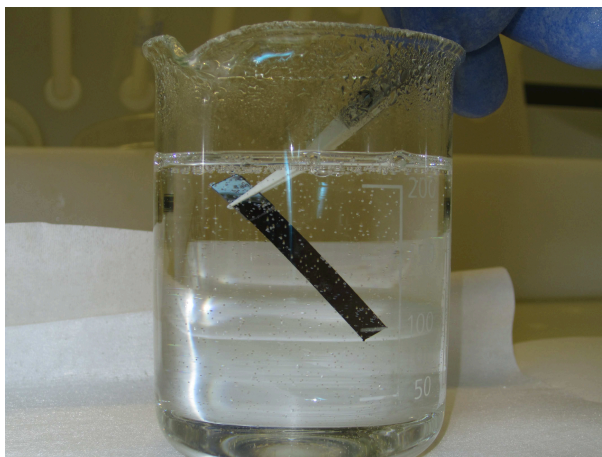


Figure 5.10: *The delicate nature of the silicon cantilevers required a change from the cerium oxide cleaning regime. Thus, the cantilevers were held in piranha solution prior to bonding.*

the cantilever surface, so a range of drop sizes was used. These can be seen in Figures 5.11 and 5.12. Approximately $1 \mu\text{l}$ of bonding solution was required to bond a surface area of 2.2 cm^2 at the standard volume/area ratio, so the drop sizes were chosen in order to be able to deposit the bonding solution in one, two, three, four or five drops.

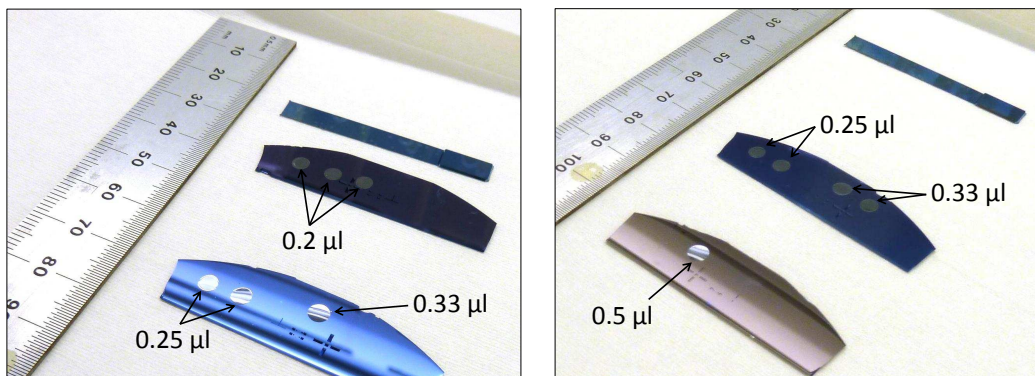


Figure 5.11: *Experiments with bonding solution on oxidised silicon wafer cleaned using piranha solution to determine the spread of the drop sizes from $0.2 \mu\text{l}$ to $0.6 \mu\text{l}$.*

A smaller number of drops is beneficial as this reduces the possibility of the introduction of contaminants such as dust particulates in the lab environment to the cantilevers during the period of time between the first drop of bonding

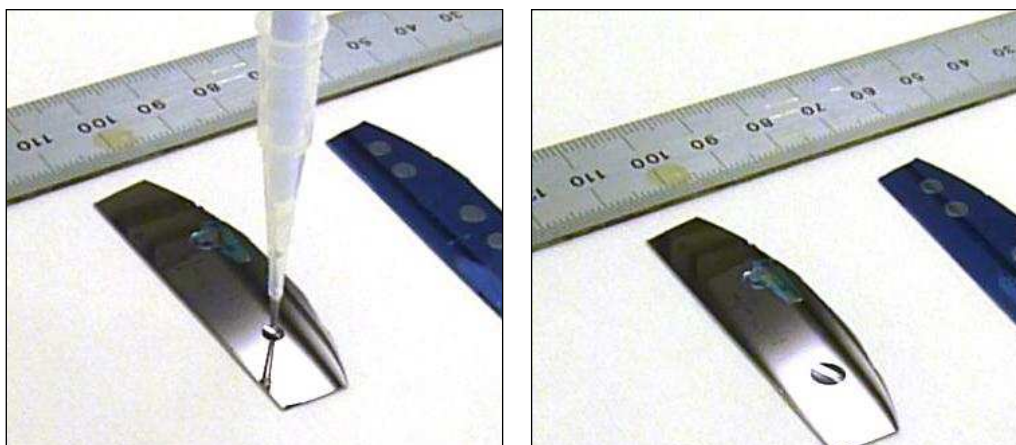


Figure 5.12: *The spread of a $1\mu\text{l}$ drop of bonding solution.*

solution being deposited and the two cantilevers being bonded. Another consideration is that the bonding process will begin within moments of the bonding solution being deposited onto the cantilever surface. However, a larger drop size may result in bonding solution wicking around the edges of the cantilevers if the droplet spreads out to cover the width of the cantilever.

It was seen that using $1\mu\text{l}$ of solution produced a drop that was within the width of the cantilever. A bonding trial was then performed using cantilevers with similar dimensions as the ones that would be used for the loss measurements but with equal thickness, to study the spread of the bonding solution. The trial is pictured in Figure 5.13, and the bond quality is shown in Figure 5.14.

When bonding pieces of silica, air bubbles can clearly be seen moving towards the edges of the bond during the first hours after bonding. This observation cannot be made when bonding silicon components because they are opaque to visible wavelengths. However, thermal imaging allows for bond quality to be observed in cases where the components are sufficiently thin. Figure 5.14 shows the thermal images of the trial bond 20 minutes and 18 hours after the bond was made. In this case, the thermal images show the bond to be

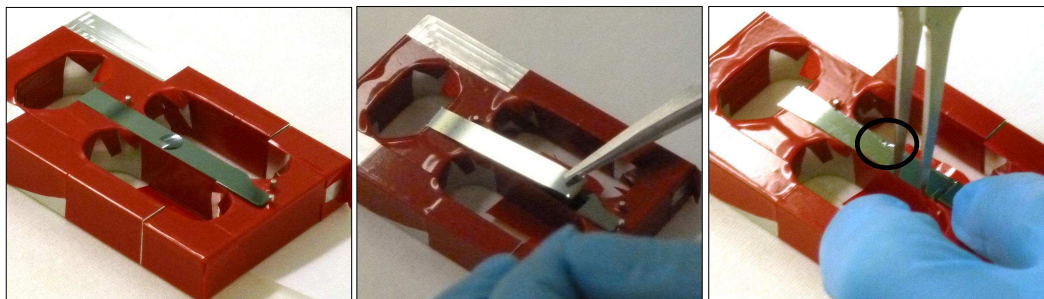


Figure 5.13: *Bonding a pair of cantilevers with 1 μl of bonding solution. In the third image, a small amount of bonding solution can be seen (circled) where the pressure of the top cantilever caused bond solution to 'wick' around to the top surface.*

free of significant voids even after 20 minutes and the bonding technique was successful, apart from the spreading of bonding solution on to the top surface of the cantilever.

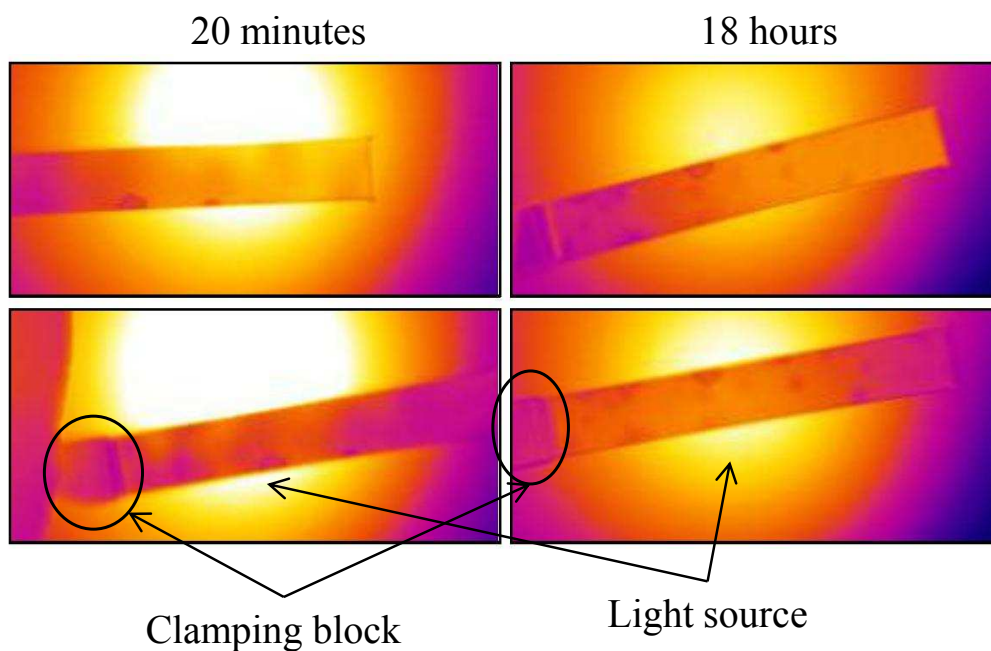


Figure 5.14: *Thermal images showing the bond between two silicon cantilevers after being bonded using one 1 μl drop of bonding solution. Once the bond is completely cured, if there are no voids or particulates between the two surfaces, the appearance should be uniform.*

To avoid the wicking of bonding solution observed in the trial onto the top surface of the cantilever, three drops of $0.33\ \mu\text{l}$ of bonding solution were used for the cantilevers in the loss measurement experiment. Once the cantilevers were bonded, the thinner cantilever appeared to be flexible enough to mould itself around the air bubbles in the bond. This dimpled effect is visible in the bottom photograph in Figure 5.15.



Figure 5.15: *Top: Three drops of bonding solution, each $0.33\ \mu\text{l}$ were used. Bottom: The bonded cantilever after 24 hours. Bonding solution that wicked around on to the top is visible, as is a square ‘dimple’ - a surface defect on the top surface of the cantilever due to the manufacturing process.*

Thermal images (shown in Figure 5.16) were taken at several stages during the four week curing period in order to monitor the changes in the bond. The lower half of the bond (nearest the clamping block) showed a significant improvement in bond quality during the curing period. The tip of the cantilever also showed improvement. Bubbles or contaminants on the bonding surfaces in this area however, resulted in a poorer quality of the bond.

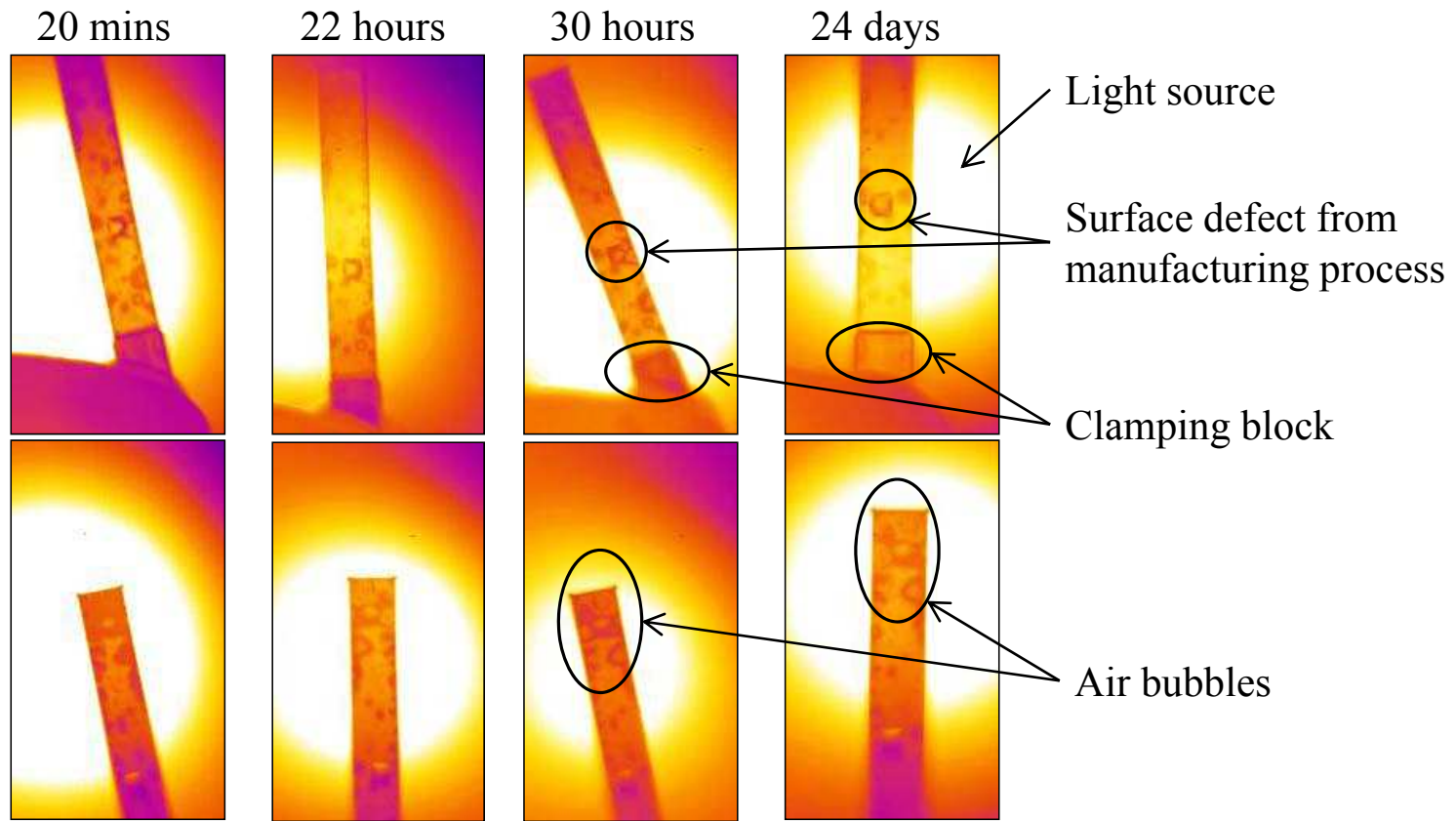


Figure 5.16: *The changes in the bond during the curing period can be seen in thermal images. Although the majority of the change is within 30 hours, some improvement is noted in the images taken 24 days after bonding.*

5.3 Results and Interpretation

5.3.1 Introduction

When exciting the bonded structure, only the second resonant mode was successfully excited. Therefore, the measurements of the second resonant modes for the unoxidised and oxidised cantilevers were used to calculate the loss of the oxide and bond layer.

Figure 5.17 shows the measured losses for the second resonant mode of the $66\mu\text{m}$ thick unoxidised silicon cantilever, along with the expected thermoelastic loss. The thermoelastic loss is calculated using equation 5.7, where the value for Young's Modulus is taken to be 164 GPa [136], the density of silicon is taken to be 2333kgm^{-3} [137], the thermal conductivity was taken from Touloukian [137], and the coefficient of thermal expansion and specific heat capacity were taken from Hull [138]. The thermoelastic loss limits were calculated using the minimum and maximum values for the thermal conductivity.

Previous measurements of uncoated silicon cantilevers have shown the mechanical loss can be somewhat lower than that shown in Figure 5.18 [136] at low temperature, suggesting that the measured loss value for ϕ_s here is higher than anticipated, possibly due to noise in the laboratory environment during the experiment and energy from the excited mode of the cantilever coupling into the clamping structure [136]. However, since the mechanical loss of a silicon substrate at high temperature is extremely close to the thermoelastic loss, and the intrinsic loss of the bonded structure is expected to be several orders of magnitude higher than the loss of the silicon substrate, the levels of ϕ_s seen here are expected to be low enough to allow a bond loss level to be obtained.

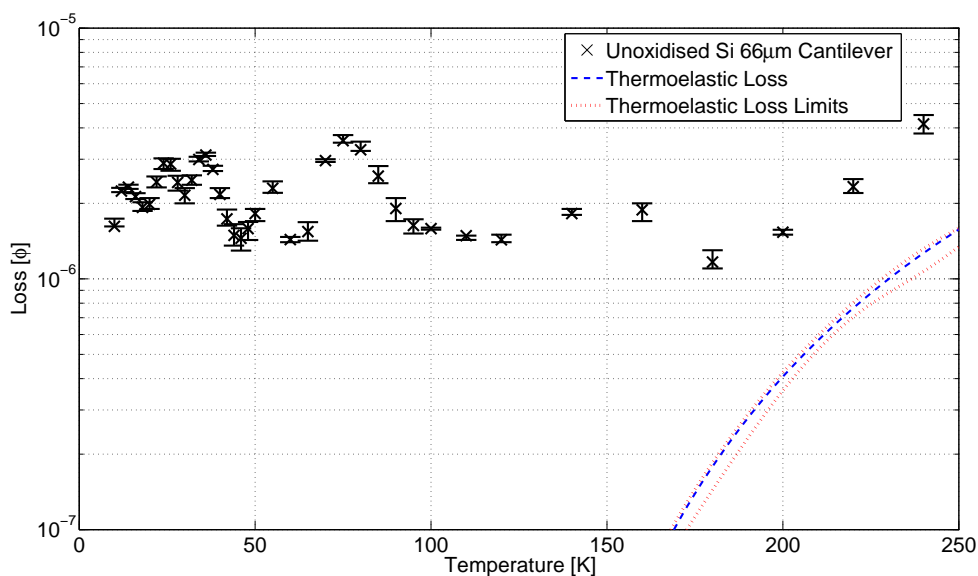


Figure 5.17: *The loss measurements for the 66 μm plain silicon cantilever, and the thermoelastic loss for the second mode, at 572 Hz.*

5.3.2 The Mechanical Loss in the Oxide Layers

The 66 μm thick cantilever was oxidised, and the loss of the mode at 572 Hz remeasured, as plotted in Figure 5.18. It can be seen, that at temperatures below ~ 75 K, the effects of the loss of the oxide layer are clearly visible. However, above ~ 75 K, the measured losses appear to be dominated by a combination of the excess losses discussed, and the thermoelastic loss of the substrate. Thus, values for the oxide loss were calculated predominantly over the temperature range from ~ 10 K to 75 K.

The calculated loss of the oxide layer, using equation 5.6, is shown in Figure 5.18.

5.3.3 Mechanical Loss of the Bond Layer

Figure 5.19 shows the measured loss for the bonded structure, at the second resonant mode of 736 Hz.

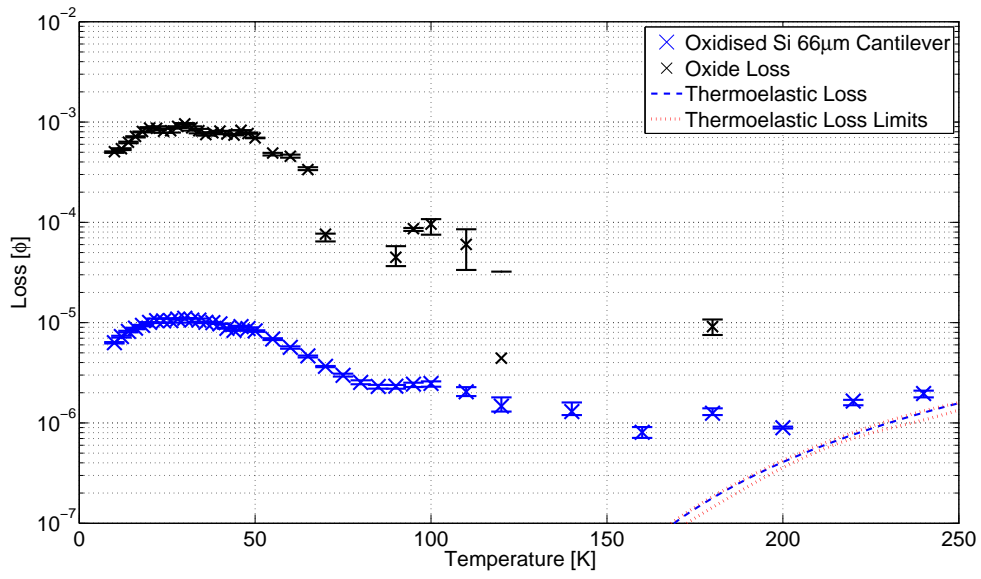


Figure 5.18: *The loss of the oxidised 66 µm cantilever and the calculated oxide loss.*

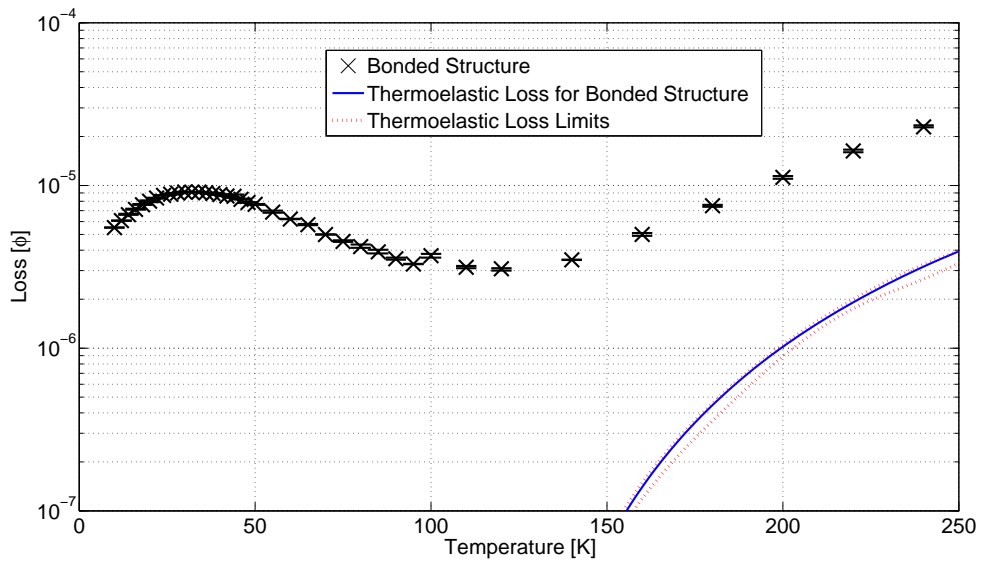


Figure 5.19: *The measured loss for the bonded structure.*

Applying equation 5.22:

$$\phi_b = \frac{E_t}{E_b} \left[\phi_m - \phi_s - \phi_{sTE} - 2 \frac{E_{o1}}{E_t} \phi_o - \frac{E_{o2}}{E_t} \phi_o - \frac{E_{o3}}{E_t} \phi_o \right],$$

and using equations 5.14 - 5.20, the mechanical loss of the bond layer can be determined. Due to the loss measurements of the $66\ \mu\text{m}$ cantilever being dominated above 75 K by excess losses, the results for the loss of the bond layer are restricted to the temperature range of 10 - 75 K.

Figure 5.20 show the mechanical loss of the bond layer, for the temperature range 10 - 75 K. The maximum loss measured between 10 and 75 K was 0.17 at 75 K, and the lowest loss measured was 0.04 at 20 K. The apparent structure visible in Figure 5.20 is attributed to the noise in the calculated loss of the oxide layer.

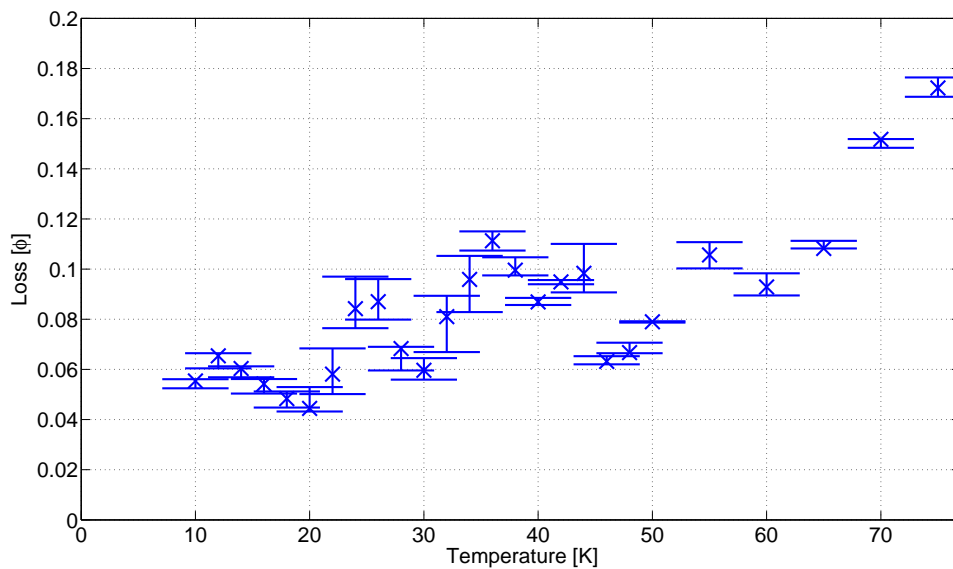


Figure 5.20: *The mechanical loss of the bond layer for the second mode at 736 Hz in the temperature range 10 - 75 K.*

5.4 Conclusions

The results obtained provide a new upper limit of 0.17 ± 0.004 for a hydroxide-catalysis bond between silicon at temperatures below 75 K. The minimum loss of 0.04 ± 0.008 was obtained at 20 K. These are below the calculated mechan-

ical loss of hydroxide-catalysis bonds between fused silica (0.49 ± 0.05) [104], currently used in the construction of Advanced LIGO.

These values were only obtained for the loss at the second resonant mode, as this was the only mode of the bonded structure that could be cleanly excited and of which the ring down could be recorded. The experiment was highly repeatable; however, with each of the three clampings of the bonded structure producing loss curves that were within a 5% of each other between 10 and 100 K, showing that the results were indeed reliable for this mode.

The bond between the cantilevers was not a completely uniform bond, as voids were visible in the top end of the cantilever. However, a large proportion of the bonded area was free of voids as opposed to previously reported bond loss values [124].

A more precise loss value over a wider temperature range could be obtained if a more consistent bond without voids was present between the two cantilevers, and multiple resonant modes were measured to further define the bond loss.

Chapter 6

Conclusions

An international scientific community has developed a global network of interferometric gravitational wave detectors that are now undergoing significant upgrades after completing initial searches for gravitational wave signals from astronomical events. These detectors operate by searching for changes in the positions of suspended mirrors, induced by the passage of gravitational waves. The detector upgrades, which will form the second generation of instruments, will increase the sensitivity of the first generation detectors by a factor of ~ 10 . These room temperature detectors will incorporate fused silica test mass mirrors suspended from fused silica fibres, jointed to the masses through the application of hydroxide-catalysis bonding, chosen due to a combination of its properties including having sufficiently low mechanical losses and thus thermal noise.

The thermal noise of an interferometer can potentially be further minimised by reducing the operating temperature of the test mass mirrors and suspensions to cryogenic temperatures. Research has begun into the development of cryogenic interferometric gravitational wave detectors as a future generation of detector system to improve upon the sensitivities expected from the second generation

detectors. Silicon may replace fused silica as the material used for the test mass mirrors and suspensions due to its low dissipation characteristics at cryogenic temperatures. This thesis focuses on the adaption of hydroxide-catalysis bonding for jointing silicon in the construction of the test mass suspensions.

Silicon requires a layer of SiO_2 on the bonding surface in order for a hydroxide-catalysis bond to successfully form. The strength of bonds between silicon samples and the minimum thickness of the layer required for a successful bond was investigated. Silicon blocks of dimensions 5×10 mm from Prolog ingots manufactured using the Czochralski process with crystallographic orientation $\langle 100 \rangle$ and $\langle 111 \rangle$ were thermally oxidised in a wet environment at 1000°C for varying periods of time in order to grown oxide layers with thicknesses between 0 and ~ 270 nm.

135 pairs of silicon blocks were bonded together such that a bonded sample had the dimensions of $5 \times 10 \times 40$ mm. 86 were strength tested at ~ 77 K, and 49 were tested at room temperature. The results from the strength tests showed a clear trend of decreasing strength once the minimum oxide layer was less than 50 nm and no significant difference in strength indicating that the strength of the bonds is not negatively influenced by thermal loading due to expansion differences between the bond and bulk material. The characteristic strength of all the samples studied at both cryogenic and at room temperature was above 20 MPa, with the potential to increase this by the identification and removal of factors negatively affecting the strength. This result showed the potential for hydroxide-catalysis bonding to be a technique used in the construction of silicon suspensions for a cryogenic gravitational wave detector when the bonding surfaces had a minimum oxide layer thickness of 50 nm.

Once the minimum oxide layer for a successful bond had been established, the nature of the oxide layer was investigated. Electron beam deposition, ion beam sputtering and dry thermal oxidation were used to apply an oxide layer

of approximately 150 nm onto silicon blocks. Silicon ingots of crystallographic orientation $\langle 100 \rangle$ and $\langle 111 \rangle$ were used, with the $\langle 100 \rangle$ ingot being manufactured by Shin-Etsu using the Float Zone method, and the $\langle 111 \rangle$ ingot being manufactured by Prolog using the Czochralski process.

The ion beam and e-beam oxide layers proved vulnerable to the cerium oxide cleaning procedure, with approximately 25 nm of oxide layer worn away after cleaning. The e-beam samples were the weakest set of samples, at both cryogenic and room temperature, while the cryogenic strengths were consistently higher than room temperature strengths. The dry thermal oxide produced the strongest and most consistent range of strengths.

When samples broke along the bond, each oxide type produced distinctive break patterns. The e-beam samples had bond break surfaces that were uniform in colour, and ellipsometry showed the thickness of the oxide layer to be unchanged, suggesting the bond failed to form, leaving the oxide layers in tact. This, combined with the low strength, implies that e-beam deposition is not a desirable technique to be used in the construction of suspensions for a gravitational wave detector. Ion beam sputtering and thermal oxides can still be considered, however the cleaning technique would need to be carefully adapted to prevent erosion of the ion beam sputtered oxide layer.

Further, the mechanical loss of a hydroxide-catalysis bond between silicon samples was measured to determine its loss, to enable its contribution to the overall thermal noise of a suspension to be assessed. The mechanical loss of a cantilever can be measured through exciting its bending modes and measuring the ringdown time of each mode in a vacuum. Two cantilevers of different thicknesses were measured in this way at temperature steps between 10 and 250 K before being thermally oxidised and re-measured in the same way. They were then bonded together such that the bond was offset from the centre of the bonded structure. By then measuring the ringdowns of the bonded structure,

the loss of the bond can be extracted at each temperature step.

An upper limit of the loss of a hydroxide-catalysis bond between silicon of 0.18 ± 0.004 was obtained at temperatures below 75 K. The minimum loss of 0.04 ± 0.008 was obtained at 20 K. These low values, which are below those calculated for the hydroxide-catalysis bonds between silica, show that hydroxide-catalysis bonding may be a suitable jointing technique for future cryogenic gravitational wave detectors.

Appendix A

Weibull Analysis Code

This code was written by Prof. Martin Hendry.

```
program weibul\\
  implicit double precision(a-h,o-z)\\
  double precision fdata(100),pdata(100)\\
  double precision chain_m(1000000),chain_f0(1000000)\\
  double precision m_sorted(1000000),f0_sorted(1000000)\\
  double precision loglike(1000000), array(1000000)\\
  double precision xdata(100),ydata(100)\\
  double precision x_line(450),y_line(450)\\
  double precision f_fit(10000),cdf_fit(10000),\\
*cdf_lin(10000)\\
  integer nsample(18),index(1000000)\\
  external uniform, gaussian, xllike, heapsort\\
  common/mcmc/fdata,sumlnf,pts,npts\\
  common/sort/array,index,n_mcmc
```

C *****

```
  nsample(1) = 80\\
  nsample(2) = 49\\
  nsample(3) = 33\\
  nsample(4) = 37\\
  nsample(5) = 7\\
  nsample(6) = 17\\
  nsample(7) = 29\\
  nsample(8) = 32\\
```

```
nsample(9) = 4\\
nsample(10) = 5\\
nsample(11) = 16\\
nsample(12) = 14\\
nsample(13) = 17\\
nsample(14) = 23\\
nsample(15) = 25\\
nsample(16) = 20\\
nsample(17) = 8\\
nsample(18) = 17\\
```

c ***** Commencing loop over samples

```
do nsamp = 1,18\\
  print*, ' Beginning sample number ', nsamp\\
  npts = nsample(nsamp)\\
  pts = dble(npts)\\
  if(nsamp.eq.1)then\\
    open(unit=99,file='sample01.dat',status='unknown')\\
    open(unit=98,file='fitdata01.dat',status='unknown')\\
  endif\\
  if(nsamp.eq.2)then\\
    open(unit=99,file='sample02.dat',status='unknown')\\
    open(unit=98,file='fitdata02.dat',status='unknown')\\
  endif\\
  if(nsamp.eq.3)then\\
    open(unit=99,file='sample03.dat',status='unknown')\\
    open(unit=98,file='fitdata03.dat',status='unknown')\\
  endif\\
  if(nsamp.eq.4)then\\
    open(unit=99,file='sample04.dat',status='unknown')\\
    open(unit=98,file='fitdata04.dat',status='unknown')\\
  endif\\
  if(nsamp.eq.5)then\\
    open(unit=99,file='sample05.dat',status='unknown')\\
    open(unit=98,file='fitdata05.dat',status='unknown')\\
  endif\\
  if(nsamp.eq.6)then\\
    open(unit=99,file='sample06.dat',status='unknown')\\
    open(unit=98,file='fitdata06.dat',status='unknown')\\
  endif\\
  if(nsamp.eq.7)then\\
    open(unit=99,file='sample07.dat',status='unknown')\\
```

```
    open(unit=98,file='fitdata07.dat',status='unknown')\\
endif\\
if(nsamp.eq.8)then\\
    open(unit=99,file='sample08.dat',status='unknown')\\
    open(unit=98,file='fitdata08.dat',status='unknown')\\
endif\\
if(nsamp.eq.9)then\\
    open(unit=99,file='sample09.dat',status='unknown')\\
    open(unit=98,file='fitdata09.dat',status='unknown')\\
endif\\
if(nsamp.eq.10)then\\
    open(unit=99,file='sample10.dat',status='unknown')\\
    open(unit=98,file='fitdata10.dat',status='unknown')\\
endif\\
if(nsamp.eq.11)then\\
    open(unit=99,file='sample11.dat',status='unknown')\\
    open(unit=98,file='fitdata11.dat',status='unknown')\\
endif\\
if(nsamp.eq.12)then\\
    open(unit=99,file='sample12.dat',status='unknown')\\
    open(unit=98,file='fitdata12.dat',status='unknown')\\
endif\\
if(nsamp.eq.13)then\\
    open(unit=99,file='sample13.dat',status='unknown')\\
    open(unit=98,file='fitdata13.dat',status='unknown')\\
endif\\
if(nsamp.eq.14)then\\
    open(unit=99,file='sample14.dat',status='unknown')\\
    open(unit=98,file='fitdata14.dat',status='unknown')\\
endif\\
if(nsamp.eq.15)then\\
    open(unit=99,file='sample15.dat',status='unknown')\\
    open(unit=98,file='fitdata15.dat',status='unknown')\\
endif\\
if(nsamp.eq.16)then\\
    open(unit=99,file='sample16.dat',status='unknown')\\
    open(unit=98,file='fitdata16.dat',status='unknown')\\
endif\\
if(nsamp.eq.17)then\\
    open(unit=99,file='sample17.dat',status='unknown')\\
    open(unit=98,file='fitdata17.dat',status='unknown')\\
endif\\
if(nsamp.eq.18)then\\
```

```
        open(unit=99,file='sample18.dat',status='unknown')\\
        open(unit=98,file='fitdata18.dat',status='unknown')\\
    endif\\

c ***** First sort the F values into increasing order

    do ipt = 1,npts\\
        read(99,*)fdata(ipt)\\
    enddo\\
    close(99)\\
    do ipt = 1,npts\\
        do jpt = ipt,npts\\
            if(fdata(ipt).gt.fdata(jpt))then\\
                ftemp = fdata(ipt)\\
                fdata(ipt) = fdata(jpt)\\
                fdata(jpt) = ftemp\\
            endif\\
        enddo\\
    enddo\\
    do ipt = 1,npts\\

c ***** Compute values of x and y, using the formula 2b

        xdata(ipt) = dlog(fdata(ipt)) \\
        pdata(ipt) = (dble(ipt) - 0.3d0)/(pts + 0.4d0)\\
        ydata(ipt) = dlog(dlog(1.d0/(1.d0-pdata(ipt))))\\
        write(98,1111)ipt,fdata(ipt),pdata(ipt),\\
*xdata(ipt),ydata(ipt)\\
        enddo\\

1111    format(i2,1x,f14.8,1x,f14.8,1x,f14.8,1x,f14.8)\\
        close(98)

c ***** Now compute best-fit straight line and convert\\
c ***** to corresponding m and F0 values\\

        xsm = 0.d0\\
        xsq = 0.d0\\
        ysm = 0.d0\\
        ysq = 0.d0\\
        xysm = 0.d0\\
        do ipt = 1,npts\\
            xsm = xsm + xdata(ipt)\\
```

```

    ysm = ysm + ydata(ipt)\
    xsq = xsq + xdata(ipt)*xdata(ipt)\
    ysq = ysq + ydata(ipt)*ydata(ipt)\
    xysm = xysm + xdata(ipt)*ydata(ipt)\
  enddo\
  slope = (pts*xysm - xsm*ysm)/(pts*xsq - xsm*xsm)\
  zept = (ysm*xsq - xysm*xsm)/(pts*xsq - xsm*xsm)\
  fitted_m = slope\
  fitted_f0 = dexp(-zept/slope)\

c ***** Given these fitted values compute a best-fit line\
c ***** in the (x,y) plane\

  do ixy = 1,450\
    x_line(ixy) = 0.01d0*ixy\
    y_line(ixy) = slope*x_line(ixy) + zept\
  enddo\

c ***** Write out data ready for MATLAB

  if(nsamp.eq.1)then\
    open(unit=99,file='linplot01.dat',status='unknown')\
  endif\
  if(nsamp.eq.2)then\
    open(unit=99,file='linplot02.dat',status='unknown')\
  endif\
  if(nsamp.eq.3)then\
    open(unit=99,file='linplot03.dat',status='unknown')\
  endif\
  if(nsamp.eq.4)then\
    open(unit=99,file='linplot04.dat',status='unknown')\
  endif\
  if(nsamp.eq.5)then\
    open(unit=99,file='linplot05.dat',status='unknown')\
  endif\
  if(nsamp.eq.6)then
    open(unit=99,file='linplot06.dat',status='unknown')
  endif
  if(nsamp.eq.7)then
    open(unit=99,file='linplot07.dat',status='unknown')
  endif
  if(nsamp.eq.8)then
    open(unit=99,file='linplot08.dat',status='unknown')
  endif

```

```
endif
if(nsamp.eq.9)then
  open(unit=99,file='linplot09.dat',status='unknown')
endif
if(nsamp.eq.10)then
  open(unit=99,file='linplot10.dat',status='unknown')
endif
if(nsamp.eq.11)then
  open(unit=99,file='linplot11.dat',status='unknown')
endif
if(nsamp.eq.12)then
  open(unit=99,file='linplot12.dat',status='unknown')
endif
if(nsamp.eq.13)then
  open(unit=99,file='linplot13.dat',status='unknown')
endif
if(nsamp.eq.14)then
  open(unit=99,file='linplot14.dat',status='unknown')
endif
if(nsamp.eq.15)then
  open(unit=99,file='linplot15.dat',status='unknown')
endif
if(nsamp.eq.16)then
  open(unit=99,file='linplot16.dat',status='unknown')
endif
if(nsamp.eq.17)then
  open(unit=99,file='linplot17.dat',status='unknown')
endif
if(nsamp.eq.18)then
  open(unit=99,file='linplot18.dat',status='unknown')
endif

do ixy = 1,450
  write(99,2222)x_line(ixy),y_line(ixy)
enddo

2222  format(f14.8,1x,f14.8)
      close(99)

c ***** Now ready to begin MCMC search

sumlnf = 0.d0
do ipt = 1,npts
```

```
        sumlnf = sumlnf + dlog(fdata(ipt))
    enddo
    n_mcmc = 100000
    iseed = -2
    xm_init = fitted_m
    f0_init = fitted_f0

c      xm_init = uniform(0.d0,10.d0,iseed)

c      f0_init = uniform(0.d0,100.d0,iseed)

    xm_min = 0.d0
    xm_max = 20.d0
    f0_min = 0.d0
    f0_max = 100.d0
    prop_m_sig = 0.25d0
    prop_f0_sig = 1.d0
    chain_m(1) = xm_init
    chain_f0(1) = f0_init
    loglike(1) = xllike(xm_init,f0_init)
    sum_m = chain_m(1)
    sum_f0 = chain_f0(1)

c ***** Beginning MCMC loop

    print*, ' Doing MCMC search for sample ', nsamp
    do imcmc = 2, n_mcmc
        xm = chain_m(imcmc-1)
        f0 = chain_f0(imcmc-1)
        xllike_old = xllike(xm, f0)
446    xm_move = gaussian(0.d0, prop_m_sig, iseed)
        xm_new = xm + xm_move
        f0_move = gaussian(0.d0, prop_f0_sig, iseed)
        f0_new = f0 + f0_move
        if(xm_new.lt.xm_min.or.xm_new.gt.xm_max) goto 446
        if(f0_new.lt.f0_min.or.f0_new.gt.f0_max) goto 446
        xllike_new = xllike(xm_new, f0_new)

c ***** Now determine if new point should be included

        diff = xllike_new - xllike_old
        if(diff.ge.0.d0) then
            chain_m(imcmc) = xm_new
```

```
        chain_f0(imcmc) = f0_new
        loglike(imcmc) = xllike_new
    else

c ***** In this case we accept the proposal point with prob R
c ***** First compute probability ratio

        ratio = dexp(diff)
        rat_check = uniform(0.d0,1.d0,iseed)
        if(rat_check.le.ratio)then
            chain_m(imcmc) = xm_new
            chain_f0(imcmc) = f0_new
            loglike(imcmc) = xllike_new
        else
            chain_m(imcmc) = xm
            chain_f0(imcmc) = f0
            loglike(imcmc) = xllike_old
        endif
    endif
    sum_m = sum_m + chain_m(imcmc)
    sum_f0 = sum_f0 + chain_f0(imcmc)

c        frac = dble(imcmc)/100.d0 - idint(dble(imcmc)/100.d0)
c        if(frac.eq.0.d0)then
c            write(*,*)' Doing ',imcmc
c        endif

c ***** Ready to move on to next point in chain

        enddo
        close(99)

c ***** Chain completed. Ready to sort values

        print*, ' Sorting log likelihood pairs for sample ',nsamp
        do imcmc = 1,n_mcmc
            array(imcmc) = loglike(imcmc)
            index(imcmc) = imcmc
        enddo
        call heapsort

c ***** Now write out sorted values to new arrays
```

```
do imcmc = 1,n_mcmc
  loglike(imcmc) = array(imcmc)
  m_sorted(imcmc) = chain_m(index(imcmc))
  f0_sorted(imcmc) = chain_f0(index(imcmc))
enddo
xm_ml = m_sorted(1)
f0_ml = f0_sorted(1)

c ***** Writing out chain points: 68% truncated sample and full sample
if(nsamp.eq.1)then
  open(unit=99,file='mcmc_chain01.dat',status='unknown')
  open(unit=98,file='mcmc_trunc01.dat',status='unknown')
endif
if(nsamp.eq.2)then
  open(unit=99,file='mcmc_chain02.dat',status='unknown')
  open(unit=98,file='mcmc_trunc02.dat',status='unknown')
endif
if(nsamp.eq.3)then
  open(unit=99,file='mcmc_chain03.dat',status='unknown')
  open(unit=98,file='mcmc_trunc03.dat',status='unknown')
endif
if(nsamp.eq.4)then
  open(unit=99,file='mcmc_chain04.dat',status='unknown')
  open(unit=98,file='mcmc_trunc04.dat',status='unknown')
endif
if(nsamp.eq.5)then
  open(unit=99,file='mcmc_chain05.dat',status='unknown')
  open(unit=98,file='mcmc_trunc05.dat',status='unknown')
endif
if(nsamp.eq.6)then
  open(unit=99,file='mcmc_chain06.dat',status='unknown')
  open(unit=98,file='mcmc_trunc06.dat',status='unknown')
endif
if(nsamp.eq.7)then
  open(unit=99,file='mcmc_chain07.dat',status='unknown')
  open(unit=98,file='mcmc_trunc07.dat',status='unknown')
endif
if(nsamp.eq.8)then
  open(unit=99,file='mcmc_chain08.dat',status='unknown')
  open(unit=98,file='mcmc_trunc08.dat',status='unknown')
endif
if(nsamp.eq.9)then
  open(unit=99,file='mcmc_chain09.dat',status='unknown')
```

```
        open(unit=98,file='mcmc_trunc09.dat',status='unknown')
    endif
    if(nsamp.eq.10)then
        open(unit=99,file='mcmc_chain10.dat',status='unknown')
        open(unit=98,file='mcmc_trunc10.dat',status='unknown')
    endif
    if(nsamp.eq.11)then
        open(unit=99,file='mcmc_chain11.dat',status='unknown')
        open(unit=98,file='mcmc_trunc11.dat',status='unknown')
    endif
    if(nsamp.eq.12)then
        open(unit=99,file='mcmc_chain12.dat',status='unknown')
        open(unit=98,file='mcmc_trunc12.dat',status='unknown')
    endif
    if(nsamp.eq.13)then
        open(unit=99,file='mcmc_chain13.dat',status='unknown')
        open(unit=98,file='mcmc_trunc13.dat',status='unknown')
    endif
    if(nsamp.eq.14)then
        open(unit=99,file='mcmc_chain14.dat',status='unknown')
        open(unit=98,file='mcmc_trunc14.dat',status='unknown')
    endif
    if(nsamp.eq.15)then
        open(unit=99,file='mcmc_chain15.dat',status='unknown')
        open(unit=98,file='mcmc_trunc15.dat',status='unknown')
    endif
    if(nsamp.eq.16)then
        open(unit=99,file='mcmc_chain16.dat',status='unknown')
        open(unit=98,file='mcmc_trunc16.dat',status='unknown')
    endif
    if(nsamp.eq.17)then
        open(unit=99,file='mcmc_chain17.dat',status='unknown')
        open(unit=98,file='mcmc_trunc17.dat',status='unknown')
    endif
    if(nsamp.eq.18)then
        open(unit=99,file='mcmc_chain18.dat',status='unknown')
        open(unit=98,file='mcmc_trunc18.dat',status='unknown')
    endif

    length = idint(0.68*n_mcmc + 0.5d0)
    do imcmc = 1,length
        write(98,667) imcmc,m_sorted(imcmc),f0_sorted(imcmc),
        *loglike(imcmc)
```

```

667     format(i8,1x,f16.10,1x,f16.10,1x,f16.10)
       enddo
       do imcmc = 1,n_mcmc
         write(99,667)imcmc,m_sorted(imcmc),f0_sorted(imcmc),
 *loglike(imcmc)
       enddo

c *****

       print*, ' Sorting marginal m values for sample ',nsamp
       do imcmc = 1,n_mcmc
         array(imcmc) = chain_m(imcmc)
         index(imcmc) = imcmc
       enddo
       call heapsort
       do imcmc = 1,n_mcmc
         m_sorted(imcmc) = array(imcmc)
       enddo
       print*, ' Sorting marginal F0 values for sample ',nsamp
       do imcmc = 1,n_mcmc
         array(imcmc) = chain_f0(imcmc)
         index(imcmc) = imcmc
       enddo
       call heapsort
       do imcmc = 1,n_mcmc
         f0_sorted(imcmc) = array(imcmc)
       enddo

c ***** Compute 68%, 95% errors

       n68_hi = idint(0.16d0*dble(n_mcmc) + 0.5d0)
       n68_lo = idint(0.84d0*dble(n_mcmc) + 0.5d0) + 1
       n95_hi = idint(0.025d0*dble(n_mcmc) + 0.5d0)
       n95_lo = idint(0.975d0*dble(n_mcmc) + 0.5d0) + 1

c ***** Ready to compute posterior pdf statistics

       xm_sm = 0.d0
       xm_sq = 0.d0
       f0_sm = 0.d0
       f0_sq = 0.d0
       do imcmc = 1,n_mcmc
         xm_sm = xm_sm + m_sorted(imcmc)

```

```

        xm_sq = xm_sq + m_sorted(imcmc)*
*m_sorted(imcmc)
        f0_sm = f0_sm + f0_sorted(imcmc)
        f0_sq = f0_sq + f0_sorted(imcmc)*
*f0_sorted(imcmc)
    enddo
    xm_mean = xm_sm / dble(n_mcmc)
    xm_var = (xm_sq/dble(n_mcmc)) - xm_mean*xm_mean
    f0_mean = f0_sm / dble(n_mcmc)
    f0_var = (f0_sq/dble(n_mcmc)) - f0_mean*f0_mean
    print*, ' RESULTS FOR SAMPLE ', nsamp
    print*, ' Linear fitted m = ', fitted_m
    print*, ' Linear fitted F0 = ', fitted_f0
    print*, ' Maximum likelihood estimates: '
    print*, ' m = ', xm_ml
    print*, ' F0 = ', f0_ml
    print*, ' '
    print*, '          Mean m = ', xm_mean
    xm68_lo = xm_mean - m_sorted(n68_lo)
    xm68_hi = m_sorted(n68_hi) - xm_mean
    print*, ' + 68% error = ', xm68_hi
    print*, ' - 68% error = ', xm68_lo
    xm95_lo = xm_mean - m_sorted(n95_lo)
    xm95_hi = m_sorted(n95_hi) - xm_mean
    print*, ' + 95% error = ', xm95_hi
    print*, ' - 95% error = ', xm95_lo
    print*, '          S.D. m = ', dsqrt(xm_var)
    print*, ' '
    print*, '          Mean f0 = ', f0_mean
    f068_lo = f0_mean - f0_sorted(n68_lo)
    f068_hi = f0_sorted(n68_hi) - f0_mean
    print*, ' + 68% error = ', f068_hi
    print*, ' - 68% error = ', f068_lo
    f095_lo = f0_mean - f0_sorted(n95_lo)
    f095_hi = f0_sorted(n95_hi) - f0_mean
    print*, ' + 95% error = ', f095_hi
    print*, ' - 95% error = ', f095_lo
    print*, '          S.D. f0 = ', dsqrt(f0_var)
    print*, ' '

```

c ***** Open results file

```

if(nsamp.eq.1)open(unit=99,file='results_samp01.dat',

```

```
*status='unknown')
  if(nsamp.eq.2)open(unit=99,file='results_samp02.dat',
*status='unknown')
  if(nsamp.eq.3)open(unit=99,file='results_samp03.dat',
*status='unknown')
  if(nsamp.eq.4)open(unit=99,file='results_samp04.dat',
*status='unknown')
  if(nsamp.eq.5)open(unit=99,file='results_samp05.dat',
*status='unknown')
  if(nsamp.eq.6)open(unit=99,file='results_samp06.dat',
*status='unknown')
  if(nsamp.eq.7)open(unit=99,file='results_samp07.dat',
*status='unknown')
  if(nsamp.eq.8)open(unit=99,file='results_samp08.dat',
*status='unknown')
  if(nsamp.eq.9)open(unit=99,file='results_samp09.dat',
*status='unknown')
  if(nsamp.eq.10)open(unit=99,file='results_samp10.dat',
*status='unknown')
  if(nsamp.eq.11)open(unit=99,file='results_samp11.dat',
*status='unknown')
  if(nsamp.eq.12)open(unit=99,file='results_samp12.dat',
*status='unknown')
  if(nsamp.eq.13)open(unit=99,file='results_samp13.dat',
*status='unknown')
  if(nsamp.eq.14)open(unit=99,file='results_samp14.dat',
*status='unknown')
  if(nsamp.eq.15)open(unit=99,file='results_samp15.dat',
*status='unknown')
  if(nsamp.eq.16)open(unit=99,file='results_samp16.dat',
*status='unknown')
  if(nsamp.eq.17)open(unit=99,file='results_samp17.dat',
*status='unknown')
  if(nsamp.eq.18)open(unit=99,file='results_samp18.dat',
*status='unknown')

write(99,*)' Linear fitted m = ',fitted_m
write(99,*)' Linear fitted F0 = ',fitted_f0
write(99,*)' '
write(99,*)' Maxmimum likelihood estimates: '
write(99,*)' m = ',xm_ml
write(99,*)' F0 = ',f0_ml
write(99,*)' '
```

```

write(99,*)'          Mean m = ',xm_mean
xm68_lo = xm_mean - m_sorted(n68_lo)
xm68_hi = m_sorted(n68_hi) - xm_mean
write(99,*)'    + 68% error = ',xm68_hi
write(99,*)'    - 68% error = ',xm68_lo
xm95_lo = xm_mean - m_sorted(n95_lo)
xm95_hi = m_sorted(n95_hi) - xm_mean
write(99,*)'    + 95% error = ',xm95_hi
write(99,*)'    - 95% error = ',xm95_lo
write(99,*)'          S.D. m = ',dsqrt(xm_var)
write(99,*)' '
write(99,*)'          Mean f0 = ',f0_mean
f068_lo = f0_mean - f0_sorted(n68_lo)
f068_hi = f0_sorted(n68_hi) - f0_mean
write(99,*)'    + 68% error = ',f068_hi
write(99,*)'    - 68% error = ',f068_lo
f095_lo = f0_mean - f0_sorted(n95_lo)
f095_hi = f0_sorted(n95_hi) - f0_mean
write(99,*)'    + 95% error = ',f095_hi
write(99,*)'    - 95% error = ',f095_lo
write(99,*)'          S.D. f0 = ',dsqrt(f0_var)
write(99,*)' '
close(99)

```

```

c ***** Compute fits to Weibull model CDF, both using
c ***** ML parameter estimates and best-fitting line

```

```

if(nsamp.eq.1)then
  open(unit=99,file='cdfplot01.dat',status='unknown')
endif
if(nsamp.eq.2)then
  open(unit=99,file='cdfplot02.dat',status='unknown')
endif
if(nsamp.eq.3)then
  open(unit=99,file='cdfplot03.dat',status='unknown')
endif
if(nsamp.eq.4)then
  open(unit=99,file='cdfplot04.dat',status='unknown')
endif
if(nsamp.eq.5)then
  open(unit=99,file='cdfplot05.dat',status='unknown')
endif
if(nsamp.eq.6)then

```

```
        open(unit=99,file='cdfplot06.dat',status='unknown')
    endif
    if(nsamp.eq.7)then
        open(unit=99,file='cdfplot07.dat',status='unknown')
    endif
    if(nsamp.eq.8)then
        open(unit=99,file='cdfplot08.dat',status='unknown')
    endif
    if(nsamp.eq.9)then
        open(unit=99,file='cdfplot09.dat',status='unknown')
    endif
    if(nsamp.eq.10)then
        open(unit=99,file='cdfplot10.dat',status='unknown')
    endif
    if(nsamp.eq.11)then
        open(unit=99,file='cdfplot11.dat',status='unknown')
    endif
    if(nsamp.eq.12)then
        open(unit=99,file='cdfplot12.dat',status='unknown')
    endif
    if(nsamp.eq.13)then
        open(unit=99,file='cdfplot13.dat',status='unknown')
    endif
    if(nsamp.eq.14)then
        open(unit=99,file='cdfplot14.dat',status='unknown')
    endif
    if(nsamp.eq.15)then
        open(unit=99,file='cdfplot15.dat',status='unknown')
    endif
    if(nsamp.eq.16)then
        open(unit=99,file='cdfplot16.dat',status='unknown')
    endif
    if(nsamp.eq.17)then
        open(unit=99,file='cdfplot17.dat',status='unknown')
    endif
    if(nsamp.eq.18)then
        open(unit=99,file='cdfplot18.dat',status='unknown')
    endif

    do ixy = 1,10000
        f_fit(ixy) = 0.01d0*ixy
        cdf_fit(ixy) = 1.d0 -
*dexp(-(f_fit(ixy)/f0_ml)**xm_ml)
```

```
        cdf_lin(ixy) = 1.d0 -
*dexp(-(f_fit(ixy)/fitted_f0)**fitted_m)
        write(99,3333)f_fit(ixy),cdf_fit(ixy),cdf_lin(ixy)
3333    format(f14.8,1x,f14.8,1x,f14.8)
        enddo
        close(99)
    enddo
end
```

```
double precision function xllike(xm,f0)
implicit double precision(a-h,o-z)
double precision fdata(100)
common/mcmc/fdata,sumlnf,pts,npts
term3 = (xm-1.d0)*sumlnf
term4 = 1.d0/(f0**xm)
sumfm = 0.d0
do ipt = 1,npts
    sumfm = sumfm + fdata(ipt)**xm
enddo
xllike = pts*dlog(xm) - xm*pts*dlog(f0) + term3 -
* term4*sumfm
return
end
```

```
double precision function uniform(a,b,idum)
implicit double precision(a-h,o-z)
external ran3
x = ran3(idum)
uniform = a + (b-a)*x
return
end
```

```
double precision function gaussian(a,b,idum)
implicit double precision(a-h,o-z)
external gasdev
x = gasdev(idum)
gaussian = a + b*x
return
end
```

```
double precision function gasdev(idum)
integer idum
integer iset
```

```
double precision fac,gset,rsq,v1,v2,ran3
save iset, gset
data iset/0/
if (idum.lt.0) iset=0
if (iset.eq.0) then
1   v1=2.d0*ran3(idum)-1
    v2=2.d0*ran3(idum)-1
    rsq=v1**2+v2**2
    if (rsq.ge.1.d0.or.rsq.eq.0.d0) goto 1
    fac=sqrt(-2.d0*dlog(rsq)/rsq)
    gset=v1*fac
    gasdev=v2*fac
    iset=1
else
    gasdev=gset
    iset = 0
endif
return
end

double precision function ran3(idum)
integer idum
integer mbig,mseed,mz
double precision fac
parameter(mbig=1000000000,mseed=161803398,mz=0,fac=1.d0/mbig)
integer i,iff,ii,inext,inextp,k
integer mj,mk,ma(55)
save iff,inext,inextp,ma
data iff /0/
if(idum.lt.0.or.iff.eq.0)then
    iff = 1
    mj = abs(mseed-abs(idum))
    mj = mod(mj,mbig)
    ma(55) = mj
    mk = 1
    do i = 1,54
        ii = mod(21*i,55)
        ma(ii) = mk
        mk = mj - mk
        if(mk.lt.mz)mk = mk + mbig
        mj = ma(ii)
    enddo
    do k = 1,4
```

```

        do i = 1,55
            ma(i) = ma(i) - ma(1+mod(i+30,55))
            if(ma(i).lt.mz)ma(i)=ma(i)+mbig
        enddo
    enddo
    inext = 0
    inextp = 31
    idum = 1
endif
inext = inext + 1
if(inext.eq.56)inext = 1
inextp = inextp + 1
if(inextp.eq.56)inextp = 1
mj = ma(inext)-ma(inextp)
if(mj.lt.mz)mj=mj+mbig
ma(inext) = mj
ran3 = mj*fac
return
end

subroutine heapsort
implicit double precision(a-h,o-z)
double precision array(1000000)
integer index(1000000)
common/sort/array,index,n_mcmc
nhalf = n_mcmc/2
do m = nhalf,1,-1
    temp = array(m)
    itemp = index(m)
    i1 = m
    i2 = m + m
1    continue
    if(i2.lt.n_mcmc.and.array(i2+1).lt.array(i2))
*i2=i2+1
    if(array(i2).lt.temp) then
        array(i1) = array(i2)
        index(i1) = index(i2)
        i1 = i2
        i2 = i1 + i1
    else
        i2 = n_mcmc+1
    endif
    if(i2.le.n_mcmc) goto 1

```

```
        array(i1) = temp
        index(i1) = itemp
    enddo
do i = n_mcmc,3,-1
    temp = array(i)
    itemp = index(i)
    array(i) = array(1)
    index(i) = index(1)
    i1 = 1
    i2 = 2
2    continue
    if((i2+1).lt.i.and.array(i2+1).lt.array(i2))
*i2=i2+1
    if(array(i2).lt.temp) then
        array(i1) = array(i2)
        index(i1) = index(i2)
        i1 = i2
        i2 = i1 + i1
    else
        i2 = i
    endif
    if(i2.lt.i) goto 2
    array(i1) = temp
    index(i1) = itemp
enddo
temp = array(2)
itemp = index(2)
array(2) = array(1)
index(2) = index(1)
array(1) = temp
index(1) = itemp
return
end
```

Bibliography

- [1] A. Einstein. Die grundlage der allgemeinen relativitätstheorie. *Annalen der Physik*, 49:769, 1916.
- [2] R. A. Hulse and J. H. Taylor. Discovery of a pulsar in a binary system. *The Astrophysical Journal*, 195:L51–L53, 1975.
- [3] J. H. Taylor, R. A. Hulse, L. A. Fowler, et al. Further observations of the binary pulsar PSR 1913+ 16. *Astrophysical Journal*, 206:L53–L58, 1976.
- [4] M. C. W. Sandford, editor. *First International LISA Symposium*. Classical Quantum Gravity, 1997.
- [5] B. S. Sathyaprakash and B. F. Schutz. Physics, Astrophysics and Cosmology with Gravitational Waves. *Living Reviews in Relativity*, 12(2), 2009.
- [6] M. Pitkin, S. Reid, S. Rowan, et al. Gravitational Wave Detection by Interferometry (Ground and Space). *Arxiv preprint arXiv:1102.3355*, 2011.
- [7] P.R. Saulson. *Fundamentals of interferometric gravitational wave detectors*, volume 1. 1994.
- [8] B.F. Schutz. Gravitational-wave sources. *Classical and Quantum Gravity*, 13:A219, 1996.
- [9] B. P. Abbott et al. Searches for periodic gravitational waves from unknown isolated sources and Scorpius X-1: Results from the second LIGO science run. *Physical Review D*, 76(8):082001, 2007.
- [10] B. Allen. The stochastic gravity-wave background: sources and detection. *Relativistic gravitation and gravitational radiation: proceedings of the Les Houches School of Physics, held in Les Houches, Haute Savoie, 26 September-6 October, 1995*, 1:373, 1997.

-
- [11] B. P. Abbott et al. Searching for a stochastic background of gravitational waves with the laser interferometer gravitational-wave observatory. *The Astrophysical Journal*, 659:918, 2007.
- [12] J. Weber. Detection and generation of gravitational waves. *Physical Review*, 117(1):306–313, 1960.
- [13] J. Weber. Gravitational-wave-detector events. *Physical Review Letters*, 20(23):1307–1308, 1968.
- [14] J. Weber. Anisotropy and polarization in the gravitational-radiation experiments. *Physical Review Letters*, 25(3):180–184, 1970.
- [15] J. Weber. Evidence for Discovery of Gravitational Radiation. *Physical Review Letters*, 22:1320–1324, 1969.
- [16] I. S. Heng, E. Daw, J. Giaime, et al. Allegro: noise performance and the ongoing search for gravitational waves. *Classical and Quantum Gravity*, 19:1889, 2002.
- [17] P. Astone, M. Bassan, P. Bonifazi, et al. Long term operation of the rome "explorer" cryogenic gravitational wave detector. *Physical Review D*, 47(2):362–375, 1993.
- [18] IS Heng, DG Blair, EN Ivanov, and ME Tobar. Long term operation of a niobium resonant bar gravitational wave antenna. *Physics Letters A*, 218(3-6):190–196, 1996.
- [19] M. Cerdonio, M. Bonaldi, D. Carlesso, et al. The ultracryogenic gravitational-wave detector AURIGA. *Classical and Quantum Gravity*, 14:1491, 1997.
- [20] A. Vinante, R. Mezzena, G.A. Prodi, et al. Thermal noise in a high Q ultracryogenic resonator. *Review of scientific instruments*, 76:074501, 2005.
- [21] S.E. Whitcomb. Ground based gravitational wave detection: now and future. *Classical and Quantum Gravity*, 25:114013, 2008.
- [22] M. Punturo et al. The Einstein Telescope: a third-generation gravitational wave observatory. *Classical and Quantum Gravity*, 27:194002, 2010.
- [23] K. Danzmann et al. LISA: Laser interferometer space antenna for gravitational wave measurements. *Classical and Quantum Gravity*, 13:A247, 1996.

- [24] K. Danzmann and A. Rüdiger. LISA technology: concept, status, prospects. *Classical and Quantum Gravity*, 20:S1, 2003.
- [25] D. Sigg. Status of the LIGO detectors. *Classical and Quantum Gravity*, 25, 2008.
- [26] B. Abbot. LIGO: The Laser Interferometer Gravitational-Wave Observatory . *arXiv:0711.3041v1 [gr-qc]*, 2007.
- [27] F. Acernese et al. Virgo upgrade investigations. *J. Phys.: Conf. Ser.*, 32:223, 2006.
- [28] R. Takahashi et al. Operational status of TAMA300 with the seismic attenuation system (SAS). *Classical and Quantum Gravity*, 25, 2008.
- [29] H. Grote. The status of GEO 600. *Classical and Quantum Gravity*, 25, 2008.
- [30] S. Hild et al. The status of GEO 600. *Classical and Quantum Gravity*, 23:S643, 2006.
- [31] W. A. Edelstein, J. Hough, J. R. Pugh, et al. Limits to the measurement of displacement in an interferometric gravitational radiation detector. *Journal of Physics E: Scientific Instruments*, 11:710, 1978.
- [32] B.J. Meers. Recycling in laser-interferometric gravitational-wave detectors. *Physical Review D*, 38(8):2317, 1988.
- [33] K. A. Strain and B. J. Meers. Experimental demonstration of dual recycling for interferometric gravitational-wave detectors. *Physical review letters*, 66(11):1391–1394, 1991.
- [34] G. Heinzel, K. A. Strain, J. Mizuno, et al. Experimental demonstration of a suspended dual recycling interferometer for gravitational wave detection. *Physical review letters*, 81(25):5493–5496, 1998.
- [35] Gravitational Wave Interferometer Noise Calculator, Caltech. <http://lhocds.ligo-wa.caltech.edu:8000/advligo/GWINC>.
- [36] P.R. Saulson. Terrestrial gravitational noise on a gravitational wave antenna. *Physical Review D*, 30(4):732–736, 1984.
- [37] S.A. Hughes and K.S. Thorne. Seismic gravity-gradient noise in interferometric gravitational-wave detectors. *Physical Review D*, 58(12):122002, 1998.

- [38] M. G. Beker, G. Cella, R. DeSalvo, et al. Improving the sensitivity of future GW observatories in the 1–10 Hz band: Newtonian and seismic noise. *General Relativity and Gravitation*, 43(2):623–656, 2011.
- [39] M. V. Plissi, C. I. Torrie, M. E. Husman, et al. GEO 600 triple pendulum suspension system: Seismic isolation and control. *Review of scientific instruments*, 71:2539, 2000.
- [40] B. Willke, P. Aufmuth, C. Aulbert, et al. Status of GEO 600. *Classical and Quantum Gravity*, 21:S417, 2004.
- [41] R. Abbott, R. Adhikari, G. Allen, et al. Seismic isolation for Advanced LIGO. *Classical and Quantum Gravity*, 19:1591, 2002.
- [42] Y. Levin. Internal thermal noise in the LIGO test masses: A direct approach. *Physical Review D*, 57(2):659, 1998.
- [43] G. M. Harry, A.M. Gretarsson, P.R. Saulson, et al. Thermal noise in interferometric gravitational wave detectors due to dielectric optical coatings. *Classical and Quantum Gravity*, 19:897, 2002.
- [44] D. R. M. Crooks, P. Sneddon, G. Cagnoli, et al. Excess mechanical loss associated with dielectric mirror coatings on test masses in interferometric gravitational wave detectors. *Classical and Quantum Gravity*, 19:883, 2002.
- [45] M. Evans, S. Ballmer, M. Fejer, et al. Thermo-optic noise in coated mirrors for high-precision optical measurements. *Physical Review D*, 78(10):102003, 2008.
- [46] V.B. Braginsky, V. P. Mitrofanov, and V.I. Panov. *Systems with small dissipation*. University of Chicago Press, 1985.
- [47] N. A. Robertson, G. Cagnoli, D. R. M. Crooks, et al. Quadruple suspension design for Advanced LIGO. *Classical and Quantum Gravity*, 19:4043, 2002.
- [48] V. B. Braginsky, M. L. Gorodetsky, and S. P. Vyatchanin. Thermodynamical fluctuations and photo-thermal shot noise in gravitational wave antennae. *Physics Letters A*, 264(1):1–10, 1999.
- [49] S. Rowan, R. L. Byer, M. M. Fejer, et al. Test mass materials for a new generation of gravitational wave detectors. In *SPIE Proc.*, volume 4865, page 292, 2003.
- [50] C.M. Caves. Quantum-mechanical radiation-pressure fluctuations in an interferometer. *Physical Review Letters*, 45(2):75–79, 1980.

- [51] C. M. Caves. Quantum-mechanical noise in an interferometer. *Physical Review D*, 23(8):1693, 1981.
- [52] R. Loudon. Quantum limit on the michelson interferometer used for gravitational-wave detection. *Physical Review Letters*, 47(12):815–818, 1981.
- [53] W. G. Unruh. In P. Meystre and M. O. Scully, editors, *Proceedings of the NATO Advanced Study Institute on Quantum Optics and Experimental General Relativity*, page 647, New York, 1983. Plenum Press.
- [54] V.B. Braginsky and Y.I. Vorontsov. Quantum-mechanical limitations in macroscopic experiments and modern experimental technique. *Physics-Uspkhi*, 17(5):644–650, 1975.
- [55] J. R. Smith. The path to the enhanced and advanced ligo gravitational-wave detectors. *submitted to Classical and Quantum Gravity*, 2009.
- [56] G. M. Harry. Advanced LIGO: the next generation of gravitational wave detectors. *Classical and Quantum Gravity*, 27:084006, 2010.
- [57] B. P. Abbott et al. LIGO: The laser interferometer gravitational-wave observatory. *Reports on Progress in Physics*, 72:076901, 2009.
- [58] G. Losurdo et al. Active Control Hierarchy in VIRGO Superattenuator: The Role of the Inverted Pendulum. In *Second Edoardo Amaldi Conference on Gravitational Wave Experiments*, volume 1, page 334, 1998.
- [59] S. Braccini, C. Bradaschia, R. Del Fabbro, et al. Seismic vibrations mechanical filters for the gravitational waves detector virgo. *Review of scientific instruments*, 67(8):2899–2902, 1996.
- [60] R. Flaminio, A. Freise, A. Gennai, et al. Advanced Virgo white paper. Technical Report VIR-NOT-DIR- 1390-304. Technical report, Virgo Collaboration, 2005.
- [61] Virgo Collaboration. Advanced Virgo Preliminary Design. Technical report, VIR-089A-08, (Virgo), 2008.
- [62] H. Grote, A. Freise, M. Malec, et al. Dual recycling for GEO 600. *Classical and Quantum Gravity*, 21:S473, 2004.
- [63] M. V. Plissi, K. A. Strain, C. I. Torrie, et al. Aspects of the suspension system for GEO 600. *Review of Scientific Instruments*, 69:3055, 1998.
- [64] M. Ando et al. Current status of TAMA. *Classical and Quantum Gravity*, 19:1409, 2002.

- [65] T. Akutsu, T. Akutsu, M. Ando, et al. Results of the search for inspiraling compact star binaries from TAMA300 observation in 2000–2004. *Physical Review D*, 74(12):122002, 2006.
- [66] S. Miyoki et al. Large scale cryogenic gravitational wave telescope. *Nuclear Physics B-Proceedings Supplements*, 138:439–442, 2005.
- [67] K. Kuroda. The status of LCGT. *Classical and Quantum Gravity*, 23:S215, 2006.
- [68] K. Kuroda. Status of LCGT. *Classical and Quantum Gravity*, 27:084004, 2010.
- [69] K. Yamamoto, T. Uchiyama, S. Miyoki, et al. Current status of the CLIO project. In *Journal of Physics: Conference Series*, volume 122, page 012002. IOP Publishing, 2008.
- [70] M. Punturo et al. The Einstein Telescope: a third-generation gravitational wave observatory. *Classical and Quantum Gravity*, 27:194002, 2010.
- [71] S. Hild, S. Chelkowski, A. Freise, et al. A xylophone configuration for a third-generation gravitational wave detector. *Classical and Quantum Gravity*, 27:015003, 2010.
- [72] A. Freise, S. Chelkowski, S. Hild, et al. Triple Michelson interferometer for a third-generation gravitational wave detector. *Classical and Quantum Gravity*, 26:085012, 2009.
- [73] G. Ballardini, S. Braccini, C. Bradaschia, et al. Measurement of the transfer function of the steering filter of the virgo super attenuator suspension. *Review of Scientific Instruments*, 72:3635, 2001.
- [74] S.D. Penn, A. Ageev, D. Busby, et al. Frequency and surface dependence of the mechanical loss in fused silica. *Physics Letters A*, 352(1-2):3–6, 2006.
- [75] B. Willke et al. The geo 600 gravitational wave detector. *Classical and Quantum Gravity*, 19:1377–1387, 2002.
- [76] O. L. Anderson and H. E. Bömmel. Ultrasonic absorption in fused silica at low temperatures and high frequencies. *Journal of the American Ceramic Society*, 38(4):125–131, 1955.
- [77] D. F. McGuigan, C. C. Lam, R. Q. Gram, et al. Measurements of the mechanical Q of single-crystal silicon at low temperatures. *Journal of Low Temperature Physics*, 30(5):621–629, 1978.

- [78] T. Uchiyama, T. Tomaru, M. E. Tobar, et al. Mechanical quality factor of a cryogenic sapphire test mass for gravitational wave detectors. *Physics Letters A*, 261(1-2):5–11, 1999.
- [79] ET Science Team. Einstein gravitational wave Telescope conceptual design study . Technical report, ET-0106C-10, 2011.
- [80] M. Alshourbagy, P. Amico, L. Bosi, et al. First characterization of silicon crystalline fibers produced with the μ -pulling technique for future gravitational wave detectors. *Review of scientific instruments*, 77(4):044502–044502, 2006.
- [81] M. Lorenzini, E. Cesarini, G. Cagnoli, et al. Silicate bonding properties: Investigation through thermal conductivity measurements. In *Journal of Physics: Conference Series*, volume 228, page 012019. IOP Publishing, 2010.
- [82] A. Dari, F. Travasso, H. Vocca, et al. Breaking strength tests on silicon and sapphire bondings for gravitational wave detectors. *Classical and Quantum Gravity*, 27(4):045010, 2010.
- [83] N. L. Beveridge, A. A. van Veggel, M. Hendry, et al. Low-temperature strength tests and SEM imaging of hydroxide catalysis bonds in silicon. *Classical and Quantum Gravity*, 28:085014, 2011.
- [84] R. Brown. A brief account of microscopical observations made in the months of June, July and August, 1827, on the particles contained in the pollen of plants; and on the general existence of active molecules in organic and inorganic bodies. *Philosophical Magazine*, 4:161–173, 1828.
- [85] A. Einstein. *Investigations on the Theory of the Brownian Movement*. Dover Pubns, 1956.
- [86] H.B. Callen and T.A. Welton. Irreversibility and generalized noise. *Physical Review*, 83(1):34–40, 1951.
- [87] R.F. Greene and H.B. Callen. On the formalism of thermodynamic fluctuation theory. *Physical Review*, 83(6):1231, 1951.
- [88] H.B. Callen and R.F. Greene. On a theorem of irreversible thermodynamics. *Physical Review*, 86:702–710, 1952.
- [89] A.S. Nowick and B.S. Berry. *Anelastic relaxation in crystalline solids*, volume 1. Academic Press, 1972.
- [90] F. Bondu, P. Hello, and J.Y. Vinet. Thermal noise in mirrors of interferometric gravitational wave antennas. *Physics Letters A*, 246(3-4):227–236, 1998.

-
- [91] Y.T. Liu and K.S. Thorne. Thermoelastic noise and homogeneous thermal noise in finite sized gravitational-wave test masses. *Physical Review D*, 62(12):122002, 2000.
- [92] S. Arrhenius. On the reaction rates of the inversion of cane sugar by acids. *Z. physik. Chem*, 4:226, 1889.
- [93] C. Zener. *Elasticity and anelasticity of metals*. University of Chicago Press, 1948.
- [94] A. L. Kimball and D. E. Lovell. Internal friction in solids. *Physical Review*, 30(6):948, 1927.
- [95] T. J. Quinn, C. C. Speake, and L. M. Brown. Materials problems in the construction of long-period pendulums. *Philosophical magazine. A.*, 65(2):261–276, 1992.
- [96] Y. Huang and P.R. Saulson. A method for measuring the dependence of internal friction on strain. *Review of scientific instruments*, 65(6):2102–2106, 1994.
- [97] S.D. Penn, P.H. Sneddon, H. Armandula, et al. Mechanical loss in tantalum/silica dielectric mirror coatings. *Classical and Quantum Gravity*, 20:2917, 2003.
- [98] D. R. M. Crooks, G. Cagnoli, M. M. Fejer, et al. Experimental measurements of coating mechanical loss factors. *Classical and Quantum Gravity*, 21:S1059, 2004.
- [99] A. Ageev, B.C. Palmer, A.D. Felice, et al. Very high quality factor measured in annealed fused silica. *Classical and Quantum Gravity*, 21:3887, 2004.
- [100] J. E Logan, J. Hough, and N. A. Robertson. Aspects of the thermal motion of a mass suspended as a pendulum by wires. *Physics Letters A*, 183(2-3):145–152, 1993.
- [101] G.I. González and P.R. Saulson. Brownian motion of a mass suspended by an anelastic wire. *The Journal of the Acoustical Society of America*, 96:207, 1994.
- [102] S. Rowan, S. M. Twyford, R. Hutchins, et al. Q factor measurements on prototype fused quartz pendulum suspensions for use in gravitational wave detectors. *Physics Letters A*, 233(4-6):303–308, 1997.
- [103] S. Rowan and S. M. Twyford. Mechanical losses associated with the technique of hydroxide-catalysis bonding of fused silica. *Physics Letters A*, 246(6):471–478, 1998.

- [104] P. H. Sneddon, S. Bull, G. Cagnoli, D. R. M. Crooks, E. J. Elliffe, J. E. Faller, M. M. Fejer, J. Hough, and S. Rowan. The intrinsic mechanical loss factor of hydroxy-catalysis bonds for use in the mirror suspensions of gravitational wave detectors. *Classical and Quantum Gravity*, 20:5025, 2003.
- [105] D. H. Gwo. Ultra-precision bonding for cryogenic fused-silica optics. *Proc. SPIE*, 3435:136–42, 1998.
- [106] D-H. Gwo. Ultra-precision and reliable bonding method. United States Patent no. US 6 284 085 B1, 2001.
- [107] D-H. Gwo, S. Wang, K. A. Bower, et al. The Gravity Probe-B star-tracking telescope. *Advances in space research*, 32:1401, 2003.
- [108] E. J. Elliffe, J. Bogenstahl, A. Deshpande, et al. Hydroxide-catalysis bonding for stable optical systems for space. *Classical and Quantum Gravity*, 22:S257, 2005.
- [109] S. Reid, G. Cagnoli, E. Elliffe, et al. Influence of temperature and hydroxide concentration on the setting time of hydroxy-catalysis bonds. *Physics Letters A*, 363:341–5, 2007.
- [110] L. Cunningham, P. G. Murray, A. Cumming, et al. Re-evaluation of the mechanical loss factor of hydroxide catalysis bonds and its significance for the next generation of gravitational wave detectors. *Physics Letters A*, 2010.
- [111] A. A. Van Veggel, D. Van den Ende, J. Bogenstahl, et al. Hydroxide catalysis bonding of silicon carbide. *Journal of the European Ceramic Society*, 28:303–10, 2008.
- [112] A. A. Van Veggel, J. Scott, D. A. Skinner, et al. Strength testing and SEM imaging of hydroxide catalysis bonds between silicon. *Classical Quantum Gravity*, 26(175007), 2009.
- [113] B. E. Deal and A. S. Grove. General relationship for the thermal oxidation of silicon. *Journal of Applied Physics*, 36:3770, 1965.
- [114] S. Franssila. *Introduction to microfabrication*. Wiley, 2010.
- [115] R. C. Jaeger. *Introduction to Microelectronic Fabrication*. Prentice Hall, 2002.
- [116] ASTM International, USA,. *ASTM norm C 1161-2C, Standard Test Method for Flexural Strength of Advanced Ceramics at Ambient Temperature*, 2006.

- [117] M. Ambrožič and K. Vidovič. Reliability of the Weibull analysis of the strength of construction materials. *Journal of Materials Science*, 42(23):9645–9653, 2007.
- [118] <http://www.itl.nist.gov/div898/handbook/apr/section1/apr162.htm>. Accessed 26/06/2012.
- [119] P. C. Gregory. *Bayesian logical data analysis for the physical sciences: a comparative approach with Mathematica support*. Cambridge University Press, 2005.
- [120] L. Cunningham, C. Torrie, and A. Cumming. Development of a model for Advanced LIGO thermal noise simulation. Internal LIGO Document T080163-06, 2008.
- [121] I. W. Martin. *Studies of materials for use in future interferometric gravitational wave detectors*. PhD thesis, University of Glasgow, 2009.
- [122] N. W. McLachlan. *Theory of Vibrations*. Dover, 1952.
- [123] D. J. McLachlan and L. L. Chamberlain. Atomic vibrations and melting point in metals. *Acta Metallurgica*, 12:571–576, 1964.
- [124] E. C. Chalkley. *Investigations of the properties of materials for the optics and suspensions of future gravitational wave detectors*. PhD thesis, University of Glasgow, 2010.
- [125] S. Rowan, G. Cagnoli, P. Sneddon, et al. Investigation of mechanical loss factors of some candidate materials for the test masses of gravitational wave detectors. *Physics Letters A*, 265:5, 2000.
- [126] W. Winkler, K. Danzmann, A. Rüdiger, et al. Heating by optical absorption and the performance of interferometric gravitational-wave detectors. *Physical Review A*, 44:7022–36, 1991.
- [127] S. D. Penn, G. M. Harry, A. M. Gretarsson, et al. High quality factor measured in fused silica. *Review of Scientific Instruments*, 72:3670, 2001.
- [128] K. Numata, S. Otsuka, M. Ando, and K. Tsubono. Intrinsic losses in various kinds of fused silica. *Classical and Quantum Gravity*, 19:1697, 2002.
- [129] S. M. Twyford. *Ph.D Thesis*. PhD thesis, University of Glasgow, 1998.
- [130] M. R. Abernathy, S. Reid, E. Chalkley, et al. Cryogenic mechanical loss measurements of heat-treated hafnium dioxide. *Classical and Quantum Gravity*, 28:195017, 2011.

-
- [131] D. Crooks. *Mechanical Loss and its Significance in the Test Mass Mirrors of Gravitational Wave Detectors*. PhD thesis, University of Glasgow, 2003.
- [132] C. Zener. Internal friction in solids. i. theory of internal friction in reeds. *Physical Review*, 52(3):230, 1937.
- [133] C. Zener. Internal friction in solids ii. general theory of thermoelastic internal friction. *Physical review*, 53(1):90, 1938.
- [134] A. S. Norwick and B. S. Berry. *Anelastic Relaxation in Crystalline Solids*. Academic, New York, 1972.
- [135] A. Heptonstall, G. Cagnoli, J. Hough, et al. Characterisation of mechanical loss in synthetic fused silica ribbons. *Physics Letters A*, 354(5-6):353–359, 2006.
- [136] S. Reid, G. Cagnoli, D. R. M. Crooks, et al. Mechanical dissipation in silicon flexures. *Physics Letters A*, 351(4-5):205–211, 2006.
- [137] Y. S. Touloukian and E. H. Buyco. Specific Heat Metallic Elements and Alloys, Thermophysical Properties of Matter: The TPRC Data Series.
- [138] R. Hull. Properties of crystalline silicon. Institution of Electrical Engineers, 1999.